

ABSTRACT

HATEM, TAREK MOUSTAFA. Microstructural Modeling of Heterogeneous Failure Modes in Martensitic Steels. (Under the direction of Professor Mohammed A. Zikry).

A three-dimensional multiple-slip dislocation-density-based crystalline formulation, specialized finite-element formulations, predictive failure models, and infinity-power integrable function based Voronoi tessellations adapted to martensitic orientations, were used to investigate large strain inelastic deformation, dislocation-density evolution in martensitic transformation, and heterogeneous failure modes in martensitic microstructures. The formulation is based on accounting for variant morphologies and orientations, secondary phases, such as retained austenite and inclusions, and initial dislocations-densities that are uniquely inherent to martensitic microstructures. The computational framework and the constitutive formulation were validated with experimental results for 10% Ni high-strength steel alloy. Furthermore, the formulation was used to investigate microstructures mapped directly from SEM/EBSD images of martensitic steel alloys.

The interrelated effects of microstructural characteristics, such as parent austenite orientation, variants distribution and arrangement, retained austenite, inclusions, initial dislocation-density, and defects, such as microcracks, and microvoids, were investigated for different failure modes such as rupture, transgranular and intergranular fracture, and shear localization over a broad spectrum of loading conditions that range from quasi-static to high strain-rate conditions.

The computational predictions, consistent with experimental observations, indicated that variant morphology and orientations have a direct consequence on how shear-strain accumulation and failure evolves in martensitic microstructures subjected to quasi-static and high strain-rate loading conditions. The analysis shows that shear-strain localization occurs due to slip-system compatibilities corresponding to low-angle blocks boundaries, the loading direction and the long direction of laths, which result in shear-pipes. At specific triple junctions, rotation misalignments due to lattice and slip incompatibilities occur, and this further exacerbated by defects. The results underscore the inherent competition between shear localization, transgranular, and intergranular failure modes. For certain variant arrangements, which correspond to random low angle orientations, cracks can be blunted by dislocation-density activities along transgranular planes. The effects of strain rate and inclusions on the evolution of shear-strain localization were also investigated under both tensile and compressive loadings. Tensile hydrostatic pressure forms under dynamic loads, and combined with plastic shear-slip accumulation between inclusions and the martensitic matrix accelerate shear-strain localization.

© Copyright 2009 by Tarek Moustafa Hatem

All Rights Reserved

Microstructural Modeling of Heterogeneous Failure modes in
Martensitic Steels

by
Tarek Moustafa Hatem

A dissertation submitted to the Graduate Faculty of
North Carolina State University
in partial fulfillment of the
requirements for the degree of
Doctor of Philosophy

Mechanical Engineering

Raleigh, North Carolina

2009

APPROVED BY:

Dr. Ronald Scattergood

Dr. Kara Peters

Dr. Larry Silverberg

Dr. Mohammed Zikry
Chair of Advisory Committee

DEDICATION

This work is dedicated in loving memory of my mother, Madge Shalaby. For raising five children, bearing, feeding, nursing, educating, caring and loving. For keeping our household clean, joyful and safe. For inspiring us to be what we are, and making us believe that there are no walls for knowledge and dreams. For instructing Physics to high school girls, and making them better women. For standing tall against unjust, need and ignorance. May Allah reward her with the highest of all rewards that are due to her ... Amen.

BIOGRAPHY

Tarek M. Hatem was born in Kuwait in September 29th, 1979. After Kuwait occupation in 1990, he returned to his home country (Egypt). At middle and high school graduations, Tarek was awarded for the highest GPA among the senior classes in his county (Mokattam hills), and received a five years full scholarship to attend Engineering School in Cairo University.

He received a Bachelor of Science in Aerospace Engineering in 2001. His graduation project, the first prototype of Egyptian amateur satellite, received the highest board of Egyptian universities' first place award for scientific projects in 2001, and was presented in many Egyptian and Regional TV channels. At graduation, he was nominated to join aggregation of 12 distinguished professors and 10 exceptional engineers to develop the first remote sensing satellite for desert development (DesertSat), at the Egyptian National Authority of Remote Sensing and Space Science (NARSS). During 2001-2003 in NARSS, he received a six-month training by Ukranian Yuzhnoye Design Office, accomplished the first full design and mission analysis for DesertSat, designed and fabricated an RPV and an aerial remote sensing and tracking system, and innovatively designed an orbit tailored for desert monitoring applications. He is a founder member of Aerospace Cairo group.

After, he Joined Applied Science Int. (ASI) as a senior software developer and a research engineer. In 2004, he received the highest employee evaluation and correspondingly the highest salary raise. During 2003-2005 in ASI, he led the effort to develop first

commercial CAD and structural analysis package for progressive collapse using Applied Element Method (AEM), optimized, verified and validated AEM solver, provided first full analysis for Alfred P. Murrah Federal building collapse under terrorist attacks, analyzed Ramsis II historical statue during reallocation, analyzed large number of structures during collapse or under extreme loadings, prepared web demonstrations and tutorials for the new software, and interviewed, hired, trained, and mentored senior and junior developers and trainees.

In 2005, Tarek received his Master of Science in Aerospace Engineering ranked 3rd of 45, with a concentration in Aerospace Structural Analysis and Control, under the oversight of Professor M. Nader Abuelfoutouh, and Professor Hany M. Negm in the field of structural health monitoring of composite and metallic structures using genetic and neural networks algorithms. Three publications, comprising one proceeding, one journal article and his Masters Thesis, were produced and presented from the work.

After, he pursued a Doctor of Philosophy degree in Mechanical Engineering at North Carolina State University under the oversight of Professor Mohammed A. Zikry in the field of microstructural modeling of heterogeneous failure in Martensitic steels and materials design with support from the Office of Naval Research (ONR) through Grant #N000140510097. Nine publications, comprising three proceedings, five journal articles and his Ph.D. dissertation, were produced and presented from the work.

During his study in NCSU, he received a Master of Material Science and Engineering in 2008 with concentration in mechanical behavior and phase transformation of metals and

semiconductors, enrolled in Technology Entrepreneur and Commercialization (TEC) program for academic year of 2007-2008, acted as a teaching assistant for courses of finite element method (fall 2005, and fall 2008), advanced finite element methods (spring 2008), and modern plasticity (spring 2008), was elected for Sigma Gamma Tau in 2006, the same year he was elected to Phi Kappa Phi, later he was elected for Tau Beta Pi in 2007, and joined professional societies of ASME, AIAA, IEEE, MRS, SIAM, and AMSat. Tarek served as Science Officer of Egyptian Student Association in North America (ESANA). After graduation, Tarek decided to pursue an academic career, and accepted a position with Professor Mohammed A. Zikry as a research associate.

ACKNOWLEDGMENTS

I would like to thank so many. God for his blessing and mercy, by Him I would like to be taught, and by Him I would like to be rewarded. My country (Egypt) for its generosity and forgiveness, by it I would like to be associated. My mother (Madge) for her lasting love, confidence, and dedication, by her I would like to be inspired. My father (Dr. Moustafa) for his encouragement and support, by him I would like to move forward. My family (Ahmed, Rana, Mohammed, and Sarah) for being what they are, by them I would like to be surrounded. My academic advisor (Dr. Zikry) for his patient, advice and being more than academic advisor for me, by him I would like to be guided. My mentors and role models (Dr. Scattergood, Dr. Ghoniem, and Dr. Zikry again!) for listening, wisdom, kindness and teaching, by them I would like to be lifted up. My committee members (Dr. Peters, Dr. Silverberg, Dr. Scattergood and Dr. Zikry again!) for delight and insight, by them I would like to be instructed. My labmates and friends (Omid, Fadi, James, Khalil, Jibin, Pratheek, William, Siqi, Walid, Hatem, Jaafar, Dr. Ashraf and Dr. Waeil) for friendship, joy and new perspectives, by them I would like to be accompany. My life cast (so many include those already listed and colleagues, friends, staff and faculty in MAE, MSE (special thanks go to Edna Edas), Math, CE, CSE, TEC, HPC, ONR, ESANA, ...) for making my life as complete as it has been, without you this work will be impossible, and without you I will not go any further. Cheers!

I would like also to thank this great country and the Office of Naval Research (ONR) for making this opportunity available through Grant #N000140510097. Finally, I would like to pray to god to bring justice, prosperity and knowledge to humankind ... Amen.

TABLE OF CONTENTS

LIST OF TABLES	xii
LIST OF FIGURES	xiii
CHAPTER 1. INTRODUCTION	1
1.1 References	6
CHAPTER 2. MULTIPLE-SLIP CRYSTAL PLASTICITY	
CONSTITUTIVE FORMULATION	10
2.1 Multiple-Slip Crystal Plasticity Formulation	10
2.2 Evolutionary Equations for the Mobile and Immobile Dislocation Densities	15
2.3 Determination of the Coefficients for the Coupled Evolutionary Equations	22
2.4 References	24
CHAPTER 3. MARTENSITIC MICROSTRUCTURAL	
REPRESENTATION	27
3.1 Crystalline Structure of Heterogeneous Microstructure of	

Martensite	27
3.2 Martensitic Orientation.....	28
3.3 Morphology: Variant Arrangement and Distribution.....	33
3.4 Secondary-Phases Structures.....	35
3.5 Transformation Dislocations Densities	36
3.6 References	37
3.7 Tables and Figures (Chapter 3)	41
CHAPTER 4. NUMERICAL METHODS	49
4.1 L_∞ Voronoi Tessellation Algorithm	57
4.2 References	58
4.3 Figure (Chapter 4)	59
CHAPTER 5. A NEW PREDICTIVE MODEL FOR INITIAL	
 DISLOCATION-DENSITIES FOR MARTENSITIC	
 TRANSFORMATION	60
5.1 Phenomenological Transformation Models	61
5.2 Results for Transformation in f.c.c. and b.c.c. Crystals	63
5.3 Summary	66
5.4 References	68
5.5 Table and Figure (Chapter 5)	70

CHAPTER 6.	MODELLING OF LATH MARTENSITIC	
	MICROSTRUCTURES	73
6.1	Model Validation	74
6.2	Parent Austenite Orientation	80
6.3	Retained Austenite	81
6.4	Physically Representative Microstructure: SEM/EBSD	
	Steel Microstructures.....	83
6.5	Summary	84
6.6	References	86
6.7	Table and Figures (Chapter 6)	87

CHAPTER 7.	SHEAR PIPES EFFECT AND SHEAR-STRAIN	
	LOCALIZATION IN LATH MARTENSITIC	
	MICROSTRUCTURES	103
7.1	Shear-Strain Localization and Shear Pipes Effect Model	104
7.2	Microcrack and Shear-Strain Localization Interactions	109
7.3	Dynamic Behavior and Shear Band Formation	110
7.4	Voids/Inclusions and Shear-Strain Localization	
	Interactions	111
7.5	Summary	113
7.6	References	115

7.7 Table and Figures (Chapter 7)	117
CHAPTER 8. FRACTURE EVOLUTION IN LATH MARTENSITIC MICROSTRUCTURES	129
8.1 Transgranular and Intergranular Failure Models	129
8.2 Voids-Crack Tip Interactions	136
8.3 Summary	138
8.4 References	140
8.5 Figures (Chapter 8)	142
CHAPTER 9. SHEAR-STRAIN LOCALIZATION AND INCLUSION EFFECTS UNDER HIGH COMPRESSIVE DYNAMIC LOADS	154
9.1 Dynamic Shear-Strain Localization Under Compressive Pressure Loads	155
9.2 Secondary-Phase Inclusions Effects	160
9.3 Summary	163
9.4 References	166
9.5 Table and Figures (Chapter 9)	167
CHAPTER 10. RECOMMENDATIONS FOR FUTURE RESEARCH.....	184

LIST OF TABLES

Table 3.1	Slip-systems of martensitic b.c.c. phase	42
Table 3.2	Slip-systems of austenitic f.c.c. phase	43
Table 3.3	Slip-systems of MnS inclusions crystal structure.....	44
Table 3.4	The 24 variants corresponding to K-S OR and their numbering.....	45
Table 5.1	Properties of martensite and austenite steels	71
Table 6.1	Properties of martensitic and austenitic grains.....	88
Table 7.1	The angle between slip systems for variants 1-6 (a packet with habit plane of $(111)_\gamma$) that can be divided into groups of high and low angle GB directions. (*) denotes compatibility between slip systems that are not initially active relative to loading direction $[010]_\gamma$	118
Table 9.1	Properties of martensitic and MnS inclusions	168

LIST OF FIGURES

Figure 3.1	The relation between the austenite phase and the martensite phase for the six variants sharing $(111)_\gamma$ habit plane	46
Figure 3.2	The alignment of variants in space, relative to each other and others planes. Three main relations can be identified, flat, sharp, and extended inward	47
Figure 3.3	Lath martensite hierarchical microstructure, defined in four scale architecture, parent austenite grains, packets, blocks, and laths	48
Figure 4.1	Proposed L_∞ Voronoi tessellations (a) ordinary Voronoi tessellations. (b) L_∞ Voronoi tessellations to the same set of points. (c) Applying the same algorithm with tilt angle of 30° . (d) modified L_∞ Voronoi tessellation algorithms (sharp corners avoided)	60
Figure 5.1	The boundary conditions and loading for a simple shear problem. P_2 is parallel to y-axis and d_2 is parallel to x-axis	72
Figure 6.1	Microstructural model used in the current study, the distribution of variants in blocks and packets (variants numbered as indicated in Table 3.4), and loading, geometry, and boundary conditions	89
Figure 6.2	Global stress-strain curve for experimental and predicted results for low nickel martensitic steel (Stresses values are normalized by the static yield stress)	90
Figure 6.3	Global stress-strain curve for experimental results for low nickel martensitic steel, compared with numerical results obtained using ordinary Voronoi algorithms and proposed L_∞ Voronoi algorithm	91
Figure 6.4	Normalized mobile dislocation-densities for most active slip-systems; (a) slip-system $(\bar{1}12) / [\bar{1}\bar{1}1]$, (b) slip-system $(112) / [111]$, and (c) slip-system $(1\bar{1}2) / [\bar{1}11]$ at a nominal strain of 15%. Values normalized by mobile dislocation-densities saturation values, $\rho_{m,s}^{(\alpha)} = 6.86 \times 10^{14} \text{m}^{-2}$	92

Figure 6.5	Normalized immobile dislocation-densities for most active slip-systems; (a) slip-system $(\bar{1}12) / [1\bar{1}1]$, (b) slip-system $(112) / [11\bar{1}]$, and (c) slip-system $(1\bar{1}2) / [\bar{1}11]$ at a nominal strain of 15%. Values normalized by immobile dislocation-densities saturation values, $\rho_{m,s}^{(\alpha)} = 1.16 \times 10^{16} \text{m}^{-2}$	93
Figure 6.6	Results obtained for the modeled specimen, at a nominal strain of 15% (a) Shear slip contours γ ; (b) schematic of the specimen with shear localization region highlighted	94
Figure 6.7	$[010]_{\gamma}$ stereographic projection for variant #11 slip-systems relative to the loading direction, the locus of maximum resolved shear stress (the inner circle) and the long direction of the variants (presented as * in figure a) (a) the slip directions, (b) the slip planes.....	95
Figure 6.8	Results obtained for the modeled specimen, at a nominal strain of 15%; (a) lattice rotation in degrees; (b) normalized normal stresses; (c) normalized shear stresses. Stresses values are normalized by the static yield stress	96
Figure 6.9	Normalized mobile dislocation-densities for most active slip-systems for $[011]_{\gamma}$ loading direction; (a) slip-system $(011) / [1\bar{1}\bar{1}]$, (b) slip-system $(011) / [1\bar{1}1]$, at a nominal strain of 15%	97
Figure 6.10	Normalized immobile dislocation-densities for most active slip-systems for $[011]_{\gamma}$ loading direction, (a) slip-system $(011) / [1\bar{1}\bar{1}]$, (b) slip-system $(011) / [1\bar{1}1]$, at a nominal strain of 15%	98
Figure 6.11	Results obtained for the modeled specimen for $[011]_{\gamma}$ loading direction, at a nominal strain of 15%, (a) shear slip γ , (b) lattice rotation in degrees	99
Figure 6.12	Results obtained for the modeled specimen with 10% of retained austenite, at a nominal strain of 15%. (a) shear slip γ , (b) lattice rotation in degrees, both for retained austenite placed inside the blocks (Model 1). (c) shear slip γ , (d) lattice rotation in degrees, both for retained austenite placed at block boundary (Model 2).....	100
Figure 6.13	Physically representative microstructure mapped from SEM/EBSD steel microstructure and the distribution of variants, [6]	101

Figure 6.14	Results obtained from mapped experimental specimens, at nominal strains of 5% and 15%. (a) shear slip γ , (b) lattice rotation in degrees, both at nominal strain of 5%. (c) shear slip γ , (d) lattice rotation in degrees, both at a nominal strain of 15%	102
Figure 7.1	Microstructural model used in the current study, the distribution of variants in blocks and packets (variants numbered as indicated in Table 3.4), loading, geometry, and boundary conditions	119
Figure 7.2	Normalized mobile and immobile dislocation-densities at a nominal strain of 7.5% for most active slip-systems for (a) slip-system (112) / [11 $\bar{1}$], (b) slip-system ($\bar{1}$ 12) / [$\bar{1}$ 11], (c, d) immobile dislocation-densities, (c) slip-system (112) / [111], (d) slip-system ($\bar{1}$ 12) / [$\bar{1}$ 11]	120
Figure 7.3	Behavior at a nominal strain of 7.5% (a) Shear slip contours, (b) lattice rotation in degrees, (c) normalized normal stress, (d) normalized shear stresses. Stresses values are normalized by the static yield stress	121
Figure 7.4	[010] $_{\gamma}$ upper hemisphere stereographic projection for variant #3 slip-systems relative to the loading direction, the locus of maximum resolved shear stress (the inner circle) and the long direction of the variants (denoted as * in figure a) (a) the slip directions, (b) the slip planes.....	122
Figure 7.5	Rotation misfit at triple junction in shear localization area, (a) without microcracks, (b) with microcrack in the shear-strain localization region	123
Figure 7.6	Shear localization - microcrack interaction at a nominal strain of 7.5% (a) shear slip, (b) lattice rotation	124
Figure 7.7	Dynamic loading (120/sec strain rate), at a nominal strain of 7.5% (a) Shear slip contours, (b) lattice rotation in degrees, (c) normalized normal stress, (d) temperature in degrees Kelvin.....	125
Figure 7.8	Dynamic loading (12,000/sec strain rate), at a nominal strain of 7.5% (a) Shear slip contours, (b) lattice rotation in degrees, (c) normalized normal stress, (d) temperature in degrees Kelvin.....	126

Figure 7.9	Microstructural model and inclusion distribution	127
Figure 7.10	Dynamic loading (12,000/sec strain rate) – void/inclusion interactions, at a nominal strain of 7.5% (a) Shear slip contours, (b) lattice rotation in degrees, (c) normalized normal stress, (d) temperature in degrees Kelvin.....	128
Figure 8.1	Microstructural model used in the current study (a) the distribution of variants in blocks and packets for low angle GBs specimen (Model 1), variants numbered as in Table 3.4; (b) the distribution of variants in blocks and packets for high angle GBs model (Model 2); (c) loading, geometry, and boundary conditions	143
Figure 8.2	Normalized mobile dislocation-densities for most active slip-systems for low angle GBs specimen, (a) slip-system (112) / [11 $\bar{1}$], (b) slip-system ($\bar{1}$ 12) / [1 $\bar{1}$ 1], at a nominal strain of 7.5%. Values normalized by the mobile dislocation-density saturation value, $\rho_{m,s}^{(\alpha)} = 6.86 \times 10^{14} \text{m}^{-2}$	144
Figure 8.3	Normalized immobile dislocation-densities for most active slip-systems for low angle GBs specimen, (a) slip-system (112) / [111], (b) slip-system ($\bar{1}$ 12) / [1 $\bar{1}$ 1], at a nominal strain of 15%. Values are normalized by immobile dislocation-densities saturation values, $\rho_{im,s}^{(\alpha)} = 1.16 \times 10^{16} \text{m}^{-2}$	145
Figure 8.4	Behavior for low angle GBs, at a nominal strain of 7.5% (a) Shear slip contours γ ; (b) lattice rotation in degrees, (c) normalized normal stresses, (d) normalized shear stresses. Stresses values are normalized by the static yield stress.....	146
Figure 8.5	[010] $_{\gamma}$ upper hemisphere stereographic projection for variant #3 slip-systems relative to the loading direction, the locus of maximum resolved shear stress (the inner circle) and the long direction of the variants (denoted as * in figure a) (a) the slip directions, (b) the slip planes.....	147
Figure 8.6	Normalized mobile dislocation-densities for the most active slip-systems for high angle GBs for (a) slip-system (112) / [11 $\bar{1}$], (b) slip-system ($\bar{1}$ 12) / [1 $\bar{1}$ 1], at a nominal strain of 15%	148

Figure 8.7	Normalized immobile dislocation-densities for most active slip-systems for high angle GBs for (a) slip-system (112) / [11 $\bar{1}$], (b) slip-system ($\bar{1}$ 12) / [1 $\bar{1}$ 1], at a nominal strain of 15%	149
Figure 8.8	Results obtained for the high angle GBs specimen, at a nominal strain of 7.5% (a) Shear slip contours γ , (b) lattice rotation in degrees, (c) normalized normal stresses, (d) normalized shear stresses	150
Figure 8.9	Microstructural model and void distribution	151
Figure 8.10	Shear slip around the crack tip indicating crack tip-micro voids interactions for low angle GBs (a, b) and high angle GBs (d, c)	152
Figure 8.11	Normal stresses around the crack tip indicating crack tip-micro void interactions for low angle GBs (a, b) and high angle GBs (c, d)	153
Figure 9.1	Microstructural model used in the current study, the distribution of variants in blocks and packets (variants numbered as indicated in Table 3.4), loading, geometry, and boundary conditions	169
Figure 9.2	The global stress-strain curve for low nickel martensitic steel for different strain-rates (stresses are normalized by the static yield stress)	170
Figure 9.3	Nominal strain-rate and strain for different loading pressures. The arrows indicate wave reflection from one of the horizontal boundaries; (A) incident wave reflects from the bottom boundary; (B) wave reflects from the top boundary; (C) wave reflects from the bottom boundary again; (D) wave reflects from the top boundary	171
Figure 9.4	Normalized normal stresses for a dynamic pressure loading of 0.5 GPa at different times	172
Figure 9.5	Dynamic loading (1.0 GPa), at 12.5 μ s (a) Shear slip contours, (b) lattice rotation in degrees, (c) normalized normal stress, (d) temperature in degrees Kelvin.....	173
Figure 9.6	Normalized hydrostatic pressure stresses for a dynamic loading of 1.0 GPa at different times	174

Figure 9.7	Shear slip for a dynamic loading 1.5 GPa at different times.....	175
Figure 9.8	Lattice rotation and temperature for a dynamic loading of 1.5 GPa at 7.5 and 12.5 μ s (a-b) lattice rotation in degrees, (c-d) temperature in degrees Kelvin.....	176
Figure 9.9	Mobile and immobile dislocation-densities at 7.5 μ s for most active slip-systems for (a) slip-system (112) / $[11\bar{1}]$, (b) slip-system ($\bar{1}12$) / $[1\bar{1}1]$, (c, d) immobile dislocation-densities, (c) slip-system (112) / $[1\bar{1}1]$, (d) slip-system ($\bar{1}12$) / $[1\bar{1}1]$ at a pressure loading of 1.5 GPa	177
Figure 9.10	$[010]_{\gamma}$ stereographic projection for variant #11 slip-systems relative to the loading direction, the locus of maximum resolved shear stress (the inner circle) and the long direction of the variants (presented as * in figure a) (a) the slip directions, (b) the slip planes	178
Figure 9.11	Microstructural model and inclusion distribution	179
Figure 9.12	Normalized normal stresses for a dynamic loading of 0.5 GPa - inclusion interactions at different times	180
Figure 9.13	Shear strain for dynamic loading at a dynamic loading of 1.5 GPa – inclusions interactions at different times	181
Figure 9.14	Mobile and immobile dislocation-densities at 7.5 μ s for the most active slip-systems for (a) slip-system (112) / $[11\bar{1}]$, (b) slip-system ($\bar{1}12$) / $[1\bar{1}1]$, (c, d) immobile dislocation-densities, (c) slip-system (112) / $[1\bar{1}1]$, (d) slip-system ($\bar{1}12$) / $[1\bar{1}1]$ at pressure loading of 1.5 GPa	182
Figure 9.15	Dynamic loading at a pressure of 1.5 GPa – inclusion interactions at 7.5 μ s (a) lattice rotation in degrees, (b) temperature in degrees Kelvin, (c) hydrostatic pressure	183

CHAPTER 1

INTRODUCTION

Martensitic microstructures, such as lath, plate, and butterflies, have been commonly observed in several morphologies in steel, see, for example, Otsuka and Wayman [1]. These morphologies are generally controlled by alloying elements, such as carbon and nickel. Lath martensitic steels due to their high strength, wear resistance, and toughness have myriad military and civilian applications. These properties are uniquely inherent to martensitic steels, as a result of its lath microstructure that has distinct orientations, distributions, and morphologies pertaining to martensitic transformations, see, for example, Krauss [2-16]. Specifically, the effects of lath martensite (b.c.c.) morphology, parent austenite (f.c.c.) orientation, strains related to transformations from f.c.c. to b.c.c. structures, and secondary-phases (e.g. retained austenite and inclusions) all have interrelated effects on deformation and failure.

Due to the fine microstructure of lath martensite, it has been difficult to fully characterize lath martensite and understand its effect on overall behavior. Wayman [7-9] conducted a series of pioneering experiments that identified lath martensite's characteristics, such as the habit plane of lath martensite and martensite Orientation Relations (ORs); the lath microstructure in successive layers; the internal and interfacial dislocation microstructure in lath martensite. Kelly [15] utilized Wayman's work to interpret lath martensite microstructure using phenomenological theory to elucidate how martensitic diffusionless

transformation occurs. In recent years, Morito and his colleagues [10-14] have conducted significant experiments, utilizing TEM, SEM and EBSD characterization to classify how martensitic structures can be characterized in categories of laths, blocks (variants with low angle mismatch) and packets (collection of blocks with the same habit plane) microstructures and to characterize their orientation relations and distributions. Spanos *et al.* [16] have used EBSD and serial sectioning to construct a 3D morphology of coarse martensite lath, which provided further detailed insights on lath orientations, and shapes.

Thomas [5-6] studied the effect of retained austenite on mechanical properties and failure of Martensitic steels. Krauss had conducted a large amount of experiments to study the effect of microstructure on dislocation evolution and failure of martensitic steels, see, for example, [2-3]. Garrison studied the effect of inclusions in ductile fracture in high strength steel, see, for example, [17-19]. Minnaar and Zhou [20] studied the effect of inclusions on dynamic failure under compression loadings of naval steels. All of these investigations have clearly indicated that quasi-static and dynamic behavior, dislocation-density evolution, and failure in high-strength martensitic steels are affected by martensitic morphologies and characteristics.

Most finite-element investigations pertaining to martensitic steels utilize phenomenological plasticity models, see, for example, [21-23]. These approaches do not account for the crystalline structure and the inherent anisotropy of martensite. Furthermore, critical martensitic characteristics, such as ORs, morphologies, parent austenite orientations, initial dislocation-densities, and retained austenite are not accounted for in these studies.

Molecular dynamic (MD) simulations [24-26] have been invaluable for predicting defect nucleation and transformation at the molecular level. However, there are severe limitations related to temporal and spatial scales that minimize understanding or predicting behaviour at the relevant microstructural level.

Therefore, to address these limitations, we extend the dislocation-density based crystalline models proposed by Zikry and Kao [27] and Ashmawi and Zikry [28] to b.c.c. crystalline microstructures, for details see Hatem and Zikry [29]. Within this formulation, we account for martensitic transformations and parent austenite crystalline orientations for an accurate OR description of lath microstructure. This representation is based on arranging variants within packets and blocks that are categorized in terms of habit planes and orientations. Furthermore, the current study accounts for retained austenite and the effects of initial dislocation-densities. The initial mobile and immobile dislocation-densities incorporated in the current study were obtained from numerical models based on a proposed transformation crystalline plasticity model and the phenomenological theory of martensitic transformation. An L_∞ Voronoi tessellation algorithm, see [30-31], is also used to generate physically representative microstructures that have been adapted to account for the orientation of blocks parallel to the habit plane for an accurate representation of martensitic morphologies. These are coupled with specialized finite-element formulations for a predictive framework related to martensitic steels.

The computational framework and the constitutive formulation were validated with experimental results of 10% Ni high-strength steel alloy. Furthermore, the formulation was

used to investigate microstructures mapped directly from SEM/EBSD images of martensitic steel alloys.

Hence, the major objective of the present study is to use systematic and predictive framework related to dislocation-density evolution, predictive failure models, specialized finite element, and L_∞ Voronoi tessellation algorithm related to martensitic orientation, to study the interrelated effects of microstructural characteristics and micro-defects such as parent austenite orientation, variants distribution and arrangement, retained austenite, inclusions, initial dislocation-density, microcracks, and microvoids, relative to different failure modes such as rupture, transgranular and intergranular fracture, and shear localization over a wide range of loading conditions that range from quasi-static to high strain-rate dynamics.

This dissertation is organized as follows: the rate-dependent dislocation-density based constitutive formulation is introduced in Chapter 2. The martensitic microstructural representation is presented in Chapter 3. The computational approach and the new L_∞ Voronoi tessellation algorithm for microstructural modeling are presented in Chapter 4. The new model for martensitic transformation is presented in Chapter 5. The continuum validation model using the experimental data and the physically representative microstructures are presented in Chapter 6. The results and analysis of shear-strain localization in martensitic microstructures are presented in Chapter 7. Models of transgranular and intergranular fracture and voids-crack interactions are presented in Chapter 8. The results of computational simulations of dynamic behavior, shear-strain localization

and inclusions effects are presented in Chapter 9. In closure, future recommendations for the current research are outlined in Section 10.

REFERENCES

- [1] Otsuka K. and Wayman C. M., 1999, *Shape Memory Alloys*, Cambridge University Press, UK.
- [2] Krauss G., 2001, "Deformation and Fracture in Martensitic Carbon Steels Tempered at Low Temperature," *Metall. Mater. Trans. A*, 32B, pp. 205-221.
- [3] Saeglitz M., and Krauss G., 1997, "Deformation, Fracture, and Mechanical Properties of Low-Temperature-Tempered Martensite in SAE 43xx Steels," *Metall. Mater. Trans., A* 28A, pp. 377-387.
- [4] Morito S., Yoshida H., *et al.*, 2006, "Effect of Block Size on the Strength of Lath Martensite in Low Carbon Steels," *Mater. Sci. Eng A-Struct.*, 438-40, pp. 237-240.
- [5] Thomas G., 1978, "Retained Austenite and Tempered Martensite Embrittlement," *Metall. Trans. A*, 9A, pp. 439-450.
- [6] McMahon J. A. and Thomas G., 1973, *Proceedings of the 3rd International Conference on the Strength of Metals and Alloys*, Institution of Metals, London, pp. 180-184.
- [7] Wasaka W. and Wayman C. M., 1981, *The Morphology and Crystallography of Ferrous Lath Martensite. Studies of Fe-20%Ni-5%Mn-I, II, III,*" *Acta Metall.*, 29, pp. 973-990, 991-1011, 1013-1028.
- [8] Wasaka W. and Wayman C. M., 1981, "Crystallography and Morphology of Ferrous Lath Martensite," *Metallography*, 14, pp. 49-60.
- [9] Sandvik B. P. J. and Wayman C. M., 1983, "Characteristics of Lath Martensite, I, II, III," *Metall. Trans. A*, 14A, pp. 809-822, 823-834, 835-844.

- [10] Morito S., Huang X., *et al.*, 2006, "The Morphology and Crystallography of Lath Martensite in Alloys Steels," *Acta Mater.*, 54, pp. 5323-5331.
- [11] Morito S., Tanaka H., 2003, *et al.*, "The Morphology and Crystallography of Lath Martensite in Fe-C Alloys," *Acta Mater.*, 51, pp. 1789-1799.
- [12] Morito S., Kishida I. and Maki T., 2003, "Microstructure of Ausformed Lath Martensite in 18%Ni Maraging Steel," *J. Phys. IV France*, 112, pp. 453-456.
- [13] Morito S., Nishikawa J., *et al.*, 2003, "Dislocation Density within Lath Martensite in Fe-C and Fe-Ni Alloys," *ISIJ Int.*, 43(9), pp. 1475-1477.
- [14] Morito S., Saito H. *et al.*, 2005, "Effect of Austenite Grain Size on the Morphology and Crystallography of Lath Martensite in Low Carbon Steels," *ISIJ Int.*, 45(1), pp. 91-94.
- [15] Kelly P. M., 1992, "Crystallography of Lath Martensite in Steels," *Mater. Trans. JIM*, 33(3), pp. 235-242.
- [16] Rowenhorst D. J., Gupta A., Feng C. R. and Spanos G., 2006, "3D Crystallography and Morphological Analysis of Coarse Martensite: Combining EBSD and Serial Sectioning," *Scripta Mater.*, 55, pp. 11-16.
- [17] Garrison W. M., and Moody N. R., 1987, "Ductile Fracture," *J. Phys. Chem. Solids*, 48(11), pp. 1035-1074.
- [18] Lorio L. E., and Garrison W. M., 2002, "Effects of Gettering Sulfur as CrS or MnS on Void Generation Behavior in Ultra-High Strength Steel," *Scripta Mater.*, 46(12), pp. 863-868.

- [19] Garrison W. M. and Wojcieszynski A. L., 2007, "A Discussion of the Effect of Inclusion Volume Fraction on the Toughness of Steel," *Mater. Sci. Eng A-Struct.*, 464, pp. 321-329.
- [20] Minnaar K., and Zhou M., 1998, "An Analysis of the Dynamic Shear Failure Resistance of Structural Metal," *J. Mech. Phys. Solids*, 46-10, pp. 2155-2170.
- [21] McVeigh C., Vernerey F., 2007, *et al.*, "An Interactive Micro-Void Shear Localization Mechanism in High Strength Steels," *J. Mech. Phys. Solids*, 55, pp. 225-244.
- [22] Zhai J., Tomar V., 2004, *et al.*, "Micromechanical Simulation of Dynamic Fracture Using Cohesive Finite Element Method," *J. Eng. Mater-T ASME*, 126, pp. 179-191.
- [23] Bandstra J. P., Koss D. A., *et al.*, 2006, "Modeling Void Coalescence during Ductile Fracture of a Steel," *Mater. Sci. Eng A-Struct.*, 366(2), pp. 269-281.
- [24] Grujicic M. and Dang P., 1995, "Computer Simulation of Martensitic Simulation of Martensitic Transformation in Fe-Ni Face-Centered Cubic Alloys," *Mater. Sci. Eng A-Struct.*, 201, pp. 194-204.
- [25] Suzuki T., Shimono M., *et al.*, 2006, "Study of Martensitic Transformation by Use of Mone-Carlo Method and Molecular Dynamics," *Mater. Sci. Eng A-Struct.*, 438-440, pp. 95-98.
- [26] Marian J., Wirth B. D., *et al.*, 2003, "MD Modeling of Defects in Fe and their Interactions," *J. Nucl. Mater.*, 323, pp. 181-191.
- [27] Zikry M. A., and Kao M., 1996, "Inelastic Microstructural Failure Mechanisms in Crystalline Materials with High Angle Grain Boundaries," *J. Mech. Phys. Solids*, 44(11), pp. 1765-1798.

[28] Ashmawi W. M., and Zikry M. A., 2000, "Effects of Grain Boundaries and Dislocation Density Evolution on Large Strain Deformation Modes in fcc Crystalline Materials," *J. Comput.-Aided Mater. Des.*, 7, pp. 55-62.

[29] Hatem T. M., and Zikry M. A., "Dislocation-Density Crystalline Plasticity Modeling of Lath Martensitic Microstructures in Steel Alloys," *Philos. Mag. A*, submitted.

[30] Hwang F. K., 1979, "An $O(n \log n)$ Algorithm for Rectilinear Minimal Spanning Trees," *J. Assoc. Comput. Mach.*, 26(2), pp. 177-182.

[31] Lee D. T., 1980, "Two Dimensional Voronoi Diagram in the L_p -Metric," *J. Assoc. for Comput. Mach.*, 27(4), pp. 604-618.

CHAPTER 10

RECOMMENDATIONS FOR FUTURE RESEARCH

The following are recommendations for future research:

- Develop in-situ TEM and AFM technique to characterize heterogeneous failure evolution in steels, and to use this to validate and advance the proposed computational techniques;
- Develop crack propagation numerical representation and growth criteria as a function of different microstructure variables, such as dislocation densities, temperature, shear slip, stresses, and rotation mismatch;
- Develop hierarchical multi-scale modelling approach for martensitic steels;
- Further study of microvoids and microcracks nucleation, growth and coalescence in three-dimensions;
- Extend the current methodology to study diffusionless phase transformation on materials;
- Use the current models to investigate other martensitic microstructures, such as shape memory alloys, and other microstructures in steels, such as bainite;
- Optimize the microstructure of different steels for tailored applications;

CHAPTER 2

MULTIPLE-SLIP CRYSTAL PLASTICITY CONSTITUTIVE FORMULATION

In this chapter, the formulation for the multiple-slip crystal plasticity rate-dependent constitutive relations, and the derivation of the evolutionary equations for the mobile and immobile dislocation densities, which are coupled to the multiple-slip crystalline formulation, are presented.

2.1 Multiple-Slip Crystal Plasticity Formulation

The crystal plasticity constitutive framework used in this study is based on the formulation developed in Zikry and Kao [1], Kameda and Zikry [2]. In that formulation, it has been assumed that the deformation gradient can be decomposed into elastic and inelastic components. The velocity gradient tensor, $V_{i,j}$, is related to the deformation gradient by

$$V_{i,j} = \dot{F}_{ij} F_{ij}^{-1}, \quad (2.1)$$

where $F_{i,l}$ is the total deformation gradient. And decomposing the velocity gradient, $V_{i,j}$, into its symmetric and skew-symmetric parts as

$$V_{i,j} = D_{ij} + W_{ij}, \quad (2.2)$$

where D_{ij} is the deformation rate tensor or stretching tensor,

$$D_{ij} = \frac{1}{2}(V_{i,j} + V_{j,i}), \quad (2.3)$$

and W_{ij} is the spin tensor or vorticity tensor,

$$W_{ij} = \frac{1}{2}(V_{i,j} - V_{j,i}). \quad (2.4)$$

The total deformation-rate tensor, D_{ij} , and the total spin tensor, W_{ij} , are then each additively decomposed into elastic and plastic components as

$$D_{ij} = D_{ij}^* + D_{ij}^P, \quad (2.5)$$

$$W_{ij} = W_{ij}^* + W_{ij}^P, \quad (2.6)$$

where W_{ij}^* includes the rigid body spin. The inelastic parts are defined in terms of the crystallographic slip-rates as

$$D_{ij}^P = P_{ij}^{(\alpha)} \dot{\gamma}^{(\alpha)}, \quad (2.7)$$

$$W_{ij}^P = \omega_{ij}^{(\alpha)} \dot{\gamma}^{(\alpha)}, \quad (2.8)$$

where α is summed over all slip-systems, and the tensors $P_{ij}^{(\alpha)}$ and $\omega_{ij}^{(\alpha)}$ are symmetric and skew-symmetric second-order tensors, and are defined in terms of the unit normals and the unit slip vectors as

$$P_{ij}^{(\alpha)} = \frac{1}{2} (s_i^{(\alpha)} n_j^{(\alpha)} + s_j^{(\alpha)} n_i^{(\alpha)}), \quad (2.9)$$

$$\omega_{ij}^{(\alpha)} = \frac{1}{2} (s_i^{(\alpha)} n_j^{(\alpha)} - s_j^{(\alpha)} n_i^{(\alpha)}), \quad (2.10)$$

where $n_i^{(\alpha)}$ is the unit vector normal to the slip plane, and $s_i^{(\alpha)}$ is the unit vector in the slip direction.

The elastic response can be expressed in terms of a hypoelastic law

$$\dot{\sigma}_{ij}^{\Delta^*} = L_{ijkl} D_{kl}^*, \quad (2.11)$$

where L_{ijkl} is the fourth-rank elasticity tensor with Voigt symmetry and $\sigma_{ij}^{\Delta^*}$ is the Jaumann

rate of Cauchy stress, σ_{ij} , co-rotational with the lattice spin.

The objective stress rate used here, us given by

$$\overset{\Delta^*}{\sigma}_{ij} = \dot{\sigma}_{ij} - W_{ik}^* \sigma_{kj} - W_{kj}^* \sigma_{ki}, \quad (2.12)$$

where $\dot{\sigma}_{ij}$ is material time-derivative of Cauchy stress.

The objective stress rate, $\overset{\Delta}{\sigma}_{ij}$, co-rotational to the material element can be derived as

$$\overset{\Delta}{\sigma}_{ij} = L_{ijkl} (D_{kl} - D_{kl}^P) - W_{ik}^P \sigma_{kj} - W_{jk}^P \sigma_{ki}, \quad (2.13)$$

where L_{ijkl} are the elastic moduli and for elastic isotropy can be expressed as

$$L_{ijkl} = \mu(\delta_{ik}\delta_{jl} + \delta_{jk}\delta_{il}) + \lambda\delta_{ij}\delta_{kl}, \quad (2.14)$$

where δ_{ij} is the Kronecker delta and λ and μ are the Lamé constants.

For a rate dependent inelastic formulation, the slip rates are functions of the resolved shear and reference stresses and a power law formulation (Hutchinson [3])

$$\dot{\gamma}^{(\alpha)} = \dot{\gamma}_{ref}^{(\alpha)} \left[\frac{\tau^{(\alpha)}}{\tau_{ref}^{(\alpha)}} \right] \left[\left| \frac{\tau^{(\alpha)}}{\tau_{ref}^{(\alpha)}} \right| \right]^{\frac{1}{m}-1} \quad \text{no sum on } \alpha, \quad (2.15)$$

is used here. The reference shear strain rate, $\dot{\gamma}_{ref}^{(\alpha)}$, corresponds to a reference shear stress, $\tau_{ref}^{(\alpha)}$. The exponent m describes the material rate sensitivity and is given by

$$m = \frac{\partial \ln \tau^{(\alpha)}}{\partial \ln \dot{\gamma}^{(\alpha)}}. \quad (2.16)$$

In other words, m is the ratio of the rate of change of the resolved shear stress on each slip system to the logarithmic rate of change of the slip rate on each slip system. For shear slip rates smaller than a critical value, the lattice motion is thermally activated. The rate sensitivity parameter is much less than one for values of the shear slip rate smaller than a critical value (see, for example, Follansbee *et al.* [4]). The rate sensitivity parameter is approximately equal to one for slip rates greater than the critical slip rate, and this flow is characterized by drag controlled dislocation motion. The rate independent limit is achieved as m approaches zero. For multiple slip, γ , is taken as the sum of the accumulated plastic strains on all slip systems, n ,

$$\gamma = \sum_{\alpha=1}^n |\gamma^{(\alpha)}|, \quad (2.17)$$

where $\tau^{(\alpha)}$ is the resolved shear stress and is given in terms of the Cauchy stress by

$$\tau^{(\alpha)} = P_{ij}^{(\alpha)} \sigma_{ij}. \quad (2.18)$$

From the balance of energy, with no thermal conduction, the time rate of change of temperature is related to the rate of the plastic work by

$$\dot{T} = \frac{\chi}{\rho c_p} \sigma'_{ij} D_{ij}^p, \quad (2.19)$$

where χ is the fraction of the plastic work converted to heat, σ'_{ij} , is the deviatoric stress, ρ is the material density, and c_p is the specific heat of the material. Due to the high strain rate deformation of the crystal, the rate of change of temperature is strictly a function of adiabatic heating.

2.2 Evolutionary Equations for the Mobile and Immobile Dislocation Densities

To gain a more fundamental understanding of dislocation motion, interaction, and transmission on material failure modes, the crystal plasticity constitutive formulations is coupled to internal variables that account for a local description of the dislocation structure in each crystal. Specifically, the mobile and the immobile dislocation densities have been used

as the internal variables in the present constitutive formulation. In inelastic deformations, the characteristics of the microstructure are governed by the mechanisms of dislocation production and dynamic recovery. As the material is strained, immobile dislocations are stored in each crystal, and these dislocations act as obstacles for evolving mobile dislocations. Therefore, the immobile and mobile dislocation densities can be coupled, due to the continuous immobilization of mobile dislocations.

The reference stress, on each slip system, can be given as a function of $\rho_{im}^{(\alpha)}$, the immobile dislocation density. The reference stress that is used here is a modification of widely used classical forms (see, for example, Mughrabi [5]) that related the reference stress to a square root dependence on the dislocation density as

$$\tau_{ref}^{(\alpha)} = \tau_y^{(\alpha)} + Gb \sum_{\xi=1}^{12} a_{\xi} \sqrt{\rho_{im}^{(\alpha)}}, \quad (2.20)$$

where G is the shear modulus, b is the magnitude of the Bergers vector, $\tau_y^{(\alpha)}$ is the static yield stress, and the coefficients, a_{ξ} ($\xi = 1,12$) are interaction coefficients, and generally have a magnitude of unity.

Now consider a given state for a deformed material, which has a dislocation structure of total dislocation density, $\rho^{(a)}$. This total dislocation density is assumed to be additively

decomposed, into a mobile dislocation density, $\rho_m^{(\alpha)}$, and an immobile dislocation density, $\rho_{im}^{(\alpha)}$, as

$$\rho^{(\alpha)} = \rho_m^{(\alpha)} + \rho_{im}^{(\alpha)}. \quad (2.21a)$$

Following the approach of Gottstein and Argon [6], we have assumed that during an increment of strain, an immobile dislocation density rate is generated, which will be denoted by $\dot{\rho}_{im}^{(\alpha)+}$, and an immobile dislocation density rate is annihilated, which will be denoted by $\dot{\rho}_{im}^{(\alpha)-}$ on each slip system as

$$\frac{d\rho_{im}^{(\alpha)}}{dt} = \dot{\rho}_{im}^{(\alpha)+} + \dot{\rho}_{im}^{(\alpha)-}. \quad (2.21b)$$

It is assumed that $\dot{\rho}_m^{(\alpha)+}$ corresponds to a generation of mobile dislocation densities, and $\dot{\rho}_m^{(\alpha)-}$ corresponds to an annihilation of mobile dislocation densities as

$$\frac{d\rho_m^{(\alpha)}}{dt} = \dot{\rho}_m^{(\alpha)+} + \dot{\rho}_m^{(\alpha)-}. \quad (2.21c)$$

The balance between dislocation generation and annihilation, equations (2.21b-c), is the basis for the evolution of mobile and immobile dislocation densities as a function of

strain. Plastic deformation of the crystal is assumed to begin with the easy glide stage, stage I. In this stage, most of the dislocations belong to the primary slip system, and very little slip takes place on secondary slip systems. In this stage, dislocation densities are comparatively low, and the details of dislocation interaction and accumulation have been substantiated by TEM and other high-resolution methods. In the second stage of hardening (stage II), secondary slip systems are activated, and dislocation clusters and cell walls begin to form. The third stage of hardening is characterized by the annihilation and the rearrangement of dislocations. For a detailed experimental overview of dislocation emission, interaction, trapping, and annihilation for the three hardening stages in fcc materials, see, for example, Mitchell [7]; Anongba *et al.* [8, 9]; Argon and Haasen [10].

In stage I, dipoles and multipoles are formed after mobile dislocations emitted from a source are trapped by dislocations of opposite signs on parallel slip planes. The back stress at the source is due to the dislocation emitted by the source. If the flow stress is greater than this back stress, the source will continue to emit dislocations, and dislocations that are trapped can break free. A large number of dipoles, multipoles, and loops are formed in easy glide by forest interactions, cross-slip around obstacles, and interactions between dislocations on parallel slip planes. Dipoles and multipoles occur in well-spaced clusters, thus allowing primary dislocations to glide over long distances. Using the equation (2.21c), this is given by

$$\frac{d\rho_m^{(\alpha)}}{dt} = \text{rate of generation.} \quad (2.22)$$

The rate of dislocation generation is proportional to the distance traveled by the emitted dislocations from a dislocation source with density $\rho_{source}^{(\alpha)}$. This distance, y_{back} , is related to the decrease of the back stress on the dislocation density source, $\rho_{source}^{(\alpha)}$, after previously emitted dislocations have traveled this distance y_{back} . Hence, equation (2.22) can be written as

$$\frac{d\rho_m^{(\alpha)}}{dt} = \rho_{source}^{(\alpha)} \frac{\bar{v}}{y_{back}}, \quad (2.23)$$

where \bar{v} is mobile dislocation average velocity. Using Orwan's equation,

$$\dot{\gamma}^{(\alpha)} = \rho_m^{(\alpha)} b \bar{v}, \quad (2.24)$$

and equation (2.23), we obtain the following equations:

$$\frac{d\rho_m^{(\alpha)}}{d\gamma} = \frac{g_{source}}{b^2} \left(\frac{\rho_{im}^{(\alpha)}}{\rho_m^{(\alpha)}} \right), \quad (2.25)$$

where b is the modulus of the Burgers vector, g_{source} is a coefficient pertaining to an increase in the mobile dislocation density due to dislocation sources.

In stage II, dipole clusters multiply and join together, so that primary glide dislocations are effectively blocked. Hardening increases in this stage are due to an increase in dislocation tangles. The forest dislocations of these systems serve as obstacles for the primary dislocations. The mobile dislocations are immobilized with a mean free path proportional to $(\rho_{im}^{(\alpha)})^{-1/2}$. Spatially organized forest structures and tangles such as Frank nets, cell walls, or sub-boundaries can act as immobilization sites at this stage of the deformation. Also thermally activated cross slip can block the glide dislocations. Since the rate of trapping is related to an increase in rate of growth of immobile dislocations, using equation (2.22), the coupled mobile and immobile dislocation density evolution equations for this stage are given by

$$\frac{d\rho_m^{(\alpha)}}{d\gamma} = -\frac{g_{immob}}{b} \sqrt{\rho_{im}^{(\alpha)}} - \frac{g_{minter}}{b^2} \exp\left(-\frac{H}{\kappa T}\right), \quad (2.26)$$

$$\frac{d\rho_{im}^{(\alpha)}}{d\gamma} = \frac{g_{immob}}{b} \sqrt{\rho_{im}^{(\alpha)}} + \frac{g_{minter}}{b^2} \exp\left(-\frac{H}{\kappa T}\right), \quad (2.27)$$

where b is the modulus of the Burgers vector, g_{immob} is a coefficient related to the immobilization of mobile dislocations, and g_{minter} is a coefficient related to the trapping of mobile dislocations due to thermally activated cross-slip.

At moderate and large strains, dynamic recovery characterizes the stage III. At temperatures lower than 0.4 of the melting temperature, the main mechanism of recovery is

annihilation of the screw segments of opposite signs on the expanding dislocation loops. The evolution for the immobile dislocation density for this stage is

$$\frac{d\rho_{im}^{(\alpha)}}{d\gamma} = -g_{recov} \exp\left(-\frac{H}{\kappa T}\right) \rho_{im}^{(\alpha)}, \quad (2.28)$$

where g_{recov} is a coefficient related to the rearrangement and annihilation of immobile dislocations.

Equations (2.25-2.28) can be combined to obtain a coupled set of nonlinear evolutionary equations

$$\frac{d\rho_m^{(\alpha)}}{dt} = \dot{\gamma}^{(\alpha)} \left[\frac{g_{sour}}{b^2} \left(\frac{\rho_{im}^{(\alpha)}}{\rho_m^{(\alpha)}} \right) - \frac{g_{minter}}{b^2} \exp\left(-\frac{H}{\kappa T}\right) - \frac{g_{immob}}{b} \sqrt{\rho_{im}^{(\alpha)}} \right], \quad (2.29)$$

$$\frac{d\rho_{im}^{(\alpha)}}{dt} = \dot{\gamma}^{(\alpha)} \left[\frac{g_{minter}}{b^2} \exp\left(-\frac{H}{\kappa T}\right) + \frac{g_{immob}}{b} \sqrt{\rho_{im}^{(\alpha)}} - g_{recov} \exp\left(-\frac{H}{\kappa T}\right) \rho_{im}^{(\alpha)} \right], \quad (2.30)$$

where g_{sour} is a coefficient pertaining to an increase in the mobile dislocation density due to dislocation sources, g_{minter} is a coefficient related to the trapping of mobile dislocations due to forest intersections, cross-slip around obstacles, or dislocation interactions, g_{recov} is a coefficient related to the rearrangement and annihilation of immobile dislocations, g_{immob} is a

coefficient related to the immobilization of mobile dislocations, H is the activation enthalpy, and κ is Boltzmann's constant. As these evolutionary equations indicate, the dislocation activities related to recovery and trapping are coupled to thermal activation. The thermal activation energy temperature is updated as a function of the energy given by (2.19).

2.3 Determination of the Coefficients for the Coupled Evolutionary Equations

To couple the evolutionary equations to the crystal plasticity formulations, the four g coefficients in (2.29-2.30), and the enthalpy, H , must be determined as functions of the deformation mode. The enthalpy, H , is determined by defining an exponential ratio of the current temperature to the reference temperature, following Paidar *et al.* [11], a form of activation enthalpy for cross-slip which accounts the cross-slip effects. The four g coefficients are determined using two general conditions, pertinent to the evolution of dislocation densities in crystalline materials, have been used:

- (i) that the mobile and immobile dislocation densities saturate at large strains;
- (ii) that the relaxation of the mobile dislocation density to a quasi-steady state value occurs much faster than the variation of the immobile dislocation density.

The conditions are invoked based on the arguments by Mecking and Kocks [12], Walgraef and Aifantis [13-16], and Kubin and Estrin [17, 18]. They used similar arguments to determine coefficients in equations pertaining to the evolution of mobile and immobile dislocation densities. The saturation of both the immobile and mobile dislocation densities at large strains and their different quasi-steady values in fcc materials have been

experimentally substantiated by several investigators (see, for example, Mughrabi [5], Bay *et al.* [19], and Hansen [20]). For a detailed presentation, see to Zikry and Kao [1, 21] and Kameda and Zikry [22].

REFERENCES

- [1] Zikry M. A., and Kao M., 1996, "Inelastic Microstructural Failure Mechanisms in Crystalline Materials with High Angle Grain Boundaries," *J. Mech. Phys. Solids*, 44(11), pp. 1765-1798.
- [2] Kameda T., and Zikry M. A., 1998, "Intergranular and Transgranular Crack Growth at Triple Junction Boundaries in Ordered Intermetallics," *Int. J. Plast.*, 14(8), pp. 689-702.
- [3] Hutchinson J. W., 1976, "Bounds and Self-Consistent Estimates for Creep of Polycrystalline Materials," *P. Roy. Soc. A-Math. Phys.*, 348(1652), pp. 101-127.
- [4] Magnusen P.E., Follansbee P. S., and Koss D. A., 1984, "The Effect of Strain Rate on the Deformation and Fracture-Behavior of Ductile Metals Containing Porosity," *J. Metals*, 36(7), pp. 54-54.
- [5] Mughrabi H., 1987, "A 2-Parameter Description of Heterogeneous Dislocation Distributions in Deformed Metal Crystals," *Mater. Sci. Eng.*, 85(1-2), pp. 15-31.
- [6] Gottstein G. and Argon A. S., 1987, "Dislocation Theory of Steady-State Deformation and Its Approach in Creep and Dynamic Tests," *Acta Metall. Mater.*, 35(6), pp. 1261-1271.
- [7] Mitchell W. I., 1964, "The Precipitation Behaviour of a Complex Nickel-Base Alloy," *Zeitschrift Fur Metallkunde*, 55(10), pp. 613-616.
- [8] Anongba P. N. B., Bonneville J., and Martin J. L., 1993, "Hardening Stages of 112 Copper Single-Crystals at Intermediate and High-Temperatures: I. Mechanical-Behavior," *Acta Metall. Mater.*, 41(10), pp. 2897-2906.

- [9] Anongba P.N.B., Bonneville J., and Martin J. L., 1993, "Hardening Stages of 112 Copper Single-Crystals at Intermediate and High-Temperatures: II. Slip Systems and Microstructures," *Acta Metall. Mater.*, 41(10): p. 2907-2922.
- [10] Argon A.S. and Haasen P., 1993, "A New Mechanism of Work-Hardening in the Late Stages of Large-Strain Plastic-Flow in Fcc and Diamond Cubic-Crystals," *Acta Metall. Mater.*, 41(11), pp. 3289-3306.
- [11] Paidar V., Pope D. P., and Vitek V., 1984, "A Theory of the Anomalous Yield Behavior in L12 Ordered Alloys," *Acta Metall. Mater.*, 32(3), pp. 435-448.
- [12] Mecking H. and Kocks U. F., 1981, "Kinetics of Flow and Strain-Hardening," *Acta Metall. Mater.*, 29(11), pp. 1865-1875.
- [13] Walgraef, D. and E. C. Aifantis, 1985, "On the Formation and Stability of Dislocation Patterns: I. One-Dimensional Considerations," *Int. J. Eng. Sci.*, 23(12), pp. 1351-1358.
- [14] Walgraef, D. and E. C. Aifantis, 1985, "On the Formation and Stability of Dislocation Patterns: II. Two-Dimensional Considerations," *Int. J. Eng. Sci.*, 23(12), pp. 1359-1364.
- [15] Walgraef, D. and E. C. Aifantis, 1985, "On the Formation and Stability of Dislocation Patterns: III. 3-Dimensional Considerations," *Int. J. Eng. Sci.*, 23(12), pp. 1365-1372.
- [16] Walgraef, D. and E.C. Aifantis, 1985, "Dislocation Patterning in Fatigued Metals as a Result of Dynamical Instabilities," *J. Appl. Phys.*, 58(2), pp. 688-691.
- [17] Estrin Y. and Kubin L. P., 1988, "Plastic Instabilities - Classification and Physical-Mechanisms," *Res Mechanica*, 23(2-3), pp. 197-221.
- [18] Kubin L. P. and Estrin Y., 1988, "Strain Nonuniformities and Plastic Instabilities," *Revue De Physique Appliquee*, 23(4), pp. 573-583.

[19] Bay B., Hansen N., *et al.*, 1992, "Evolution of F.C.C. Deformation Structures in Polyslip," *Acta Metall. Mater.*, 40, pp. 205-219.

[20] Hansen N., 1990, "Cold Deformation Microstructures," *Mater. Sci. Technol.*, 6, pp. 1039-1047.

[21] Zikry M.A. and Kao M., 1996, "Dislocation Based Multiple-Slip Crystalline Constitutive Formulation for Finite-Strain Plasticity. *Scripta Mater.*, 34(7), pp. 1115-1121.

[22] Zikry M.A. and Kameda T., 1998, "Inelastic Three Dimensional High Strain-Rate Dislocation Density Based Analysis of Grain-Boundary Effects and Failure Modes in Ordered Intermetallics," *Mech. Mater.*, 28(1-4), pp. 93-102.

CHAPTER 3

MARTENSITIC MICROSTRUCTURAL REPRESENTATION

The martensitic microstructure has to be accurately represented in terms of crystalline structure, orientation, morphology, secondary-phases, such as retained austenite and inclusions, and transformation dislocation-densities. As experimentally noted by several investigators [1-14], these dominant interrelated characteristics are needed to account for the martensitic microstructure, since they collectively have a significant interrelated role in understanding and predicting behaviour at different physical scales. The representation of each of these characteristics is outlined in the following subsections.

3.1 Crystalline Structure of Heterogeneous Microstructure of Martensite

In the current study, the martensitic phase will be represented as (b.c.t./b.c.c.) with twenty four potential slip-systems with $\{110\}$ and $\{112\}$ slip-planes of for easy and pencil glide, and slip directions of $\langle 111 \rangle$, see, for example, Franciosi [15], Stainier *et al.* [16]. The slip normal to the slip plane and the slip direction vectors are given in the Table 3.1.

The austenitic phase will be represented as an f.c.c. structure with twelve potential slip-systems with habit planes of $\{111\}$ and slip directions of $\langle 110 \rangle$, see for example Taylor [17], and Franciosi and Zaoui [18]. The slip normal to the slip plane and the slip direction vectors are given in the Table 3.2.

The MnS inclusions will be represented as a NaCl like structure with six potential slip-systems with slip planes of $\{110\}$ and slip directions of $\langle 110 \rangle$, see Mardinly *et al.* [19] and Matsuno *et al.* [20]. The slip normal to the slip plane and the slip direction vectors are given in the Table 3.3.

3.2 Martensitic Orientation

For the crystalline plasticity formulation, the product phase martensite must be related to the global coordinates through a parent austenite grain orientation and variant orientations. Commonly accepted ORs for lath martensitic steels are Kurdjumov-Sachs (K-S) and Nishiyama-Wassermann (N-W) ORs as given by [21].

K-S ORs are based on a γ austenite transformation to an α' martensitic transformation as $(111)_\gamma // (011)_{\alpha'}$, $[\bar{1}01]_\gamma // [\bar{1}\bar{1}\bar{1}]_{\alpha'}$. For an N-W OR, the transformation is based on

$(111)_\gamma // (011)_{\alpha'}$, $[\bar{1}\bar{1}2]_\gamma // [0\bar{1}1]_{\alpha'}$ relation, which is a K-S OR with a 5.12° degree rotation around the $[011]_\gamma$ direction. Investigations by Wayman [7-9] and Morito [10, 11] have clearly indicated that martensitic steel alloys generally have intermediate ORs that are between K-S and N-W ORs. As can be seen from Table 3.4, twenty four variants can be obtained for K-S ORs, or twelve pairs where every pair relates with low angle boundary, e.g. variant #1 and variant #4 as in Figure 3.1.

A martensitic transformation is a military transformation, where atoms have a fixed relation to each other during the transformation. Martensitic transformations are diffusionless, as it usually occurs at high speed and/or low temperatures, which mandate glissile interfaces between parent and product phases. This interface is the habit plane [35]. The orientation of the habit planes is critical in determining the appropriate martensitic orientations relative to the parent austenite phase. Wayman [9], Kelly [15] and Maki *et al.* [10,11] have identified $(557)_\gamma$ plane as lath martensite's habit plane.

As noted earlier, an essential aspect of representing martensitic texture is to relate the martensitic b.c.c. local grain orientation to the global orientation. Three transformations are needed. The first transformation, $[T]_1$, relates an observed OR to a theoretical OR, such as

K-S and N-W ORs. The second transformation, $[T]_2$, relates a martensite OR to the parent austenite grain orientation. The third transformation, $[T]_3$, relates the austenite grain orientation to the global coordinates. These transformations are given by

$$[X]_{\text{Global}} = [T]_3 * [T]_2 * [T]_1 * [X]_{\alpha'} \quad (3.1)$$

Variants are usually deviated from theoretical ORs with random or fixed angles. The first transformation transforms observed martensitic coordinates to a martensitic orientation, such as KS or NW, as

$$[X]_{\text{th } \alpha'} = [T]_1 * [X]_{\text{Ob } \alpha'} \quad (3.2)$$

For example, observed orientations for lath martensite $[9-11]$ can be represented as a misorientation from $[011]_y$ in K-S OR with an angle ϕ , and can be represented as

$$\begin{bmatrix} t/2+c & -s/\sqrt{2} & t/2 \\ s/\sqrt{2} & c & -s/\sqrt{2} \\ t/2 & s/\sqrt{2} & t/2+c \end{bmatrix}, \quad (3.3)$$

where $s = \sin(\phi)$, $c = \cos(\phi)$, and $t = 1 - \cos(\phi)$, and ϕ generally varies between 0° and 5.12° degree for lath martensitic steels.

The second transformation is the theoretical transformation between the product martensitic phase and the parent austenitic phases, such as the KS OR. The second order tensor for the transformation is obtained utilizing the OR for the invariant plane and axis for each variant. A matrix with an orthogonal parallel system of axes can be used for both parent and product phases since $[X]_\gamma = [T]_2 * [X]_\alpha$ and therefore $[T]_2 = [X]_\alpha^{-1} * [X]_\gamma$. For the first variant in Table 3.4, we have

$$[X]_\gamma = \begin{bmatrix} 1/\sqrt{3} & -1/\sqrt{2} & 1/\sqrt{3} \\ 1/\sqrt{3} & 0 & -2/\sqrt{6} \\ 1/\sqrt{3} & 1/\sqrt{2} & 1/\sqrt{2} \end{bmatrix}, \text{ and } [X]_\alpha = \begin{bmatrix} 0 & -1/\sqrt{3} & 2/\sqrt{6} \\ 1/\sqrt{2} & -1/\sqrt{3} & -1/\sqrt{6} \\ 1/\sqrt{2} & 1/\sqrt{3} & 1/\sqrt{2} \end{bmatrix}, \quad (3.4)$$

and,

$$[T]_2 = \begin{bmatrix} 0.7416 & 0.6498 & 0.1667 \\ -0.6667 & 0.7416 & 0.0749 \\ -0.0749 & -0.1667 & 0.9832 \end{bmatrix} \quad (3.5)$$

Similar transformations can be obtained for all 24 variants related to K-S ORs as presented in Table 3.4.

The third transformation pertains to the austenite orientation relative to the global axis and the loading directions. Such a transformation is usually represented as three independent Euler angles, where $[T]_3$ can be obtained. Another approach is similar to the approach utilized to obtain $[T]_2$; $[X]_G = [T]_3 * [X]_\gamma$, and $[T]_3 = [X]_\gamma^{-1} * [X]_G$. For example, to align the load with $(111)_\gamma$ and $[-110]_\gamma$, where $[010]_G // [111]_\gamma$, $[001]_G // [-110]_\gamma$, and $[-110]_\gamma \times [111]_\gamma // [100]_G$, the transformation would be

$$[X]_\gamma = \begin{bmatrix} 1/\sqrt{6} & 1/\sqrt{3} & -1/\sqrt{2} \\ -1/\sqrt{6} & 1/\sqrt{3} & 1/\sqrt{2} \\ -2/\sqrt{6} & 1/\sqrt{3} & 0 \end{bmatrix}, \text{ and } [X]_G = \begin{bmatrix} 1 & 0 & 0 \\ 0 & 1 & 0 \\ 0 & 0 & 1 \end{bmatrix}, \quad (3.6)$$

then

$$[T]_3 = \begin{bmatrix} -0.4083 & -0.4083 & 0.8165 \\ 0.5774 & 0.5774 & 0.5774 \\ -0.7071 & 0.7071 & 0.0 \end{bmatrix}, \quad (3.7)$$

and the final transformation to the global axis can be calculated as in equation 3.1.

3.3 Morphology: Variant Arrangement and Distribution

Another unique characteristic of martensitic microstructure is the fine structure of laths, which are the building cells of the martensitic microstructure. The lath long direction is oriented along $[011]_p$, as illustrated in Figure 3.2. A typical lath geometry is $0.3 \times 2.8 \times 100 \mu\text{m}$ [8]. The change in lath width is small relative to the change in the parent austenite grain [14].

To characterize the complex martensitic microstructure that occurs on different length scales, we will follow what Morito *et al.* [10-14] have proposed based on SEM and EBSD characterization. Specifically, we will designate a block as a group of laths with low angle

misorientations, and a packet as a collection of blocks with the same habit plane (Figure 3.3). Blocks will have irregular shapes, although it can be observed that the smallest dimension will be in the direction normal to the habit plane, and block widths can vary between 0.7-8 μm [7, 14]. Using this methodology, we can use the ORs and original austenite orientations to model different variant orientations for different blocks and packets arrangements. Packets can have irregular shapes as well, although the stacking direction of variants is assumed parallel to the habit plane direction. Packet sizes can be approximated as a linear function of prior austenite grain size, and can vary between 0.7-150 μm , see [14] for more details. Due to the microstructural scale that we use in this investigation, the martensitic block is assumed as the smallest scale. Furthermore, as noted by Morito *et al.* [4] martensitic properties are more likely to be related to block size interfacial orientations. In this study, a single parent austenite grain will be considered to further elucidate how grain orientation, packets, and blocks affect mechanical properties and large strain deformation response.

3.4 Secondary-Phases Structures

Secondary-phases microstructures are frequently observed in high strength steels, i.e. inclusions, retained austenite. Inclusion can have several chemical decomposition in high-strength martensitic steels; most common in High-Strength Low Alloys (HSLA) steels is MnS, see, for example, [22-25]. Inclusions have small percentages, commonly less than 0.05%. Inclusions decomposition, size, percentage and spacing play a major role in failure properties of the steels under tension, [22-25]. In the current study, MnS inclusion is presented in martensitic microstructure to study their effect on shear localization and inelastic deformation under compressive loadings.

As it is well known, a small amount of retained austenite (approximately 5%) is frequently observed between the martensitic aggregates after the martensitic transformation, see, for example, [3, 5, 6]. In the current study, these effects will be investigated by a random distribution of f.c.c. retained austenite within the b.c.c. aggregates.

3.5 Transformation Dislocations Densities

Martensitic transformation is usually accompanied by large dislocation-densities, see, for example, [13]. These high dislocation-densities are necessary to accommodate the phase transformation and the subsequent glissile interface. Wayman [9] classified the dislocations in martensitic microstructure as two basic types, transformation and interface dislocations. The transformation dislocations are screw dislocation in all four $\langle 111 \rangle_{\alpha'}$ direction, with $a/2 [\bar{1}\bar{1}1]_{\alpha'}$ as the dominant direction. Morito *et al.* [13] conducted several experimental studies to characterize the dislocation-densities in nickel and carbon based steels with varying composition. Approximate dislocation-densities of the value of $3.8 \times 10^{14} \text{ m}^{-2}$ were obtained for low-nickel lath martensitic steels (Fe-11Ni) [13].

The percentages of mobile to immobile dislocation-densities ratio were not obtained by these studies, as it is difficult to obtain these values experimentally. The initial mobile and immobile dislocations incorporated in the current study were obtained from numerical models based on a proposed transformation crystalline plasticity model [26].

REFERENCES

- [1] Krauss G., 2001, "Deformation and Fracture in Martensitic Carbon Steels Tempered at Low Temperature," *Metall. Mater. Trans. A*, 32B, pp. 205-221.
- [2] Saeglitz M., and Krauss G., 1997, "Deformation, Fracture, and Mechanical Properties of Low-Temperature-Tempered Martensite in SAE 43xx Steels," *Metall. Mater. Trans.*, A 28A, pp. 377-387.
- [3] Nakagawa H. and Miyazaki T., 1999, "Effect of Retained Austenite on the Microstructure and Mechanical Properties of Martensitic Precipitation Hardening in Stainless Steel," *J. Mater. Sci.*, 34, pp. 3901-3908.
- [4] Morito S., Yoshida H., *et al.*, 2006, "Effect of Block Size on the Strength of Lath Martensite in Low Carbon Steels," *Mater. Sci. Eng A-Struct.*, 438-40, pp. 237-240.
- [5] Thomas G., 1978, "Retained Austenite and Tempered Martensite Embrittlement," *Metall. Trans. A*, 9A, pp. 439-450.
- [6] McMahon J. A. and Thomas G., 1973, *Proceedings of the 3rd International Conference on the Strength of Metals and Alloys*, Institution of Metals, London, pp. 180-184.

- [7] Wasaka W. and Wayman C. M., 1981, The Morphology and Crystallography of Ferrous Lath Martensite. Studies of Fe-20%Ni-5%Mn-I, II, III,” *Acta Metall.*, 29, pp. 973-990, 991-1011, 1013-1028.
- [8] Wasaka W. and Wayman C. M., 1981, “Crystallography and Morphology of Ferrous Lath Martensite,” *Metallography*, 14, pp. 49-60.
- [9] Sandvik B. P. J. and Wayman C. M., 1983, “Characteristics of Lath Martensite, I, II, III,” *Metall. Trans. A*, 14A, pp. 809-822, 823-834, 835-844.
- [10] Morito S., Huang X., *et al.*, 2006, “The Morphology and Crystallography of Lath Martensite in Alloys Steels,” *Acta Mater.*, 54, pp. 5323-5331.
- [11] Morito S., Tanaka H., 2003, *et al.*, “The Morphology and Crystallography of Lath Martensite in Fe-C Alloys,” *Acta Mater.*, 51, pp. 1789-1799.
- [12] Morito S., Kishida I. and Maki T., 2003, “Microstructure of Ausformed Lath Martensite in 18%Ni Maraging Steel,” *J. Phys. IV France*, 112, pp. 453-456.
- [13] Morito S., Nishikawa J., *et al.*, 2003, “Dislocation Density within Lath Martensite in Fe-C and Fe-Ni Alloys,” *ISIJ Int.*, 43(9), pp. 1475-1477.
- [14] Morito S., Saito H. *et al.*, 2005, “Effect of Austenite Grain Size on the Morphology and Crystallography of Lath Martensite in Low Carbon Steels,” *ISIJ Int.*, 45(1), pp. 91-94.

- [15] Franciosi P., 1983, "Glide Mechanisms in B.C.C. Crystals: An Investigation of the Case of Alfa Iron Through Multislip and Latent Hardening Test," *Acta Metall.*, 31(9), pp. 1331-1342.
- [16] Stainier L., Cuitino A. M. and Ortiz M., 2002, "A Micromechanical Model of Hardening, Rate Sensitivity and Thermal Softening in B.C.C. Single Crystal," *J. Mech. Phys. Solids*, 50, pp. 1511-1545.
- [17] Taylor G. I., 1934, "The Mechanism of Plastic Deformation in Crystals – I, II," *Proc. R. Soc. Lond. A*, 145, pp. 362-387, 388-404.
- [18] Franciosi P. and Zaoui A., 1982, "Multislip in F.c.c. Crystals a Theoretical Approach Compared with Experimental Data," *Acta Metall.*, 30, pp. 1627-1637.
- [19] Mardinly A. J., Van Vlack L. H., and Hosford W. F., 1993, "Referred Orientation of MnS Inclusions in Rolled Steel," *Texture Microstruct*, 22, pp. 127-138.
- [20] Matsuno F., Nishikida S., and Ikesaki H., 1985, "Mechanical Properties of Manganese Sulphides in the Temperature Range between Room Temperature and 1000 °C," *Trans. ISIJ*, 25, pp. 989-998.
- [21] Bhadeshia H. K. D. H., 2001, *Worked Examples in the Geometry of Crystals*. The institute of metals, London.
- [22] Garrison W. M., and Moody N. R., 1987, "Ductile Fracture," *J. Phys. Chem.*

Solids, 48(11), pp. 1035-1074.

[23] Lorio L. E., and Garrison W. M., 2002, "Effects of Gettering Sulfur as CrS or MnS on Void Generation Behavior in Ultra-High Strength Steel," *Scripta Mater.*, 46(12), pp. 863-868.

[24] Garrison W. M. and Wojcieszynski A. L., 2007, "A Discussion of the Effect of Inclusion Volume Fraction on the Toughness of Steel," *Mater. Sci. Eng A-Struct.*, 464, pp. 321-329.

[25] Minnaar K., and Zhou M., 1998, "An Analysis of the Dynamic Shear Failure Resistance of Structural Metal," *J. Mech. Phys. Solids*, 46-10, pp. 2155-2170.

[26] Hatem T. M. and Zikry M. A., 2009, *Scripta Mater.*, submitted (2009).

**Tables and Figures for
Chapter 3**

Table 3.1 Slip-systems of martensitic b.c.c. phase.

Slip-System #	Slip plane/direction	Slip-System #	Slip plane/direction
1	$(\bar{1}10)/[111]$	13	$(110)/[1\bar{1}\bar{1}]$
2	$(\bar{1}01)/[111]$	14	$(011)/[1\bar{1}\bar{1}]$
3	$(0\bar{1}1)/[111]$	15	$(\bar{1}01)/[1\bar{1}\bar{1}]$
4	$(11\bar{2})/[111]$	16	$(121)/[1\bar{1}\bar{1}]$
5	$(1\bar{2}1)/[111]$	17	$(\bar{1}12)/[1\bar{1}\bar{1}]$
6	$(\bar{2}11)/[111]$	18	$(21\bar{1})/[1\bar{1}\bar{1}]$
7	$(110)/[\bar{1}\bar{1}\bar{1}]$	19	$(101)/[11\bar{1}]$
8	$(101)/[\bar{1}\bar{1}\bar{1}]$	20	$(011)/[11\bar{1}]$
9	$(0\bar{1}1)/[\bar{1}\bar{1}\bar{1}]$	21	$(\bar{1}10)/[11\bar{1}]$
10	$(211)/[\bar{1}\bar{1}\bar{1}]$	22	$(112)/[11\bar{1}]$
11	$(1\bar{1}2)/[\bar{1}\bar{1}\bar{1}]$	23	$(2\bar{1}1)/[11\bar{1}]$
12	$(\bar{1}21)/[\bar{1}\bar{1}\bar{1}]$	24	$(\bar{1}21)/[11\bar{1}]$

Table 3.2 Slip-systems of austenitic f.c.c. phase.

Slip System #	Slip plane/direction	Slip System #	Slip plane/direction
1	$(111) / [01\bar{1}]$	7	$(\bar{1}\bar{1}1) / [011]$
2	$(111) / [\bar{1}01]$	8	$(\bar{1}\bar{1}1) / [10\bar{1}]$
3	$(111) / [1\bar{1}0]$	9	$(\bar{1}\bar{1}1) / [\bar{1}\bar{1}0]$
4	$(\bar{1}11) / [01\bar{1}]$	10	$(11\bar{1}) / [011]$
5	$(\bar{1}11) / [011]$	11	$(11\bar{1}) / [\bar{1}0\bar{1}]$
6	$(\bar{1}11) / [\bar{1}\bar{1}0]$	12	$(11\bar{1}) / [1\bar{1}0]$

Table 3.3 Slip-systems of MnS inclusions crystal structure.

Slip-System #	Slip plane/direction	Slip-System #	Slip plane/direction
1	$(\bar{1}10)/[110]$	4	$(110)/[\bar{1}\bar{1}0]$
2	$(\bar{1}01)/[101]$	5	$(101)/[\bar{1}0\bar{1}]$
3	$(0\bar{1}1)/[011]$	6	$(011)/[0\bar{1}\bar{1}]$

Table 3.4 The 24 variants corresponding to K-S OR and their numbering as used in the current study.

Variant #	Parallel Planes	Parallel Directions	Variant #	Parallel Planes	Parallel Directions
1	$(111)_\gamma // (011)_{\alpha'}$	$[\bar{1}01]_\gamma // [\bar{1}\bar{1}1]_{\alpha'}$	13	$(\bar{1}11)_\gamma // (011)_{\alpha'}$	$[0\bar{1}1]_\gamma // [\bar{1}\bar{1}1]_{\alpha'}$
2		$[\bar{1}01]_\gamma // [\bar{1}1\bar{1}]_{\alpha'}$	14		$[0\bar{1}1]_\gamma // [\bar{1}1\bar{1}]_{\alpha'}$
3		$[0\bar{1}1]_\gamma // [\bar{1}\bar{1}1]_{\alpha'}$	15		$[\bar{1}0\bar{1}]_\gamma // [\bar{1}\bar{1}1]_{\alpha'}$
4		$[0\bar{1}1]_\gamma // [\bar{1}1\bar{1}]_{\alpha'}$	16		$[\bar{1}0\bar{1}]_\gamma // [\bar{1}1\bar{1}]_{\alpha'}$
5		$[1\bar{1}0]_\gamma // [\bar{1}\bar{1}1]_{\alpha'}$	17		$[110]_\gamma // [\bar{1}\bar{1}1]_{\alpha'}$
6		$[1\bar{1}0]_\gamma // [\bar{1}1\bar{1}]_{\alpha'}$	18		$[110]_\gamma // [\bar{1}1\bar{1}]_{\alpha'}$
7	$(1\bar{1}1)_\gamma // (011)_{\alpha'}$	$[10\bar{1}]_\gamma // [\bar{1}\bar{1}1]_{\alpha'}$	19	$(11\bar{1})_\gamma // (011)_{\alpha'}$	$[\bar{1}10]_\gamma // [\bar{1}\bar{1}1]_{\alpha'}$
8		$[10\bar{1}]_\gamma // [\bar{1}1\bar{1}]_{\alpha'}$	20		$[\bar{1}10]_\gamma // [\bar{1}1\bar{1}]_{\alpha'}$
9		$[\bar{1}\bar{1}0]_\gamma // [\bar{1}\bar{1}1]_{\alpha'}$	21		$[0\bar{1}\bar{1}]_\gamma // [\bar{1}\bar{1}1]_{\alpha'}$
10		$[\bar{1}\bar{1}0]_\gamma // [\bar{1}1\bar{1}]_{\alpha'}$	22		$[0\bar{1}\bar{1}]_\gamma // [\bar{1}1\bar{1}]_{\alpha'}$
11		$[011]_\gamma // [\bar{1}\bar{1}1]_{\alpha'}$	23		$[101]_\gamma // [\bar{1}\bar{1}1]_{\alpha'}$
12		$[011]_\gamma // [\bar{1}1\bar{1}]_{\alpha'}$	24		$[101]_\gamma // [\bar{1}1\bar{1}]_{\alpha'}$

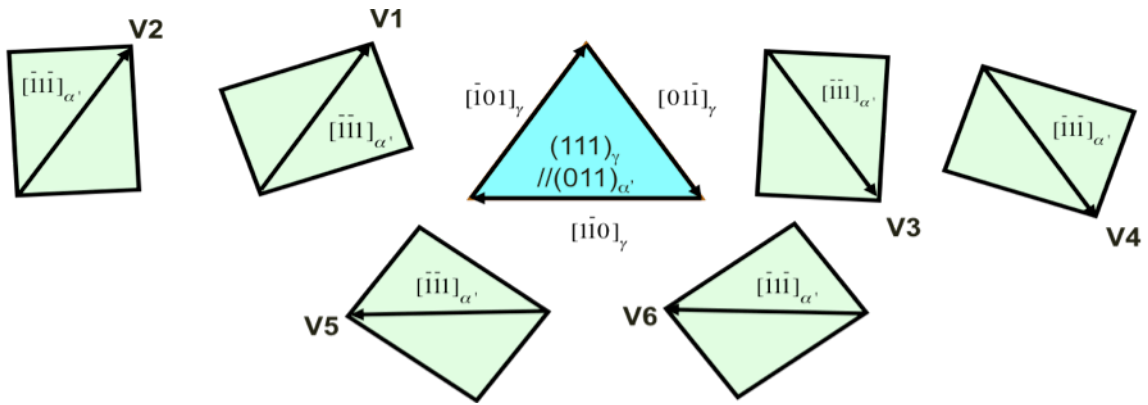


Figure 3.1 The relation between the austenite phase and the martensite phase for the six variants sharing $(111)_\gamma$ habit plane.

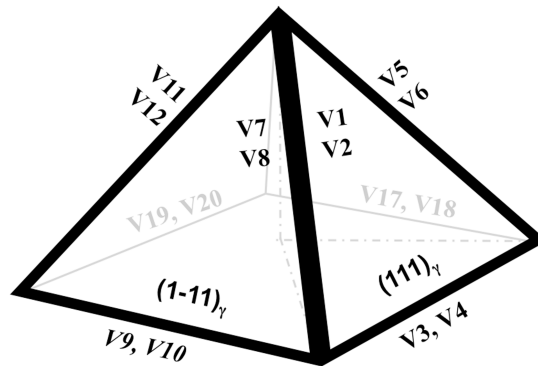


Figure 3.2 The alignment of variants in space, relative to each other and others planes. Three main relations can be identified, flat, sharp, and extended inward.

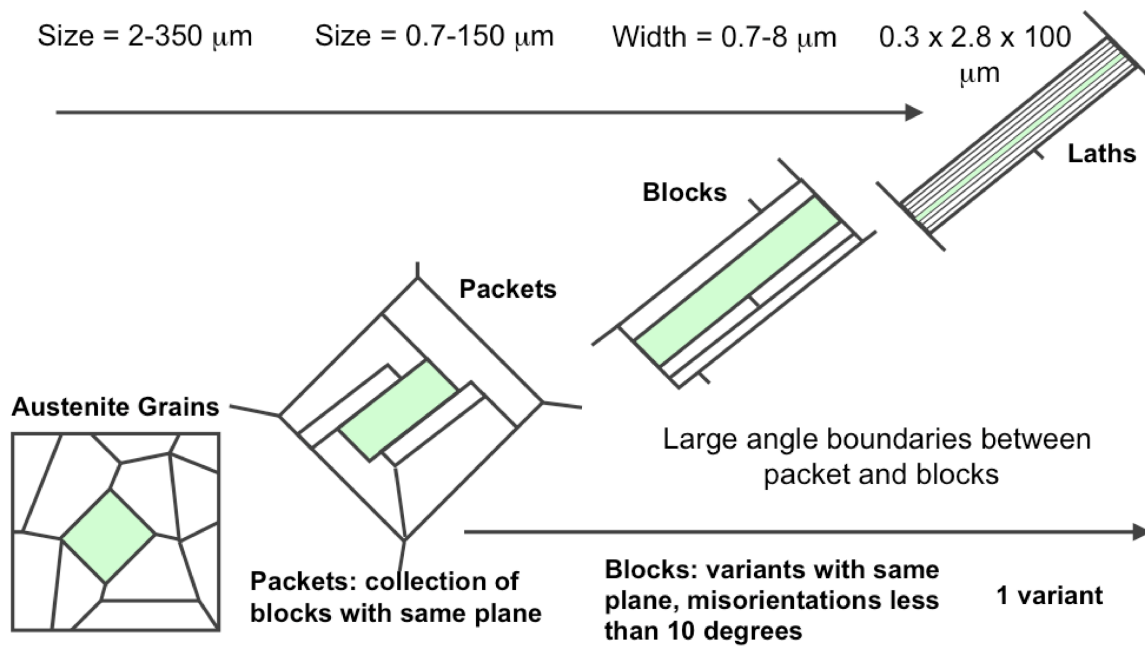


Figure 3.3 Lath martensite hierarchical microstructure, defined in four scale architecture, parent austenite grains, packets, blocks, and laths.

CHAPTER 4

NUMERICAL METHOD

To update the stress state of the crystalline material, both the total deformation rate tensor, D_{ij} , and the plastic deformation rate tensor, D_{ij}^p , are needed. A brief outline of the numerical method will be presented; for further details see Zikry [1]. An implicit finite element method analysis has been used to obtain the total deformation rate tensor, D_{ij} . The displacements have been obtained by the quasi-Newton solution of the static-equilibrium equation, with BFGS iteration to ensure convergence of the quasi-Newton method. Once the displacements are obtained, the deformation tensor can be calculated. To overcome numerical problems associated with incompressible displacements, the \bar{B} method has been used in the calculation of the deformation tensor. In the \bar{B} method, the deformation gradient is decomposed into volumetric and deviatoric parts. The volumetric part of the deformation tensor is then computed at reduced quadrature points. The resulting volumetric deformation field eliminates spurious modes that can arise due to incompressible deformations.

Once the deformation tensor is obtained from the updated nodal displacement values, the total deformation rate tensor, D_{ij} , and the total spin tensor, W_{ij} , can be calculated at each load level.

To solve for the plastic deformation rate tensor, D_{ij}^p , the time derivative of the resolved shear stress

$$\dot{\tau}^{(\alpha)} = \frac{d}{dt} (P_{ij}^{(\alpha)} \sigma_{ij}), \quad (4.1)$$

is used together with the objective stress rate, and the assumption that the elastic modulus tensor is isotropic, to obtain the following system of nonlinear differential equations for each active slip system α :

$$\dot{\tau}^{(\alpha)} = L_{ijkl} P_{ij}^{(\alpha)} D_{kl}^*, \quad (4.2)$$

in expanding form

$$\dot{\boldsymbol{\tau}}^{(\alpha)} = 2\mu P_{ij}^{(\alpha)} \left[D_{ij} - \sum_{\xi=1}^{12} P_{ij}^{(\xi)} \dot{\gamma}_{ref}^{(\xi)} \left(\frac{\boldsymbol{\tau}^{(\xi)}}{\boldsymbol{\tau}_{ref}^{(\xi)}} \right)^{\frac{1}{m}} \right]. \quad (4.3)$$

It has also been assumed, in the derivation of equation (*), that the lattice spin is a function of the elastic spin in all three directions

$$\dot{s}_i^{(\alpha)} = W_{ij}^* s_j^{(\alpha)}, \quad (4.4a)$$

$$\dot{n}_i^{(\alpha)} = W_{ij}^* n_j^{(\alpha)}, \quad (4.4b)$$

where the elastic lattice spin is obtained as

$$W_{ij}^* = W_{ij} - W_{ij}^P. \quad (4.5)$$

The solution to the system of ordinary differential equation (4.3), is numerically difficult, not only due to the nonlinearity of the resolved shear stress, but

also because the system of equation is numerically stiff in certain time intervals. The different time scales pertaining to the resolved shear stress on each slip system cause the numerical stiffness. These results in eigenvalues correspond to the Jacobian of the initial value problem that are widely varying. This leads to the growth of numerically propagated error, i.e., instability in the solution of the system of differential equations. The computational scheme developed by Zikry [1] is used to solve the system of equations (4.3). This algorithm is also used to update the evolutionary equations for the immobile and mobile dislocation densities.

Since the system of equations given by equation (4.3) is only stiff in some regions of the integration domain, an explicit fifth-order accurate Runge-Kutta method is used over most of the time domain. The propagated error is measured by the growth in the local truncation error. If the time-step must be restricted due to stability and not accuracy, a backward Euler method is used. The backward Euler method is both A-stable and stiffly stable; it is also an order one Backward Differentiation Formula (BDF). The algorithm methodology is as follows:

Automatic step control has been achieved by using step doubling on the

Runge-Kutta fourth-order method. Two approximate solutions are taken, one solution of step size $2h$ and a second solution with two steps, each of size h . Since the original method is fourth-order, the two numerical methods are related by

$$\tau(t+2h) = \hat{\tau}_1 + (2h)^5 \phi + O(h^6) + \dots, \quad (4.6)$$

$$\tau(t+2h) = \hat{\tau}_2 + 2(h)^5 \phi + O(h^6) + \dots, \quad (4.7)$$

where ϕ is of the order $\tau^5(t)/5!$. Furthermore, the two numerical methods are combined to give a solution of fifth-order accuracy

$$\tau(t+2h) = \hat{\tau}_2 + \frac{\Delta}{15} + O(h^6) + \dots, \quad (4.8)$$

where Δ is the local truncation error which measures how well the solution is approximated at each time step. Based on this error measurement, an adjusted time step is calculated

$$h_{new} = F h_{old} \left| \frac{\Delta_0}{\Delta_1} \right|^{0.20}, \quad (4.9)$$

where h_{new} is the adjusted time step, and h_{old} is the initial time step. The actual accuracy, Δ_1 , is measured by the supremum norm as $\max |\tau_1 - \tau_2|$, and Δ_0 is the desired accuracy measured by εH . Here ε is the tolerance level supplied by the user and H is a scaling factor for fractional errors for the i^{th} equation given by $|\tau| + \left| h \frac{d\tau}{dt} \right|$, where h is the initial time step. The factor F serves to keep the new time step small enough to be accepted if the truncation error in the next time step is growing. Based on equation (4.9), the time step is increased if the truncation error is smaller than the desired accuracy, and conversely the time step is decreased if the truncation error is greater than the desired accuracy.

Since Runge-Kutta methods have finite stability regions, there can be a growth in the propagated error and, therefore, the time step in certain time domains, can be restricted due to stability and not accuracy requirement by εH . This is an

indication of stiff behavior. In the present algorithm, the largest allowable time step is chosen, i.e., the time step on the stability boundary. This implies that the local errors are of the same magnitude as the accuracy tolerance used in equation (4.9). If the time step is unduly restricted due to stability, the solution will proceed in time, albeit inefficiently, due to the necessity of using intolerably small time steps. To correctly identify the regions of numerical stiffness, and to distinguish a step reduction due to accuracy from a time step reduction due to stability, a stiffness ratio, S_R , has been defined as

$$S_R = \frac{|\operatorname{Re} \lambda|_{\max}}{|\operatorname{Re} \lambda|_{\min}} \left(\frac{1}{t_2 - t_1} \right), \quad (4.10)$$

where $|\operatorname{Re} \lambda|_{\max}$ and $|\operatorname{Re} \lambda|_{\min}$ are the greatest and smallest absolute values of the real parts of the eigenvalues of the Jacobian of the system of ordinary differential equations given by equation (4.3), and $t_2 - t_1$ is the time interval of the integration. A large stiffness ratio, S_R , indicates that the ratios of the eigenvalues are dispersed relative to the time scale.

When the time step is restricted due to the presence of these widely varying eigenvalues, this is a stability problem, and an indication that the initial value problem is numerically stiff. An increasing stiffness ratio is an indication that for a specified deformation mode, the slip rate, $\dot{\gamma}^{(\alpha)}$, are much greater for one slip system than for the other active slip system; namely, one of the slip systems may be dominating the deformation process. The domination of one slip system over other active slip systems can occur, for example, when a macroscopic shear band is forming in a crystalline solid (see, for example, Zikry [1]).

If the stiffness ratio is increasing, then this is an indication of numerical stiffness, since the time step is being reduced due to stability considerations. In the present analysis, when stiff behavior is encountered, the integration is automatically switched to the backward Euler scheme. The quasi-Newton method has been used to solve the system of nonlinear algebraic equations.

The previous detailed algorithm, used to update the plastic deformation rate tensor, has also been used to update the coupled nonlinear mobile and immobile dislocation density evolutionary equations (2.29-2.30).

4.1 L_∞ Voronoi Tessellation Algorithm

To physically represent realistic grain shapes, an L_∞ Voronoi tessellation is used. Voronoi tessellations are widely used techniques to generate random grain shapes, as it generates equally distanced boundaries between a random set of points, which can be thought as nucleation sites, see for example [2]. Although, ordinary Voronoi tessellations can be used to generate equilibrium-transformed structures, it may not be appropriate for martensitic steels, since it cannot be used to account for habit plane orientations pertaining to the appropriate martensitic transformation. In this study, L_∞ Voronoi algorithms (Hwang [3] and Lee [4]) are used for the representation of martensitic microstructures. The algorithm is based on determining the distances from L_∞ bases, which can be used to orient the blocks along the specified habit planes. The technique can be used to generate orientations around general planes, such as (100) and irrational planes such as (557) by applying needed transformations. Furthermore, smoothing techniques were used to avoid sharp corners along grain and packet interfaces, as illustrated in Figure 4.1.

REFERENCES

- [1] Zikry M. A., and Kao M., 1996, "Inelastic Microstructural Failure Mechanisms in Crystalline Materials with High Angle Grain Boundaries," *J. Mech. Phys. Solids*, 44(11), pp. 1765-1798.
- [2] Torquato S., *Random heterogeneous materials: Microstructure and Macroscopic Properties*, Springer, New York, 2002.
- [3] Hwang F. K., 1979, "An $O(n \log n)$ Algorithm for Rectilinear Minimal Spanning Trees," *J. Assoc. Comput. Mach.*, 26(2), pp. 177-182.
- [4] Lee D. T., 1980, "Two Dimensional Voronoi Diagram in the L_p -Metric," *J. Assoc. for Comput. Mach.*, 27(4), pp. 604-618.

Figure for Chapter 4

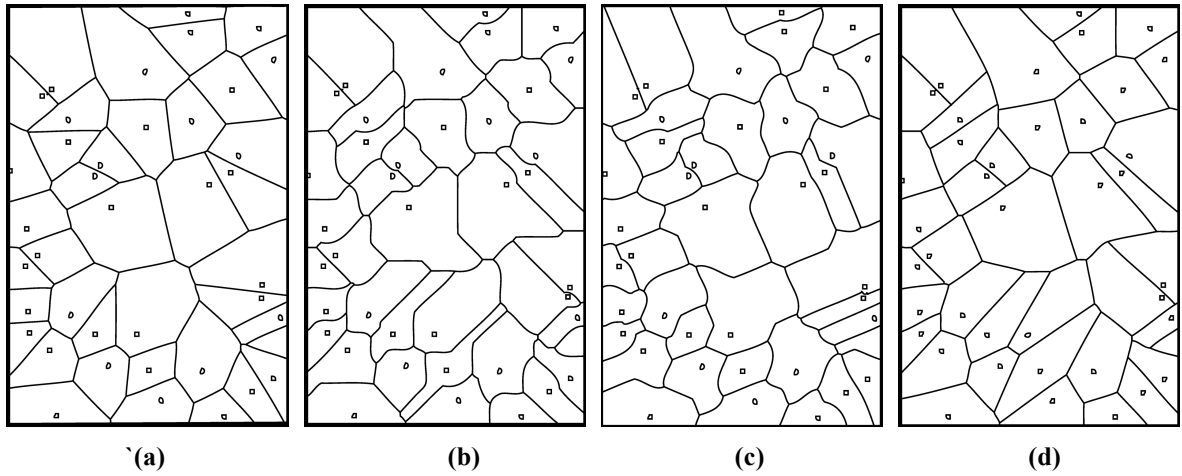


Figure 4.1 Proposed L_∞ Voronoi tessellations (a) ordinary Voronoi tessellations. (b) L_∞ Voronoi tessellations to the same set of points. (c) Applying the same algorithm with tilt angle of 30° . (d) modified L_∞ Voronoi tessellation algorithms (sharp corners avoided).

CHAPTER 5

A NEW PREDICTIVE MODEL FOR INITIAL DISLOCATION-DENSITIES FOR MARTENSITIC TRANSFORMATION

One of the challenges to model lath martensite is to obtain the initial dislocation densities associated with the martensitic transformation, since it can affect the behavior of martensitic structures, see, for example, Krauss [1,2]. Wayman [3] classified dislocations in martensitic microstructure as being of two basic types, transformation and interface dislocations. The transformation dislocations are screw dislocation in all four $\langle 111 \rangle_{\alpha'}$ direction, with $a/2 [\bar{1}\bar{1}1]_{\alpha'}$ as the dominant direction [3]. Morito *et al.* [4] have conducted experimental studies to obtain dislocation-densities in steels alloys with varying composition. However, these investigations do not provide how the initial dislocation-densities are associated with specific slip-systems, and how these dislocation-densities are apportioned between mobile and immobile components.

In this chapter, we used a dislocation-density crystalline plasticity formulation and specialized finite-element techniques to predict the initial mobile and immobile dislocation-

densities associated with martensitic transformations. The approach is based upon modeling the shear part of a martensitic transformation by a multiple slip dislocation-density based crystal plasticity approach. We validate the results with the $\{111\}$ transformation of low-nickel lath martensitic steels, Fe-10Ni [4].

5.1 Phenomenological Transformation Models

Several phenomenological theories have been introduced to interpret the transformation in lath martensite, [5-6]. Each of these approaches accounts for habit plane, product/parent orientation relationship, shape strain, and transformation and interface dislocations. In this study, we utilize the transformation theory introduced by Bowles and Mackenzie [7] and used by Crocker and Bilby [8] to interpret the martensitic transformation in lath martensitic steel with $\{111\}$ habit plane.

This approach is based on having a glissile interface between parent and product phases. This can exist if one direction and one plane (habit plane) is unrotated and undistorted. Hence, this martensitic transformation (P_1) is an Invariant Plane Strain (IPS), and can be described by three successive transformations, not necessarily ordered: (i) Bain

strain (B) transforms f.c.c. structure to b.c.c. structure with a minimum movement of atoms, and has one plane undistorted, although rotated; (ii) Rotation (R) which rotates the undistorted plane to its original position; (iii) Simple Shear (P_2) which restores the shape to fit the surrounding parent phase without distorting the previous plane.

Both (P_1), and (P_2) are IPS, where each one of them can be represented as $P = I - d' \times p$, where p is normal to the invariant plain, and d is the deformation vector. The product of both IPSs should be an Invariant Line Strain (ILS), and is given by

$$\begin{aligned}
 P_1 \times P_2 &= S = R \times B \\
 &= (I - d_1' \times p_1) \times (I - d_2' \times p_2)
 \end{aligned} \tag{5.1}$$

Based on calculations by Wayman [5], and Bhadeshia [6] for (S , P_1 , P_2) for Kurdjumov-Sachs (K-S) 24 variants, we obtained the following values for the deformation tensors and the normals to the invariant plane for the parent and transformed structures as

$$\begin{aligned}
 d_{2\ f.c.c.} &= [0.181 \quad 0 \quad -0.181 \quad] \\
 p_{2\ f.c.c.} &= [1 \quad 0 \quad 1 \quad] \\
 d_{2\ b.c.c.} &= [0.128 \quad 0.1283 \quad -0.181 \quad] \\
 p_{2\ b.c.c.} &= [0.707 \quad 0.7071 \quad 1 \quad]
 \end{aligned} \tag{5.2}$$

To obtain these values in the b.c.c. orientation, we used the transformation ${}_{\alpha}C_{\gamma}$,

$${}_{\alpha}C_{\gamma} = \begin{bmatrix} 1 & -1 & 0 \\ 1 & 1 & 0 \\ 0 & 0 & 1 \end{bmatrix}, \quad (5.3)$$

where α is the f.c.c. parent orientation and γ is the transformed b.c.c. structure.

5.2 Results for Transformation in f.c.c. and b.c.c. Crystals

The multiple slip dislocation-density based crystal plasticity formulation, and the specialized finite element algorithm were used to investigate the martensitic transformation of steel alloys. The martensite orientation and transformation are represented as outlined in section 5.1. The values of (d_2) and (p_2) given by section 5.1 are used to model the transformation, see Figure (5.1). An orientation matrix, T, for the transformed matrix, was calculated as

$$[T] = [\bar{d}_2 \quad p_2 \quad \bar{d}_2 \times p_2]^{-1} \quad (5.4)$$

where \bar{d}_2 is the normalized value of d_2 .

The material properties (Table 5.1) that are used here are representative of low nickel alloy steel.

Using the method outlined by Kameda and Zikry [9], the initial coefficient values, needed for the evolution of the immobile and mobile densities, for eqns. (3.6-3.7), were obtained as

$$\begin{aligned} g_{\text{minter}} = 5.53, \quad g_{\text{recov}} = 6.67, \quad g_{\text{immob}} = 0.0127, \quad g_{\text{sour}} = 2.7 \times 10^{-5}, \quad \text{and} \\ H/K = 3.289 \times 10^3 \text{ } ^\circ\text{K}. \end{aligned} \quad (5.5)$$

As outlined in Figure 5.1, we separately modeled a simple shear problem for an invariant plane for an f.c.c. and a b.c.c. single crystal. For the f.c.c. model, we obtained a shear slip of 0.24, a lattice rotation of -8.08° , a shear stress of 750 MPa, and a normal stress

value of 300 MPa at an imposed shear value of . The Shear slip and lattice rotation values match the assumed values in phenomenological theory, [5-6].

For the f.c.c. model, four active slip-systems are active: $(111) / [\bar{1}01]$, $(\bar{1}\bar{1}1) / [101]$, $(\bar{1}11) / [101]$, and $(1\bar{1}1) / [\bar{1}01]$. All have the same mobile dislocation-density of $0.14 \times 10^{14} \text{ m}^{-2}$, and immobile dislocation-density of $0.64 \times 10^{14} \text{ m}^{-2}$. This is consistent with values obtained by Morito *et al.* [4]. The sum of the dislocation-densities are close to the values extrapolated from Morito *et al.* [4] of $3.1 \times 10^{14} \text{ m}^{-2}$. However, equal values of dislocation-densities on different slip-systems are not observed experimentally, and a dominant slip-system is usually observed [3-4].

Hence, we modeled the same problem for a b.c.c. structure. For the b.c.c. model, even though we initially assumed that all 24 slip-systems are potentially active, after deformation for the shear problem with the ISP conditions, only one slip system $(112) / [11\bar{1}]$ is active with a mobile dislocation-density of $0.46 \times 10^{14} \text{ m}^{-2}$ and an immobile dislocation-density of $2.57 \times 10^{14} \text{ m}^{-2}$ at a shear value of . This active slip-system is parallel to the long direction of laths in all variants. The sum of the immobile and mobile dislocation-

densities on b.c.c. crystal is almost the same as that experimentally obtained proposed by Morito *et al.* [4].

Hence, the transformation dislocation densities can be interpreted as a combination of both f.c.c. and b.c.c. crystals. The ratio of the contribution of each slip system can be correlated with experimental observations. However, for simplicity, we can use the b.c.c. active slip-system dislocation-density values as initial immobile and mobile dislocation-density values for modeling lath martensite in steels. This is also consistent with the that the dominance of one slip system [3-4].

5.3 Summary

A multiple-slip dislocation density based crystal plasticity model and specialized finite-element techniques were used to predict initial immobile and mobile dislocation densities for an ISP shear deformation related to martensitic deformations. The predicted values for the f.c.c. and b.c.c. structures are almost approximately the same as those obtained by Morito *et al.* [4]. However, only one slip-system is dominant for the b.c.c. system, which is consistent with the experimental observations of Maki. Hence, the initial mobile and

immobile dislocation-densities from the b.c.c. structure can be used for investigations related to the failure behavior of martensitic steels. These initial values, which are based on slip-system activity and orientations, can be an important step in accurately modeling martensitic structures on the microstructural scale.

REFERENCES

- [1] Krauss G., 2001, "Deformation and Fracture in Martensitic Carbon Steels Tempered at Low Temperature," *Metall. Mater. Trans. A*, 32B, pp. 205-221.
- [2] Saeglitz M., and Krauss G., 1997, "Deformation, Fracture, and Mechanical Properties of Low-Temperature-Tempered Martensite in SAE 43xx Steels," *Metall. Mater. Trans.*, A 28A, pp. 377-387.
- [3] Sandvik B. P. J. and Wayman C. M., 1983, "Characteristics of Lath Martensite, I, II, III," *Metall. Trans. A*, 14A, pp. 809-822, 823-834, 835-844.
- [4] Morito S., Nishikawa J., *et al.*, 2003, "Dislocation Density within Lath Martensite in Fe-C and Fe-Ni Alloys," *ISIJ Int.*, 43(9), pp. 1475-1477.
- [5] Otsuka K. and Wayman C. M., 1999, *Shape Memory Alloys*, Cambridge University Press, UK.
- [6] Bhadeshia H. K. D. H., 2001, *Worked Examples in the Geometry of Crystals*. The institute of metals, London.
- [7] Bowles J. S., and Mackenzie J. K., 1954, "The crystallography of martensite transformation. III. Face centered tetragonal transformations," *Acta Metall*, 2, pp. 224-234.

[8] Crocker A. G., and Bilby B. A., 1961, "The crystallography of the martensitic reaction in steel," *Acta Metall*, 9, pp. 678-688.

[9] Kameda T., and Zikry M. A., 1996, "Three Dimensional Dislocation-Based Crystalline Constitutive Formulation for ordered Intermetallics," *Scripta Mater.*, 38(4), pp. 631-636.

**Table and Figure for
Chapter 5**

Table 5.1 Properties of martensite and austenite steels.

Properties	Martensite phase	Austenite phase
Young's modulus, E	228 GPa	200 GPa
Static yield stress, σ_y	517 MPa	367 MPa
Poisson's ratio, ν	0.3	0.3
Rate sensitivity parameters, m	.01	.01
Reference strain rate, $\dot{\gamma}_{ref}$.001s ⁻¹	.001s ⁻¹
Critical strain rate, $\dot{\gamma}_{critical}$	10 ⁴ s ⁻¹	10 ⁴ s ⁻¹
Burger vector, b	3.0×10^{-10} m	3.0×10^{-10} m
Initial immobile dislocation density, $\rho_{im}^{(\alpha)}$	10 ¹⁰ m ⁻²	10 ¹⁰ m ⁻²
Initial mobile dislocation density, $\rho_m^{(\alpha)}$	10 ⁷ m ⁻²	10 ⁷ m ⁻²

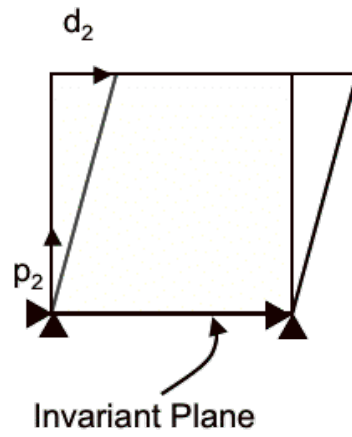


Figure 5.1 The boundary conditions and loading for a simple shear problem. P_2 is parallel to y-axis and d_2 is parallel to x-axis.

CHAPTER 6

MODELLING OF LATH MARTENSITIC MICROSTRUCTURES

The three-dimensional multiple-slip dislocation-density-based crystalline formulation, specialized finite-element formulations, and L_∞ Voronoi tessellations adapted to martensitic orientations, presented in previous chapters, were used to investigate large strain inelastic deformation modes and dislocation-density evolution in martensitic microstructures. The formulation is based on accounting for variant morphologies and orientations, retained austenite, and initial dislocations-densities that are uniquely inherent to martensitic microstructures. In this chapter, the computational framework and the constitutive formulation used in the current study were validated with experimental results on 10% Ni steel alloy under quasi-static axial compression loading. The effects of parent austenite orientation and retained austenite were also investigated for heterogeneous f.c.c./b.c.c. crystalline structures. Furthermore, the formulation was used to investigate microstructures mapped directly from SEM/EBSD images of martensitic steel alloys.

6.1 Model Validation

The multiple-slip dislocation-density based crystal plasticity formulation, the specialized finite element algorithm, and the L_∞ Voronoi scheme were used to investigate the large strain inelastic behavior of martensitic steel. The martensite orientation is represented as outlined in Chapter 3. The parent austenite grain is oriented based on the loading plane of $(001)_\gamma$, and two loading directions $[010]_\gamma$ and $[110]_\gamma$. The K-S relation is adapted as the martensite OR, and $\{111\}_\gamma$ is assumed as the habit plane. The martensite morphology is generated by the L_∞ Voronoi tessellation to generate block and packet microstructures relative to the parent austenite grain. A representative aggregate size was determined by modeling the response of aggregates with different aggregate sizes. In this study, 40 martensitic grains are used with 10 packets, with an average of 4 blocks per packet as shown in Figure 6.1. It is also assumed that the parent austenite grain has an initial cube orientation.

Using the method outlined by Kameda and Zikry [1], the initial coefficient values, needed for the evolution of the immobile and mobile dislocation-densities given by equations (2.29-2.30) were obtained as

$$g_{\text{minter}} = 5.53, \quad g_{\text{recov}} = 6.67, \quad g_{\text{immob}} = 0.0127, \quad g_{\text{sour}} = 2.7 \times 10^{-5}, \quad \text{and}$$

$$H/K = 3.289 \times 10^3 \text{ } ^\circ\text{K}. \quad (6.1)$$

A mobile and immobile dislocation-densities saturation values were obtained for the previous values, and found to be:

$$\rho_{im,s}^{(\alpha)} = 1.16 \times 10^{16} \text{ m}^{-2}, \quad \rho_{m,s}^{(\alpha)} = 6.86 \times 10^{14} \text{ m}^{-2}, \quad (6.2)$$

To validate the modeling scheme, comparisons were made with experiments conducted by Kumar [2] on 10% Ni steel alloy. Comparisons were made for axial compression strain rates of 0.01/s, and 0.0001/s by applying normal axial loads as shown in Figure 6.1. Based on a convergence analysis, 2485 four node quadrilateral elements were used with a plane strain analysis for a specimen size of 4.2 mm by 6.3 mm. The material properties (Table 6.1) that are used here are representative of low nickel alloy steel.

The global nominal stress-strain curve of a comparison between the predictions and the experimental results is shown in Figure 6.2. As seen, there is excellent agreement between the predicted and measured values for both strain-rates for nominal strains up to 30%. These results validate the computational framework and constitutive formulation that has been developed.

As noted earlier, the representation of the morphological martensitic microstructures by tessellation is critical. If ordinary tessellation had been used instead of the adapted L_∞ Voronoi scheme, the results would have been different and inaccurate. Figure 6.3 compares the results of L_∞ Voronoi and the ordinary Voronoi tessellations with the experimental measurements. Both models have the same set of points and material properties, and the only difference is in the tessellation algorithm. It is clearly obvious that the ordinary Voronoi scheme differs significantly from the experimental results, and that the L_∞ Voronoi has excellent comparison with the experimental measurements. This is due to the incorporation of accurate representations of habit planes, slip-system orientations, and lath long direction within the L_∞ Voronoi scheme. As these microstructural characteristics, as will be seen, have an important effect on deformation and localization.

To further elucidate the local microstructural mechanisms, the contours for the mobile dislocation-densities (Figure 6.4), and the immobile dislocation-densities (Figure 6.5) corresponding to the three most active slip-systems, at a nominal strain of 15% are shown. The maximum normalized (the mobile densities are normalized by the saturated mobile dislocation-density) mobile dislocation-densities are 0.44 for $(\bar{1}12)/[1\bar{1}1]$, 0.22 for $(112)/[11\bar{1}]$, and 0.08 for $(1\bar{1}2)/[\bar{1}11]$. The maximum normalized (the immobile densities are normalized by the saturated immobile dislocation-density) immobile dislocation-densities for the three slip-systems are 0.55 for $(\bar{1}12)/[1\bar{1}1]$, 0.33 for $(112)/[11\bar{1}]$, and 0.17 for $(1\bar{1}2)/[\bar{1}11]$. The evolution of dislocation-densities along selected blocks and along low-angle grain boundaries (as noted earlier grain boundaries are equivalent to block boundaries) result in an increase in dislocation-densities values and a localization of shear slip as shown in Figure 6.6. These increases in dislocation-density are due to an alignment of the load towards $[010]_y$. $[011]_y$ is a maximum resolved shear stress direction for this load, since it is 45° from the loading direction. $[011]_y$ is also parallel to the long direction of laths and blocks, and parallel to the slip direction $[111]_\alpha$ based on the K-S OR.

To further underscore the orientation relation between loading direction, slip-systems, and the lath long directions, the stereographic projection of the slip-systems of variant #11 relative to the loading direction, the locus of maximum resolved shear stress (a circle that is 45° from the loading direction), and the long direction of the variant are plotted as in Figure 6.7. As can be seen, the slip direction $[11\bar{1}]_{\alpha'}$ aligns with $[0\bar{1}\bar{1}]_{\gamma}$, which is the long direction of the laths inside the block and the maximum resolved shear direction for the uniaxial loading direction of $[010]_{\gamma}$. Furthermore, slip-plane $(112)_{\alpha'}$ is almost coincident with the maximum resolved shear locus. This would activate slip-system $(112) / [11\bar{1}]$ in this variant as was confirmed by the results shown in Figures 6.4b, and 6.5b.

Similarly for variant #4, the slip direction $[1\bar{1}\bar{1}]_{\alpha'}$ aligns with the direction $[0\bar{1}\bar{1}]_{\gamma}$. Slip-plane $(\bar{1}12)$ is nearly adjacent to the maximum resolved shear stress direction. This activates slip-system $(\bar{1}12) / [1\bar{1}\bar{1}]$ as confirmed by Figures 6.4a and 6.5a. Similar behavior can be obtained for other variants. Furthermore, systems $(\bar{1}12) / [1\bar{1}\bar{1}]$ in variant #4 and $(112) / [11\bar{1}]$ in variant #11 are continuous, which lead to shear-strain localization as shown in Figure 6.6. This special configuration aligns the slip-systems with the maximum resolved shear stress direction with the long direction of the blocks, and when combined with the low

angle boundaries between blocks, acts as shear pipes for the localization of dislocation-densities and shear strains.

As shown in Figure 6.6a, the accumulated maximum plastic shear is 2.21 at a nominal strain of 15%. This large value is due to geometrical softening and the orientation effects associated with the shear pipes. The geometrical softening occurs due to the large lattice rotation that is high as 31.1° (Figure 6.8a), reaching its maximum at the kink on the free surface. The maximum normalized (stress values are normalized by the static yield stress) normal stress is -5.23 (Figure 6.8b), and the maximum normalized shear stress is 0.85 (Figure 6.8c). These maximum values occur at the blocks boundaries.

It should also be noted that the immobile dislocation-density associated with slip-system $(\bar{1}12) / [1\bar{1}1]$ saturates at a nominal strain of approximately 21%, which is the unloading strain of the experimental specimen. At this strain, several inactive slip-systems are activated due to lattice rotation, and at 30% nominal strain, 21 slip-systems are active through the specimen.

6.2 Parent Austenite Orientation

In this section, we investigate the effects of initial austenite orientation on large strain inelastic deformation in martensitic steels microstructures. For this analysis, we assumed, as before, one austenite grain would result in 40 blocks and 10 packets, and the microstructure is generated by the L_∞ Voronoi tessellation algorithm using the same set of points used in the previous analyses. The parent austenite grain is oriented based on a loading plane of $(001)_\gamma$, and a loading direction of $[110]_\gamma$, by applying a transformation angle of 45° . The Euler angles and the relations with the global axes were determined from the previously presented, $[T]_3 = [X]_\gamma^{-1} * [X]_G$ relation.

The contours for the mobile dislocation-densities (Figure 6.9), and the immobile dislocation-densities (Figure 6.10) corresponding to the two most active slip-systems, at a nominal strain of 15%, are shown. The maximum normalized mobile dislocation-densities for the two slip-systems are 0.11 for $(110) / [1\bar{1}1]$, and 0.08 for $(011) / [1\bar{1}1]$, while the maximum normalized immobile dislocation-densities are 0.22 for $(110) / [1\bar{1}1]$, and 0.18 for $(011) / [1\bar{1}1]$. Furthermore, both dislocation-densities and shear slip (Figure 6.11a) are uniformly distributed throughout the specimen with no evident of localization. This can be

due to the orientation effects of the austenite grain, since the blocks and the lath long directions are inclined, and not coincident, with the maximum resolved shear stress orientation (Figure 6.11a). The maximum shear slip is 0.64, which is three times less than the previous model, and the maximum lattice rotation is 30.73° (Figure 6.11b).

6.3 Retained Austenite

It has frequently been observed that there are small percentages of retained austenite between laths and blocks in lath martensite, see, for example, [3-4]. To investigate these effects, we modeled a heterogeneous crystalline structure with f.c.c. for the retained austenite structure and b.c.c. for the martensitic structure. We assumed that 10% of the volume is retained austenite. The retained austenite was assumed to be parallel to the long direction of the blocks in two configurations; inside the martensitic blocks (Model 1), and between blocks/packets (Model 2).

The shear slip and lattice rotation for both models are presented in Figure 6.12. The maximum shear slip is 1.66 for Model 1 and 1.85 for Model 2. The maximum lattice rotation is -30.71° for Model 1 and -34.79° for Model 2. In both cases, there is a considerable

decrease in the values of shear slip in comparison with cases with no retained austenite. This difference in behavior can be due to the interaction of martensitic (b.c.c.) slip-systems with the retained austenitic (f.c.c.) regions. Slip-systems in austenite (f.c.c.) are $\{111\}_{\gamma}/\langle 110 \rangle_{\gamma}$, which would be aligned with the $\{110\}_{\alpha}/\langle 111 \rangle_{\alpha}$ based on the KS OR between parent austenite and martensitic systems. However, active slip-systems in the martensitic (b.c.c.), blocks are of the $\{112\}$ family of planes, which would make it incompatible with f.c.c. slip-systems. This incompatibility between both slip-systems can impede and block dislocation-density transmission and shear-slip accumulation at f.c.c.-b.c.c. interfaces. On the other hand, if we had active slip-systems corresponding to the $\{110\}$ family of planes, the slip-systems would be compatible with the f.c.c. slip-systems of the retained austenite, and that can enhance plastic strain accumulation and localization.

These results are consistent with experimental observations pertaining to the stabilizing effects of retained austenite, see, for example, [3-5]. Moreover, the proposed approach can be an effective tool in predicting the mechanical behavior for a wide range of microstructures in steels such as dual phase steel and carbide free bainite steel.

6.4 Physically Representative Microstructure: SEM/EBSD Steel Microstructures

To further validate the proposed approach, the previous models were compared with experimentally SEM/EBSD characterized lath martensite in low carbon steel (0.2 wt.% C steel), see Kitahara *et al.* [6]. Figure 6.13, shows the model mapped directly from Kitahara *et al.* [41] by extrapolating the geometrical coordinates, and was then discretized into a finite-element mesh.

Figure 6.14 shows shear slip and lattice rotation at two nominal strains of 5% (a, b) and 15% (c, d). The maximum shear slip is 0.07 at a nominal strain of 5% and 1.92 at nominal strain, of 15% combined with maximum lattice rotation of -2.92° at 5% nominal strain and -37.31° at 15% nominal strain. Due to crystal rotations and geometrical softening inside the blocks, the shear slip is highly localized, as seen in Figure 6.14. These results indicate how physical microstructures can be used with the proposed framework to predict behavior at the relevant martensitic microstructural scale.

6.5. Summary

This investigation provides detailed validated predictive capabilities that have been used to understand complex interrelated physical mechanisms that relate to martensitic microstructures at different physical scales. A physically based microstructure representation of variants, blocks, packets, retained austenite, and initial dislocations was developed. A multiple-slip rate-dependent crystalline constitutive formulation that is coupled to the evolution of mobile and immobile dislocation-densities, and specialized computational schemes have been developed to investigate the effects of variant shapes, orientations, retained austenite, parent austenite grain orientations, and initial dislocation-densities associated with transformation strains.

For a loading direction of $[010]_y$, significant increases in dislocation activities occur along the blocks, and slip-systems $(1\bar{1}2) / [\bar{1}11]$, $(\bar{1}12) / [1\bar{1}1]$, and $(112) / [11\bar{1}]$ are the dominant systems. This configuration is almost coincident with the maximum resolved shear stress direction and with the long direction of blocks. When combined with low angle boundaries between blocks it acts as shear pipes that increase the dislocation-densities and shear strains within highly localized regions. This behavior was also evident for the mapped

SEM/EBSD images, where the loading was oriented on the same direction, which is a further indication of the validity of the proposed predictive methodology.

For the $[110]_{\gamma}$ loading directions, $(110)/[1\bar{1}1]$, and $(011)/[1\bar{1}1]$ are the most active slip-systems. The shear slip is three times less than the previous loading direction. This can be due to the incompatibility between slip directions, the long direction of laths and the maximum resolved shear stresses, where more grain boundaries are available to impede the dislocation transmission between blocks.

The effects of retained austenite on dislocation activities and behavior of martensitic steels was also investigated by incorporating f.c.c structures (retained austenite) within b.c.c structures (martensitic blocks) The results clearly show the stabilizing effect of retained austenite and crystalline heterogeneities in reducing plastic strains and lattice rotations in critical regions.

This general methodology underscores the importance of accurately representing martensitic microstructure on different microstructural scales. This predictive framework can be used to model other steel phases and alloys, such as bainite and dual phase steels and to potentially control behavior at the microstructural scale.

REFERENCES

- [1] Kameda T., and Zikry M. A., 1996, "Three Dimensional Dislocation-Based Crystalline Constitutive Formulation for ordered Intermetallics," *Scripta Mater.*, 38(4), pp. 631-636.
- [2] Kumar S., Brown University, private communication.
- [3] Thomas G., 1978, "Retained Austenite and Tempered Martensite Embrittlement," *Metall. Trans. A*, 9A, pp. 439-450.
- [4] McMahon J. A. and Thomas G., 1973, *Proceedings of the 3rd International Conference on the Strength of Metals and Alloys*, Institution of Metals, London, pp. 180-184.
- [5] Nakagawa H. and Miyazaki T., 1999, "Effect of Retained Austenite on the Microstructure and Mechanical Properties of Martensitic Precipitation Hardening in Stainless Steel," *J. Mater. Sci.*, 34, pp. 3901-3908.
- [6] Kitahara H., Ueji R., *et al.*, 2006, "Crystallographic Features of Lath Martensite in Low-Carbon Steel," *Acta Mater.*, 54, pp. 1279-1288.

**Table and Figures for
Chapter 6**

Table 6.1 Properties of martensitic and austenitic grains.

Properties	Martensite phase	Austenite phase
Young's modulus, E	228GPa	200 GPa
Static yield stress, τ_y	517MPa	367 MPa
Poisson's ratio, ν	0.3	0.3
Rate sensitivity parameters, m	0.01	0.01
Reference strain rate, $\dot{\gamma}_{ref}$	$0.001s^{-1}$	$0.001s^{-1}$
Critical strain rate, $\dot{\gamma}_{critical}$	$10^4 s^{-1}$	$10^4 s^{-1}$
Burger vector, b	$3.0 \times 10^{-10}m$	$3.0 \times 10^{-10}m$
Reference stress interaction coefficient, a_i ($i=1, n$)	0.5	0.5
Initial immobile dislocation-density, $\rho_{im}^{(\alpha)}$	Calculated	$10^{10} m^{-2}$
Initial mobile dislocation-density, $\rho_m^{(\alpha)}$	Calculated	$10^7 m^{-2}$

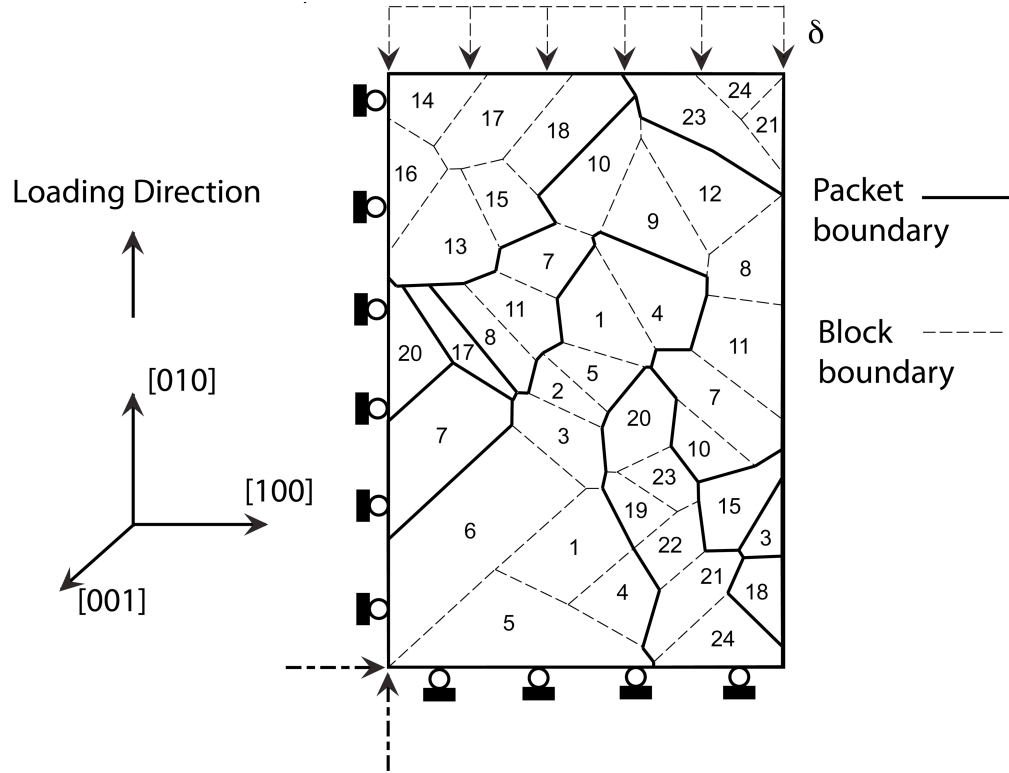


Figure 6.1 Microstructural model used in the current study, the distribution of variants in blocks and packets (variants numbered as indicated in Table 3.4), and loading, geometry, and boundary conditions.

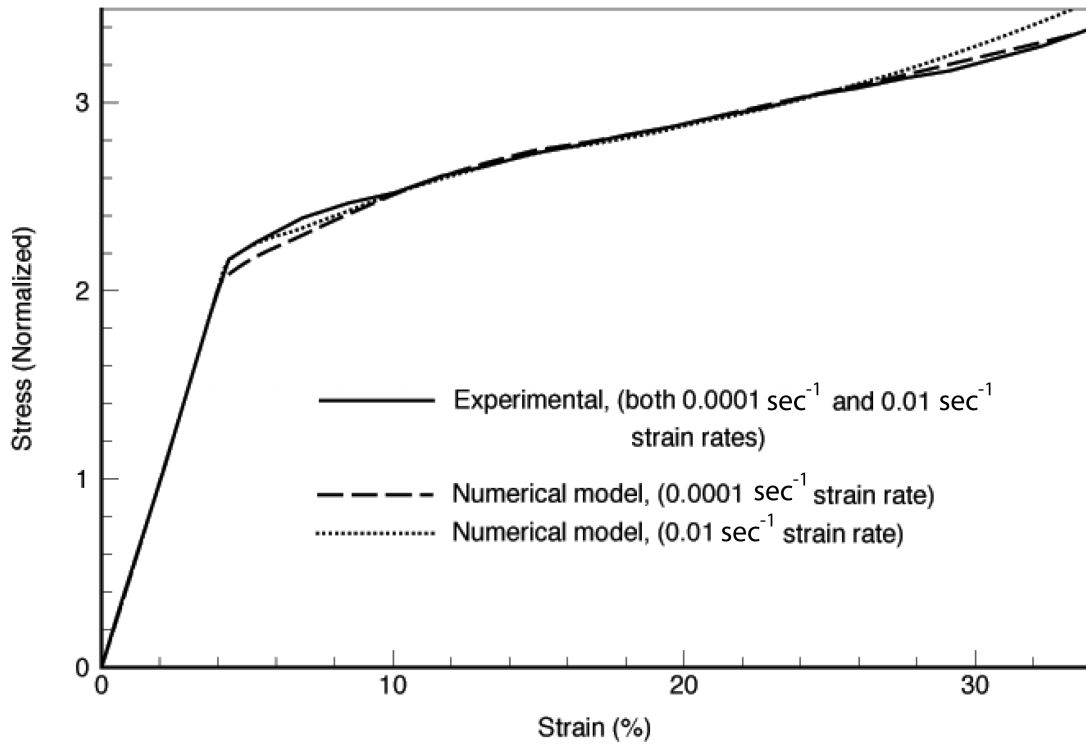


Figure 6.2 Global stress-strain curve for experimental and predicted results for low nickel martensitic steel (Stresses values are normalized by the static yield stress).

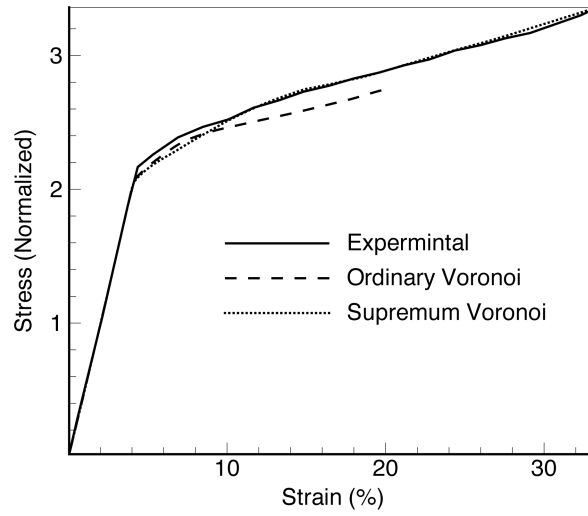


Figure 6.3 Global stress-strain curve for experimental results for low nickel martensitic steel, compared with numerical results obtained using ordinary Voronoi algorithms and proposed L_{∞} Voronoi algorithm.

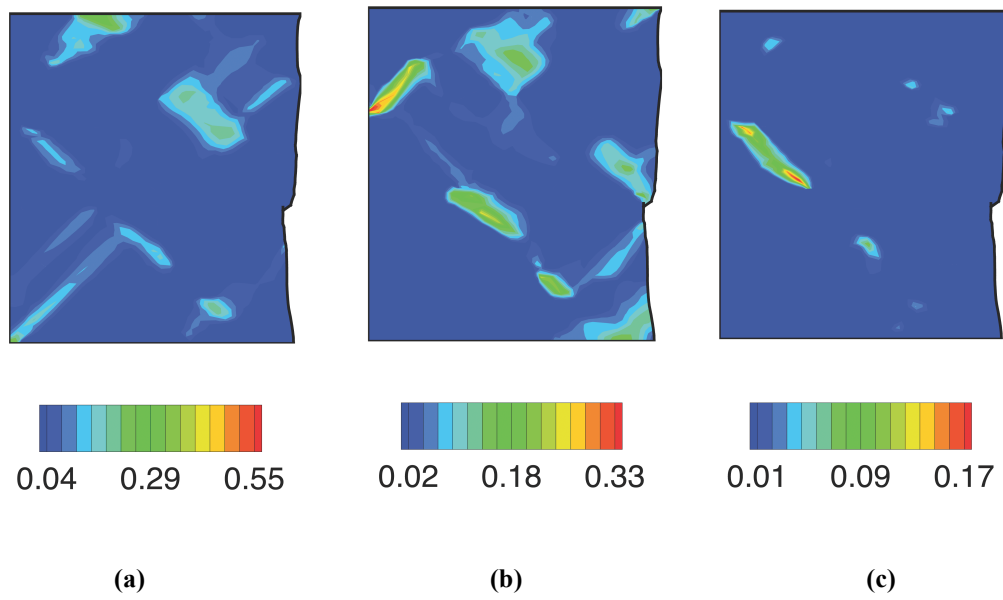


Figure 6.4 Normalized mobile dislocation-densities for most active slip-systems; (a) slip-system $(\bar{1}12)/[1\bar{1}1]$, (b) slip-system $(112)/[11\bar{1}]$, and (c) slip-system $(1\bar{1}2)/[\bar{1}11]$ at a nominal strain of 15%. Values normalized by mobile dislocation-densities saturation values, $\rho_{m,s}^{(\alpha)} = 6.86 \times 10^{14} \text{m}^{-2}$.

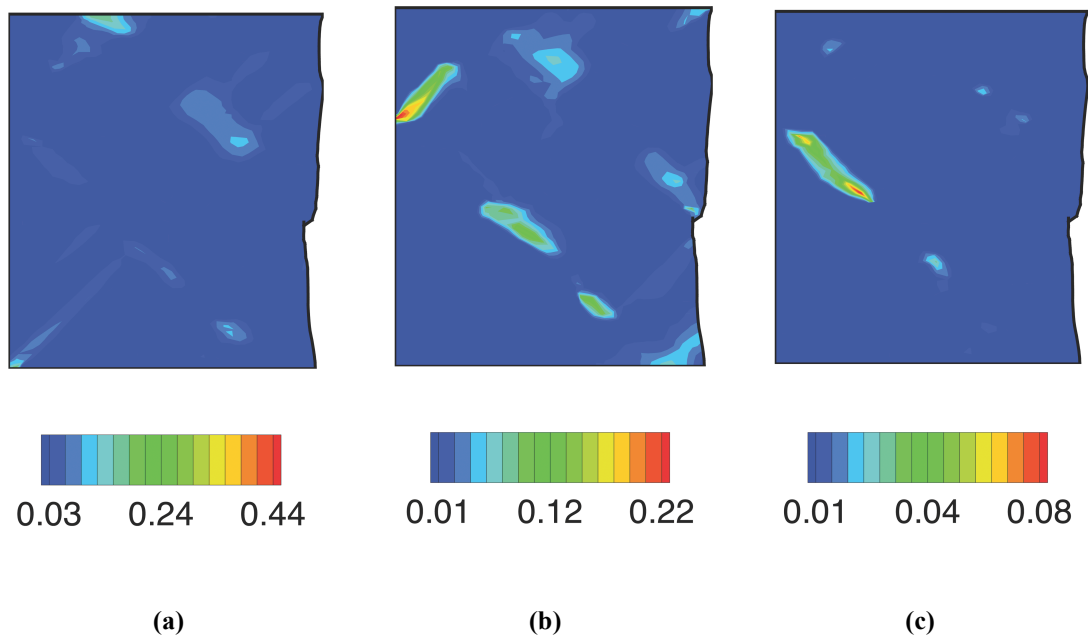


Figure 6.5 Normalized immobile dislocation-densities for most active slip-systems; (a) slip-system $(\bar{1}12)/[1\bar{1}1]$, (b) slip-system $(112)/[11\bar{1}]$, and (c) slip-system $(1\bar{1}2)/[\bar{1}11]$ at a nominal strain of 15%. Values normalized by immobile dislocation-densities saturation values, $\rho_{im,s}^{(\alpha)} = 1.16 \times 10^{16} \text{m}^{-2}$.

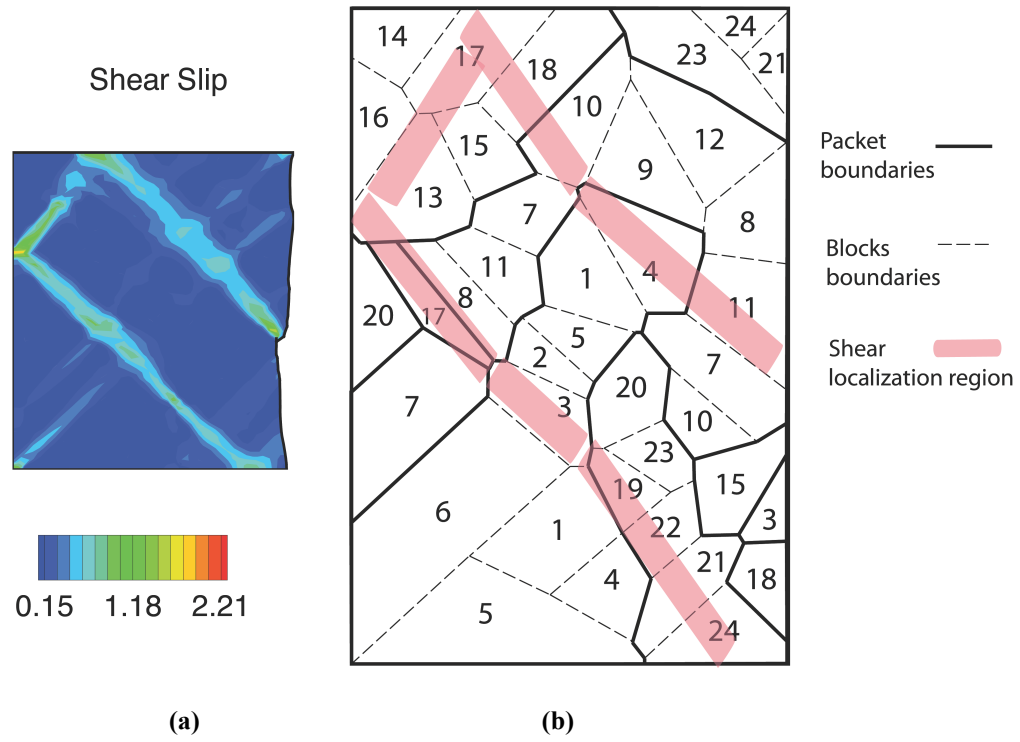


Figure 6.6 Results obtained for the modeled specimen, at a nominal strain of 15% (a) Shear slip contours γ ; (b) schematic of the specimen with shear localization region highlighted.

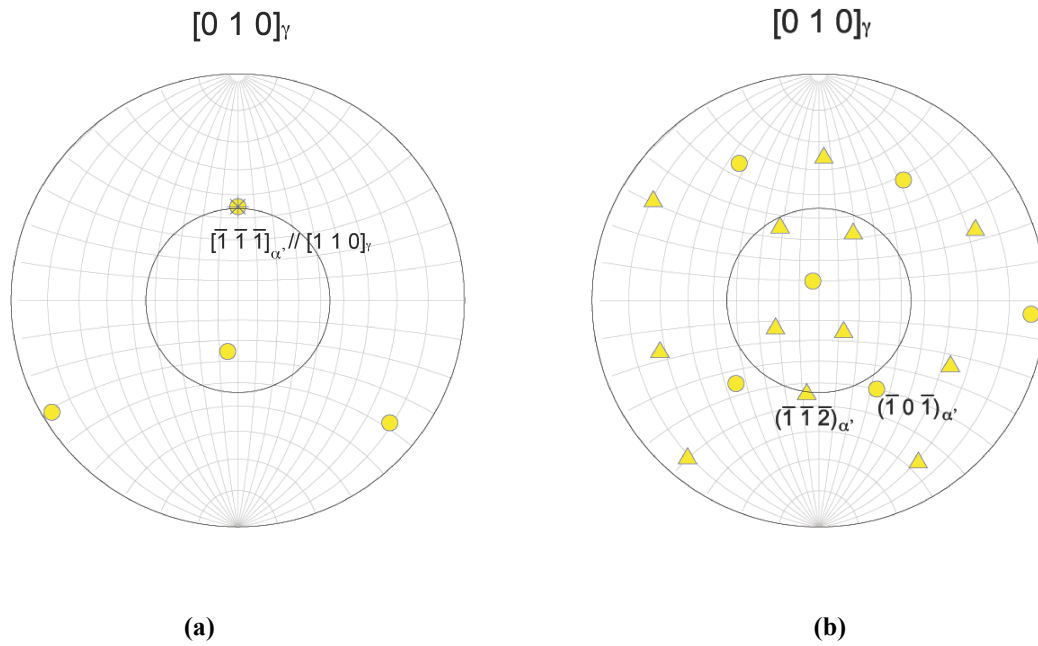


Figure 6.7 $[010]_\gamma$ stereographic projection for variant #11 slip-systems relative to the loading direction, the locus of maximum resolved shear stress (the inner circle) and the long direction of the variants (presented as * in figure a) (a) the slip directions, (b) the slip planes.

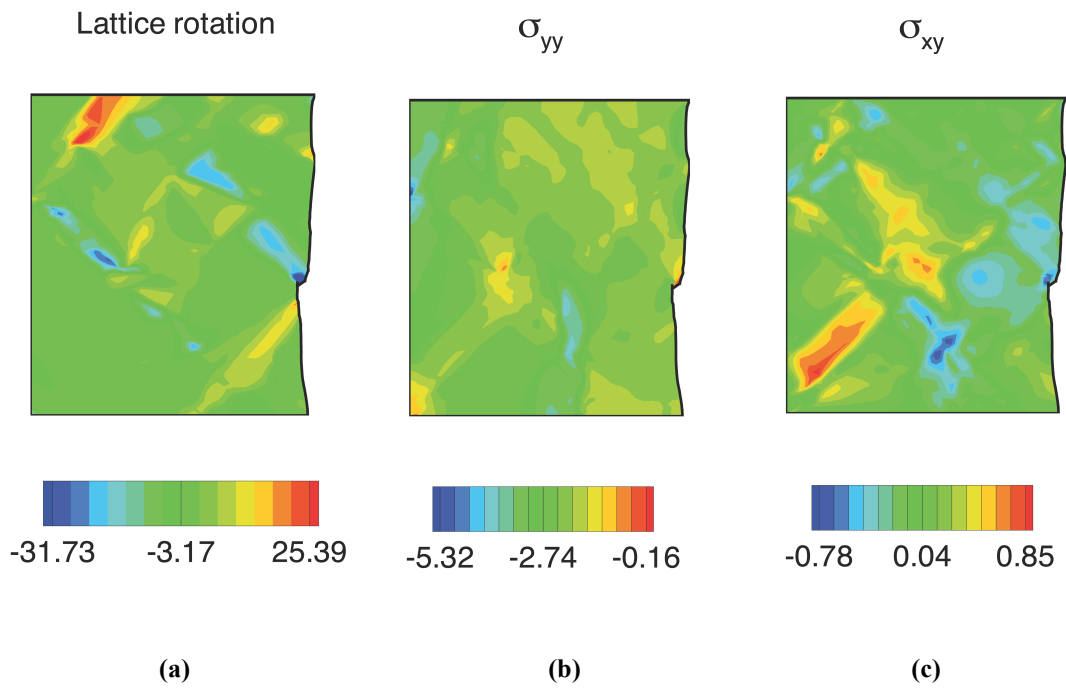


Figure 6.8 Results obtained for the modeled specimen, at a nominal strain of 15%; (a) lattice rotation in degrees; (b) normalized normal stresses; (c) normalized shear stresses. Stress values are normalized by the static yield stress.

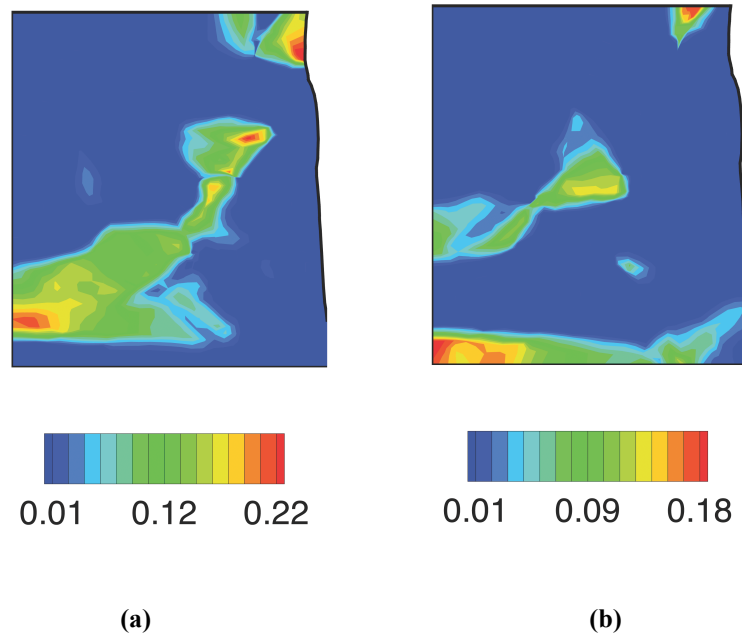


Figure 6.9 Normalized mobile dislocation-densities for most active slip-systems for $[011]_y$ loading direction; (a) slip-system $(011)/[11\bar{1}]$, (b) slip-system $(011)/[1\bar{1}1]$, at a nominal strain of 15%.

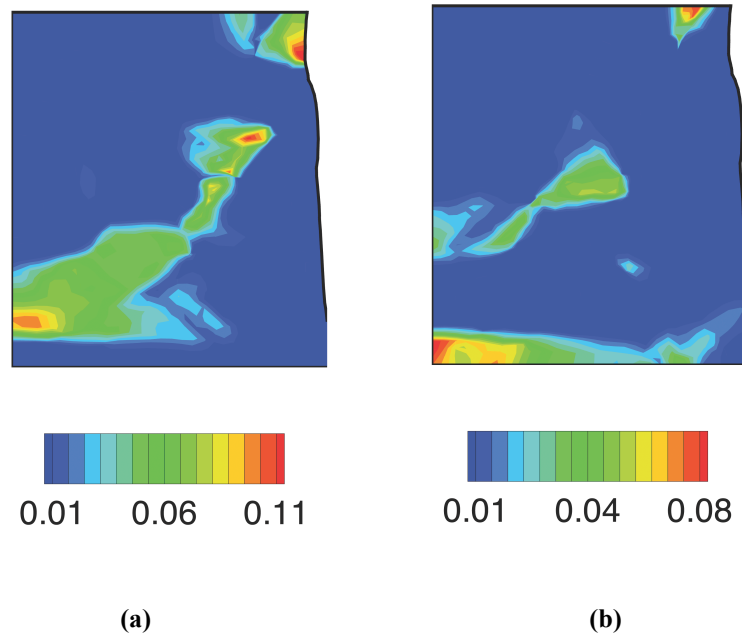


Figure 6.10 Normalized immobile dislocation-densities for most active slip-systems for $[011]_y$ loading direction, (a) slip-system $(011)/[11\bar{1}]$, (b) slip-system $(011)/[1\bar{1}1]$, at a nominal strain of 15%.

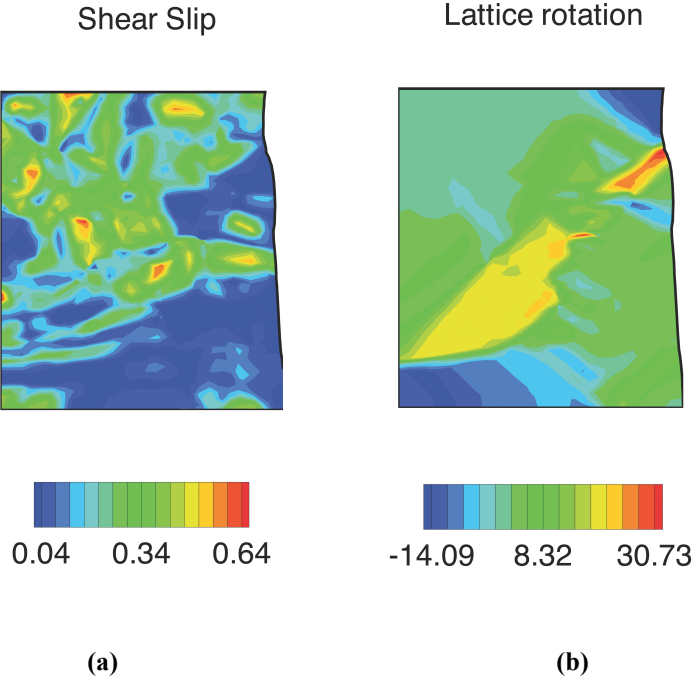


Figure 6.11 Results obtained for the modeled specimen for $[011]_{\gamma}$ loading direction, at a nominal strain of 15%, (a) shear slip γ , (b) lattice rotation in degrees.

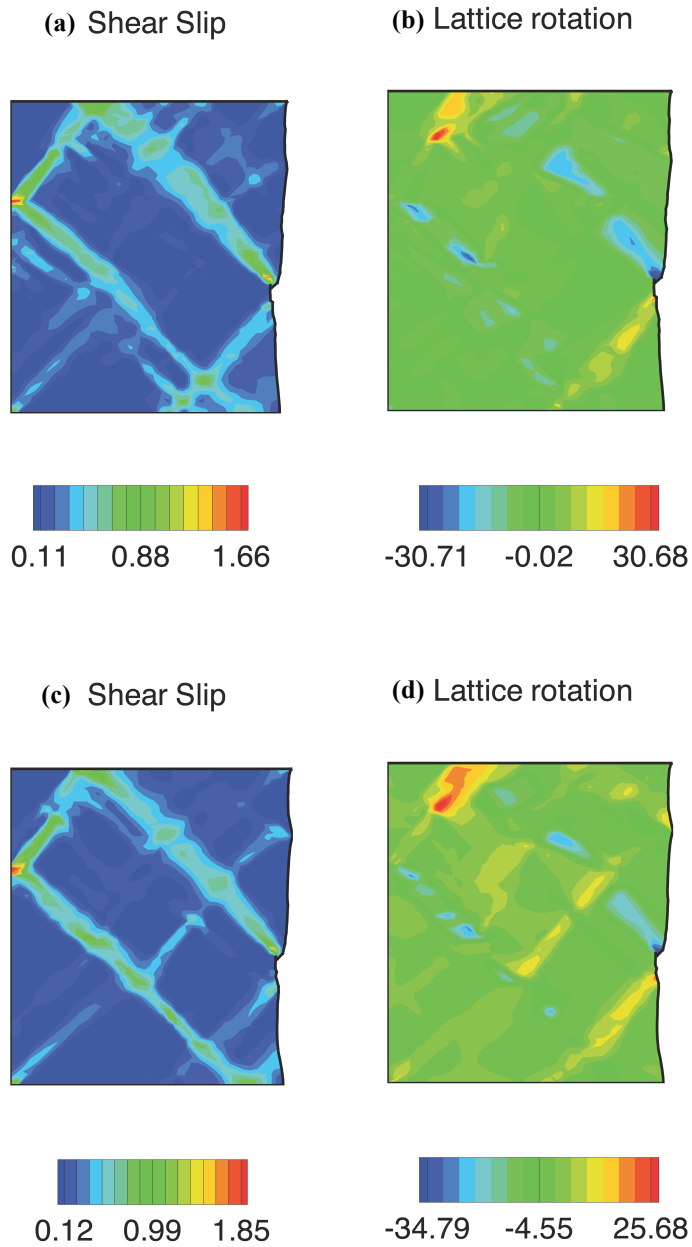


Figure 6.12 Results obtained for the modeled specimen with 10% of retained austenite, at a nominal strain of 15%. (a) shear slip γ , (b) lattice rotation in degrees, both for retained austenite placed inside the blocks (Model 1). (c) shear slip γ , (d) lattice rotation in degrees, both for retained austenite placed at block boundary (Model 2).

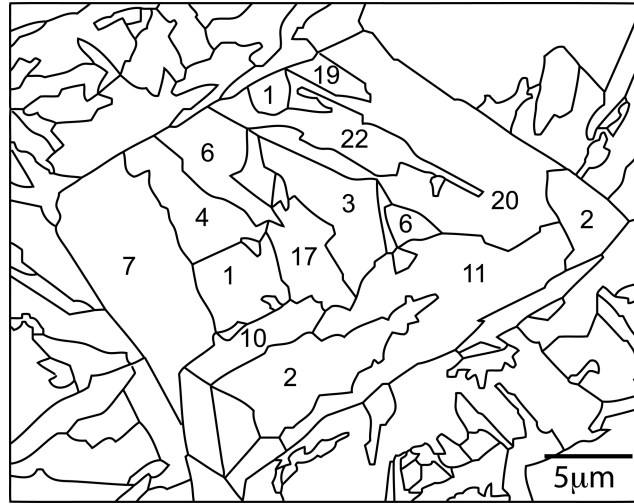


Figure 6.13 Physically representative microstructure mapped from SEM/EBSD steel microstructure and the distribution of variants, [6].

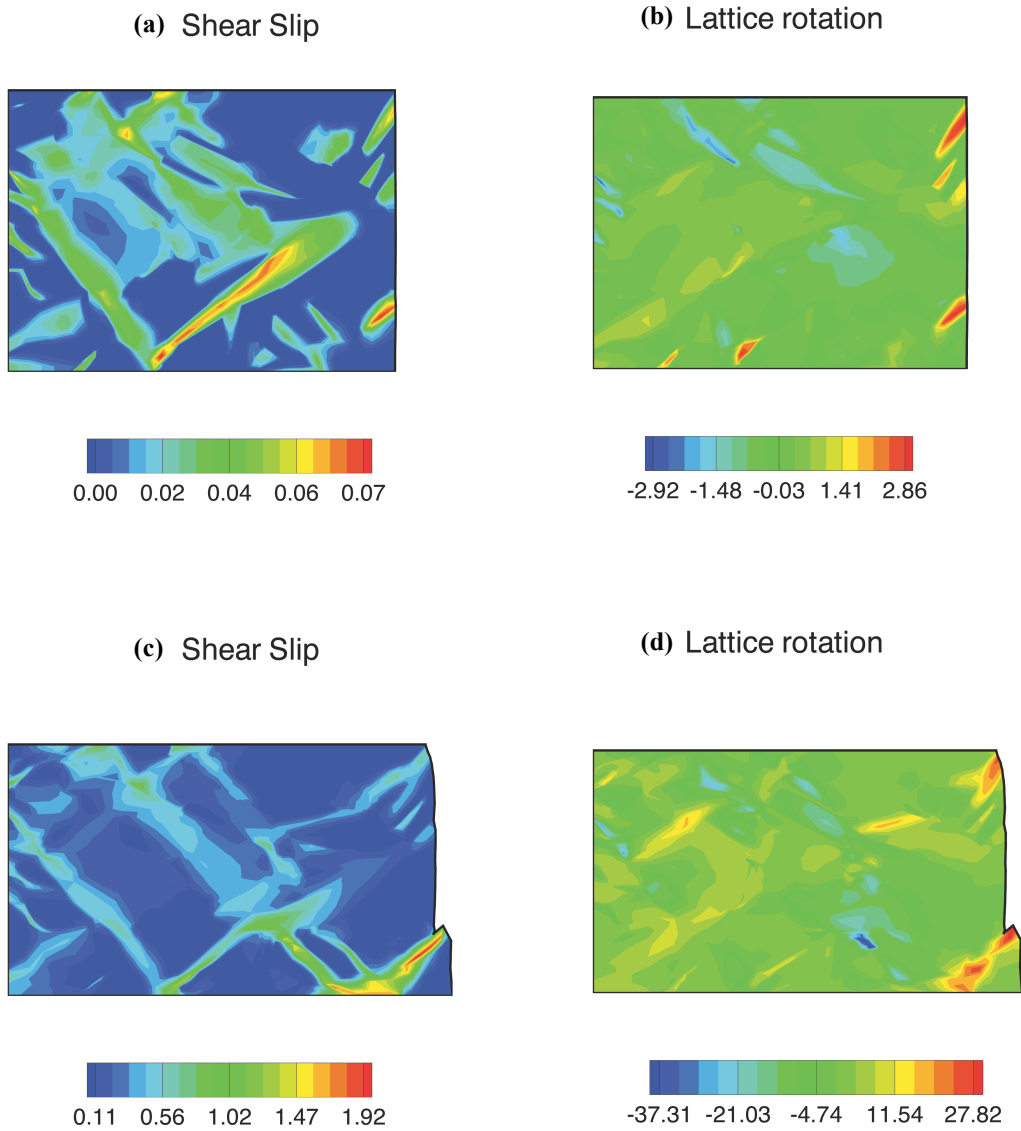


Figure 6.14 Results obtained from mapped experimental specimens, at nominal strains of 5% and 15%. (a) shear slip γ , (b) lattice rotation in degrees, both at nominal strain of 5%. (c) shear slip γ , (d) lattice rotation in degrees, both at a nominal strain of 15%.

CHAPTER 7

SHEAR PIPES EFFECT AND SHEAR-STRAIN LOCALIZATION IN LATH MARTENSITIC MICROSTRUCTURES

A three-dimensional multiple-slip dislocation-density-based crystalline formulation, specialized finite-element formulations, and L_∞ Voronoi tessellations adapted to martensitic orientations, were used to investigate dislocation-density activities and failure in high strength martensitic steels. In this chapter, the formulation is used to investigate dislocation-density activities and shear-strain localization in high strength martensitic steels, and interactions with defects within the shear-strain localization region. The effects of the loading direction, variant arrangement based upon the compatibility of the slip-systems between variants, and the loading direction and long direction of laths have been investigated. Furthermore, the interaction with different defects, such as microcracks, is investigated for quasi-static and dynamic loadings. The analysis indicates that for certain loading directions, certain slip-systems aligns with the maximum resolved shear stress direction and with the

long direction of the blocks, and when combined with the low angle boundaries between blocks, it acts as shear pipes for the localization of dislocation-densities and shear-strains.

7.1 Shear-Strain Localization and Shear Pipes Effect Model

The multiple-slip dislocation-density based crystal plasticity formulation, the specialized finite element algorithm, and the L_∞ Voronoi scheme were used to investigate the shear-strain localization and failure behavior of martensitic steel. The martensite orientation is represented as outlined in Chapter 3. The parent austenite grain is assumed to be oriented based on the loading plane of $(001)_\gamma$, and the loading direction of $[010]_\gamma$. The K-S relation is adapted as the martensite OR, and $\{111\}_\gamma$ is assumed as the habit plane. The martensite morphology is generated by the L_∞ Voronoi tessellation scheme to generate block and packet microstructures relative to the parent austenite grain. A representative aggregate size was determined by modeling the response with different aggregate sizes. In this study, 40 martensitic grains are distributed randomly with 14 packets, with an average of 3 blocks per packet as shown in Figure 7.1. For the quasi-static case, the axial quasi-static tension (0.0001/s strain-rate) is applied along the loading direction, as shown in Figure 7.1.

Based on a convergence analysis, 2501 four noded quadrilateral elements were used with a plane strain analysis for a specimen size of 3.2 mm by 6.2 mm. The material properties that are used here are representative of low nickel alloy steel (Table 6.1), and were validated with experimental results, as detailed in Chapter 6, on 10% Ni steel alloy under quasi-static compression loading.

To elucidate the local microstructural mechanisms, the contours for the mobile dislocation-densities (Figures 7.2a-7.2b), and the immobile dislocation-densities (Figures 7.2c-7.2d) corresponding to the two most active slip-systems, at a nominal strain of 7.5% are shown. The maximum mobile dislocation-densities are $0.67 \times 10^{14} \text{ m}^{-2}$ for slip-system $(112)/[11\bar{1}]$, and $0.59 \times 10^{14} \text{ m}^{-2}$ for slip-system $(\bar{1}12)/[1\bar{1}1]$. The maximum immobile dislocation-densities for the two slip-systems are $1.52 \times 10^{15} \text{ m}^{-2}$ for slip-system $(112)/[11\bar{1}]$, and $1.03 \times 10^{15} \text{ m}^{-2}$ for slip-system $(\bar{1}12)/[1\bar{1}1]$. The evolution of dislocation-densities along selected blocks and along low-angle grain boundaries (as noted earlier grain boundaries are equivalent to block boundaries) result in an increase in dislocation-densities values and a localization of shear slip as shown in Figure 7.3a. These increases in dislocation-density are due to an alignment of the load towards the $[010]_y$ direction. $[011]_y$ is a maximum resolved

shear stress direction for this load, since it is at 45° from the loading direction. $[011]_\gamma$ is also parallel to the long direction of laths and blocks, and parallel to the slip direction $[111]_\alpha$ based on the K-S OR. This special configuration aligns the slip-systems with the maximum resolved shear stress direction with the long direction of the blocks, and when combined with the low angle boundaries between blocks, acts as shear pipes for the localization of dislocation-densities and shear-strains.

To further quantify the orientation effects on failure, the OR between loading direction, slip-systems, and the lath long directions, the stereographic projection of the slip-systems of variant #3 relative to the loading direction, the locus of maximum resolved shear stress (a circle that is 45° from the loading direction), and the long direction of the variant are plotted in Figure 7.4. As can be seen, the slip direction $[\bar{1}\bar{1}1]_\alpha$ aligns with $[0\bar{1}1]_\gamma$, which is the long direction of the laths inside the block and the maximum resolved shear direction for the uniaxial loading direction of $[010]_\gamma$. Furthermore, slip-plane (112) is almost coincident with the maximum resolved shear locus. This would activate slip-system (112) / $[11\bar{1}]$ in this variant as substantiated by the results shown in Figure 7.2a.

Similarly for variant #14, the slip direction $[\bar{1}\bar{1}\bar{1}]_{\alpha'}$ has the low angle GB relation (10.5°) with the direction $[0\bar{1}1]_{\gamma}$. Slip-plane $(\bar{1}12)$ is nearly adjacent to the maximum resolved shear stress direction. This activates slip-system $(\bar{1}12)/[\bar{1}\bar{1}\bar{1}]$ as confirmed by the results shown in Figure 7.2b. Similar behavior can be obtained for other variants, such as variants 6, 13, and 16. Furthermore, the shear slip is not impeded by these low-angle boundaries, which leads to shear-strain accumulation and localization as shown in Figure 7.3a.

High and low angle GB relations can be obtained relative to variant sequences. These sequences can be used to determine the compatibility of the slip systems between variants, a summary of these relations is listed for variants 1-6 (V1-V6) in table 7.1, where it can be divided to four groups.

For group 1, crystals are based on twin relations; compatible slip-systems are parallel and aligned with the long direction of laths. Group 2 are variants with low angles of approximately 10° . Group 3 relates compatible slips-systems with low angle GBs (approximately 10°). Group 4 relates compatible slip-systems with high angle GBs (approximately 21°). Furthermore, relations can be obtained for variants belonging to different packets. For a loading direction of $[010]$, slips-systems $(112)/[\bar{1}\bar{1}\bar{1}]$, and $(\bar{1}12)/$

$[\bar{1}\bar{1}1]$ are the most active slip system, and are aligned with the long direction of laths. High angle relations can impede the dislocation-density evolution between certain variant pairs, while low angle relations can promote dislocation-density transmission between other variants, which can lead to shear-strain accumulation and localization. It should also be noted that for a slip direction of $[011]_{\alpha}$, the slip direction is continuous through the six variants and other variants (relative to austenite orientation) as a result of the martensitic transformation, and it is not initially active relative to the $[010]_{\gamma}$ loading direction.

As shown in Figure 7.3a, the accumulated maximum plastic shear is 0.45 at a nominal strain of 7.5%. This large value at a relatively low nominal strain is due to dislocation-density activities at the low angle GBs, geometrical softening, and the orientation effects associated with the shear pipes, which are essentially conduits for localization in martensitic steels as noted earlier. The geometrical softening occurs due to the large lattice rotation that as high as -11.96° (Figure 7.3b). As can be seen from Figure 7.3b, and Figure 7.5a, the rotation aligns incompatible slip-systems in certain variants with the shear-strain localization direction. This results in geometrical softening and is a possible site of failure due to high lattice rotation incompatibilities. This localized rotation around certain triple junctions have

been noted by Harren et al. [1]. The maximum normalized (stress values are normalized by the static yield stress) normal stress is 2.43 and the maximum normalized shear stress is -0.3 (Figure 7.3c-3d) that occur at triple junctions, where rotation incompatibles occur.

The current analysis is consistent with experimental results for shear-strain localization in martensitic carbon steel. As the carbon content in martensitic steel is increased, shear deformation decreases and intergranular failure has been observed [2-3]. As noted by Krauss [2-3], precipitation and interlath cementite are sites of microcrack nucleation. Another contributing factor to decreases in shear-strain localization and plastic strain accumulation can be due to a high frequency of high angle GBs, which have been observed experimentally [4] in steels with high carbon content, which inhibits plastic strain accumulation.

7.2 Microcrack and Shear-Strain Localization Interactions

In this section, we investigate interaction scenarios between shear-strain localization regions and defects that are located in areas of high plastic deformation. We introduce a micro-crack within the shear-strain localization area; the crack length

is 0.4 mm. For this analysis, we use the previous variant arrangement and material properties.

The shear slip and lattice rotation are presented in Figure 7.6. The maximum shear slip at a nominal strain of 7.5% is 0.54 (Figure 7.6a). The maximum lattice rotation at a nominal strain of 7.5% is 21.52° (Figure 7.6b). Furthermore, the microcrack results in a lattice rotation misfit at a triple junction, Figure 7.5b, which leads to significant geometrical softening, and subsequently promotes increased shear-strain accumulation and localization.

7.3 Dynamic Behavior and Shear Band Formation

In this section, we investigate the dynamic behavior of lath martensitic steels. For this analysis, we use the previous variant arrangement, and material properties. We investigate behavior for loading strain rates of 120/s (Model 1) and 12,000/s (Model 2).

The shear slip, lattice rotation, normal stresses and temperature are shown in Figure 7.7 for Model 1 at a nominal strain of 7.5%. The maximum shear slip is

0.35 (Figure 7.7a). The maximum lattice rotation stress is -14.84° (Figure 7.7b). The maximum normalized normal stress is 3.06 (Figure 7.7c). The maximum temperature is 342°K (Figure 7.7d). Due to low strain rate the shear-strain localization pattern is similar to that results in quasi-static case.

For Model 2, at a nominal strain of 7.5%, the maximum shear slip is 0.45 (Figure 7.8a), the maximum lattice rotation stress is -12.1° (Figure 7.8b), the maximum normalized normal stress is 4.11 (Figure 7.8c), and the maximum temperature is 358°K (Figure 7.8d). As can be observed from these results, the shear-strain localization is much narrower than that of the 1200/s case. This is consistent with the experimental observations of Dodd and Bai [5]. This narrowing of the shear-localization area width is due to the increased strain-rate effects that do not allow the accumulation of strains over wide regions.

7.4 Voids/Inclusions and Shear-Strain Localization Interactions

Voids and inclusions play a major role in the fracture and failure behavior of high-strength steels, see, for example, [6-10]. To investigate these effects, we placed

voids at certain triple junctions. Voids can be thought as previously existing voids, or inclusions [9-10]. Voids volume fraction is 0.056% with nine voids placed at triple junctions, as shown in Figure 7.9. The voids radius was chosen as 20 μm , which is comparable with observed voids size in steels [8]. For this analysis, we used the previous variant arrangement, boundary conditions, and strain-rate of 12,000/s (Model 2).

For Model 2, at a nominal strain of 7.5%, the maximum shear slip is 1.37 (Figure 7.10a), the maximum lattice rotation stress is -25.52° (Figure 7.10b), the maximum normalized normal stress is 3.93 (Figure 7.10c), and the maximum temperature is 467 $^\circ\text{K}$ (Figure 7.10d). As can be observed from these results, the shear-strain localization is much higher than the case without inclusions; this increase is due to the increase geometrical and thermal softening attributed voids/inclusions. Furthermore, the pattern of the shear-strain localization is different and looks more similar to the quasi-static case; this is a result of voids localizing the inelastic shear at early stages of deformation leading to increase in plastic shear values at these bands region, especially around and between voids as shown in Figure 7.10.

7.5 Summary

A physically-based microstructural representation of variants, blocks, packets, and initial dislocation-densities for lath martensitic steels was developed. A multiple-slip rate-dependent crystalline constitutive formulation that is coupled to the evolution of mobile and immobile dislocation-densities, and specialized finite-element schemes were used to investigate shear-strain localization in lath martensitic steel at quasi-static and dynamic strain-rates. Variants were represented by arrangements of packets and blocks that account for different slip planes and orientations. These variant arrangements can be categorized, through different arrangements of the blocks, as either random low or high angle GBs.

It has been shown that for a loading direction of $[010]_y$, the maximum resolved shear stress direction, the slip directions and the long direction of blocks are almost coincident. When combined with low angle GBs between blocks and slip-system compatibility, these results in shear pipes, which promote extensive shear-strain localization.

For the quasi-static case, geometrical softening occurs as a result of rotation incompatibility at specific triple junctions. This rotation incompatibility significantly

increases with the presence of a microcrack within the shear-strain localization area.

The effects of dynamic loading can be observed at higher strain rates; this is due to the interrelated effects of the thermal and geometrical softening and dynamic interactions due to wave propagation. At the high strain rate of 12,000/s, shear-strain localization is narrower than that of the 1200/s case. The effects of inclusions on dislocation activities and dynamic behavior of martensitic steels was also investigated by placing voids at certain triple junctions. The results clearly show the effect of voids/inclusions in promoting shear-strain localization.

The present study underscores how the local and unique microstructures related with the ORs of martensitic steel are intricately related to shear-strain localization and material failure at physical different scales that are unique to martensitic steels.

REFERENCES

- [1] Harren S. V., Deve H. E., and Asaro R. J., 1988, "Shear band formation in plane strain compression," *Acta Metall.*, 32, pp. 2435-2480.
- [2] Krauss G., 2001, "Deformation and Fracture in Martensitic Carbon Steels Tempered at Low Temperature," *Metall. Mater. Trans. A*, 32B, pp. 205-221.
- [3] Saeglitz M., and Krauss G., 1997, "Deformation, Fracture, and Mechanical Properties of Low-Temperature-Tempered Martensite in SAE 43xx Steels," *Metall. Mater. Trans.*, A 28A, pp. 377-387.
- [4] Morito S., Tanaka H., 2003, *et al.*, "The Morphology and Crystallography of Lath Martensite in Fe-C Alloys," *Acta Mater.*, 51, pp. 1789-1799.
- [5] Dodd B., and Bai Y., 1985, "Width of Adiabatic Shear Bands," *Mat. Sci. Technol.*, 1, pp. 38-40.
- [6] Garrison W. M., and Moody N. R., 1987, "Ductile Fracture," *J. Phys. Chem. Solids*, 48(11), pp. 1035-1074.
- [7] Garrison W. M. and Wojcieszynski A. L., 2007, "A Discussion of the Effect of Inclusion Volume Fraction on the Toughness of Steel," *Mater. Sci. Eng A-Struct.*, 464, pp. 321-329.

[8] Minnaar K., and Zhou M., 1998, "An Analysis of the Dynamic Shear Failure Resistance of Structural Metal," *J. Mech. Phys. Solids*, 46-10, pp. 2155-2170.

[9] Lorio L. E., and Garrison W. M., 2002, "Effects of Gettering Sulfur as CrS or MnS on Void Generation Behavior in Ultra-High Strength Steel," *Scripta Mater.*, 46(12), pp. 863-868.

[10] Bandstra J. P., Koss D. A., *et al.*, 2006, "Modeling void coalescence during ductile fracture of a steel," *Mater. Sci. Eng A-Struct.*, 366(2), pp. 269-281.

**Table and Figures for
Chapter 7**

Table 7.1. The angle between slip systems for variants 1-6 (a packet with habit plane of $(111)_\gamma$) that can be divided into groups of high and low angle GB directions. (*) denotes compatibility between slip systems that are not initially active relative to loading direction $[010]_\gamma$.

Group	Variants pair	Angle between
1	V1-V2*, V3-V4, V5-V6	0 degree
2	V1-V4, V3-V-6, V2-V5	10.5 degree
3	V1-V3, V1-V5*, V2-V4*, V2-V6, V3-V5, V4-V6	10.5 degree
4	V1-V6, V2-V3, V4-V5*	21 degree

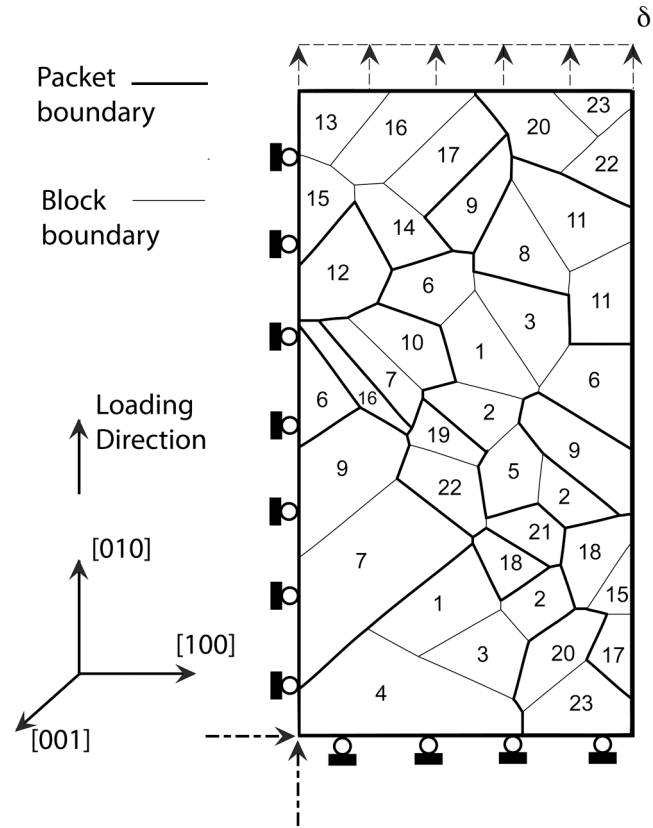


Figure 7.1 Microstructural model used in the current study, the distribution of variants in blocks and packets (variants numbered as indicated in Table 3.4), loading, geometry, and boundary conditions.

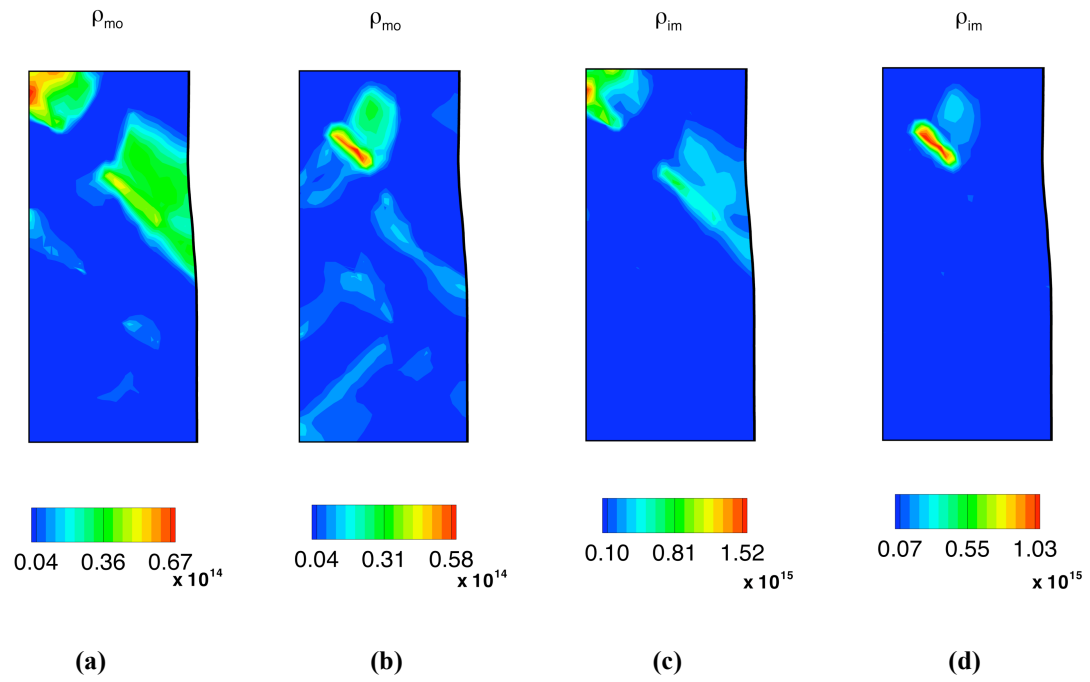


Figure 7.2 Normalized mobile and immobile dislocation-densities at a nominal strain of 7.5% for most active slip-systems for (a) slip-system $(112)/[11\bar{1}]$, (b) slip-system $(\bar{1}12)/[1\bar{1}1]$, (c, d) immobile dislocation-densities, (c) slip-system $(112)/[11\bar{1}]$, (d) slip-system $(\bar{1}12)/[1\bar{1}1]$.

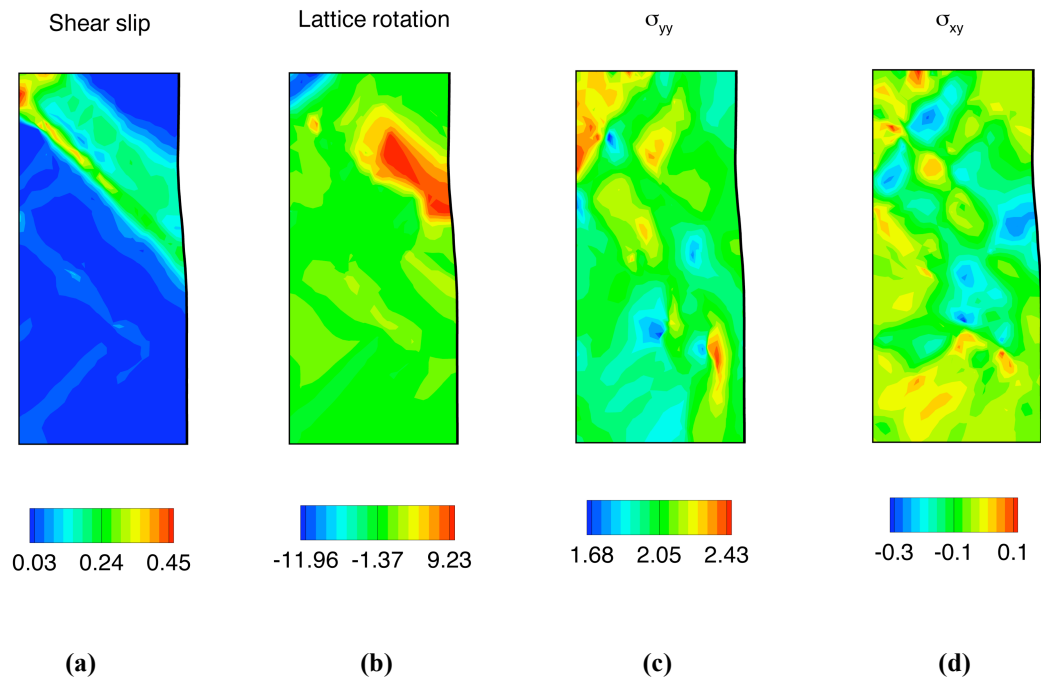


Figure 7.3 Behavior at a nominal strain of 7.5% (a) Shear slip contours, (b) lattice rotation in degrees, (c) normalized normal stress, (d) normalized shear stresses. Stresses values are normalized by the static yield stress.

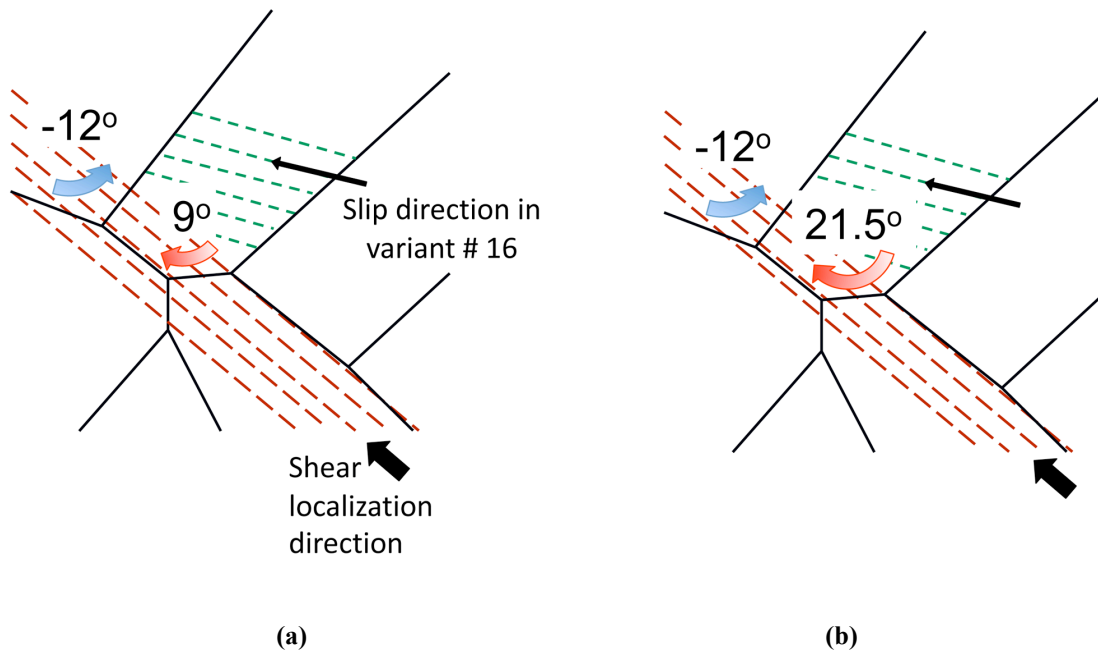


Figure 7.5 Rotation misfit at triple junction in shear localization area, (a) without microcracks, (b) with microcrack in the shear-strain localization region.

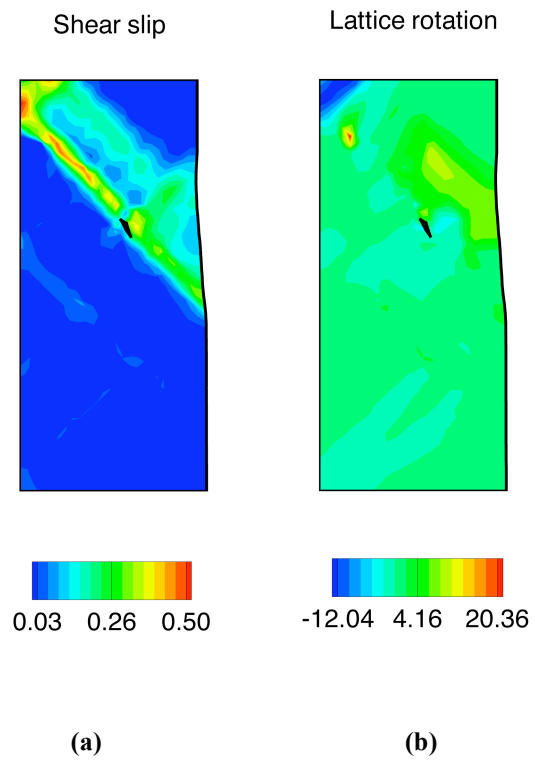


Figure 7.6 Shear localization - microcrack interaction at a nominal strain of 7.5% (a) shear slip, (b) lattice rotation.

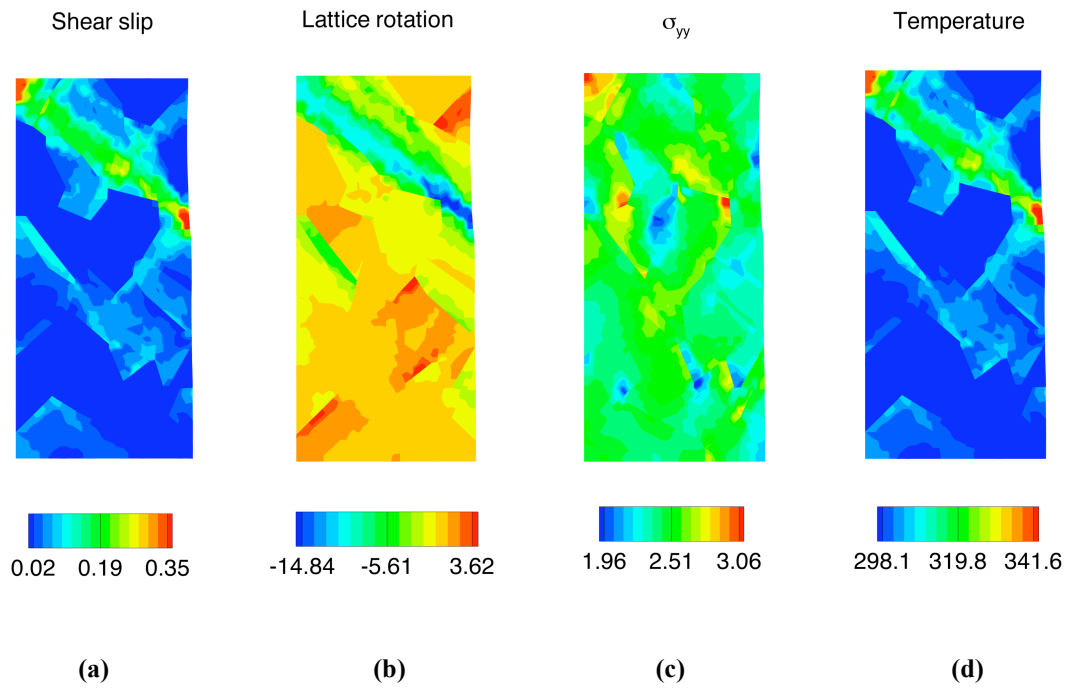


Figure 7.7 Dynamic loading (120/sec strain rate), at a nominal strain of 7.5% (a) Shear slip contours, (b) lattice rotation in degrees, (c) normalized normal stress, (d) temperature in degrees Kelvin.

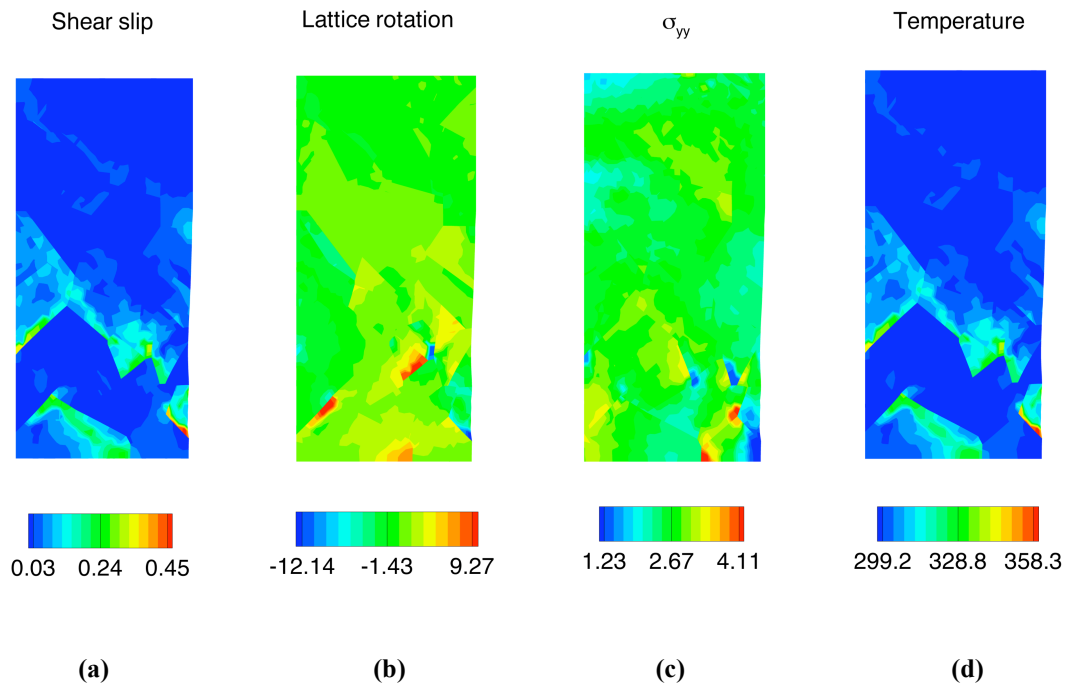


Figure 7.8 Dynamic loading (12,000/sec strain rate), at a nominal strain of 7.5% (a) Shear slip contours, (b) lattice rotation in degrees, (c) normalized normal stress, (d) temperature in degrees Kelvin.

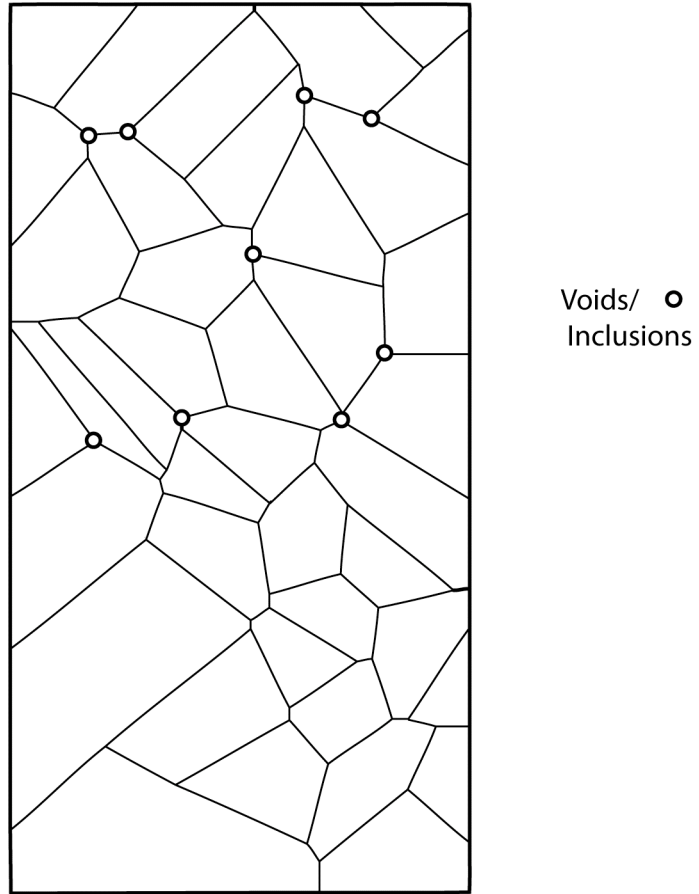


Figure 7.9 Microstructural model and inclusion distribution

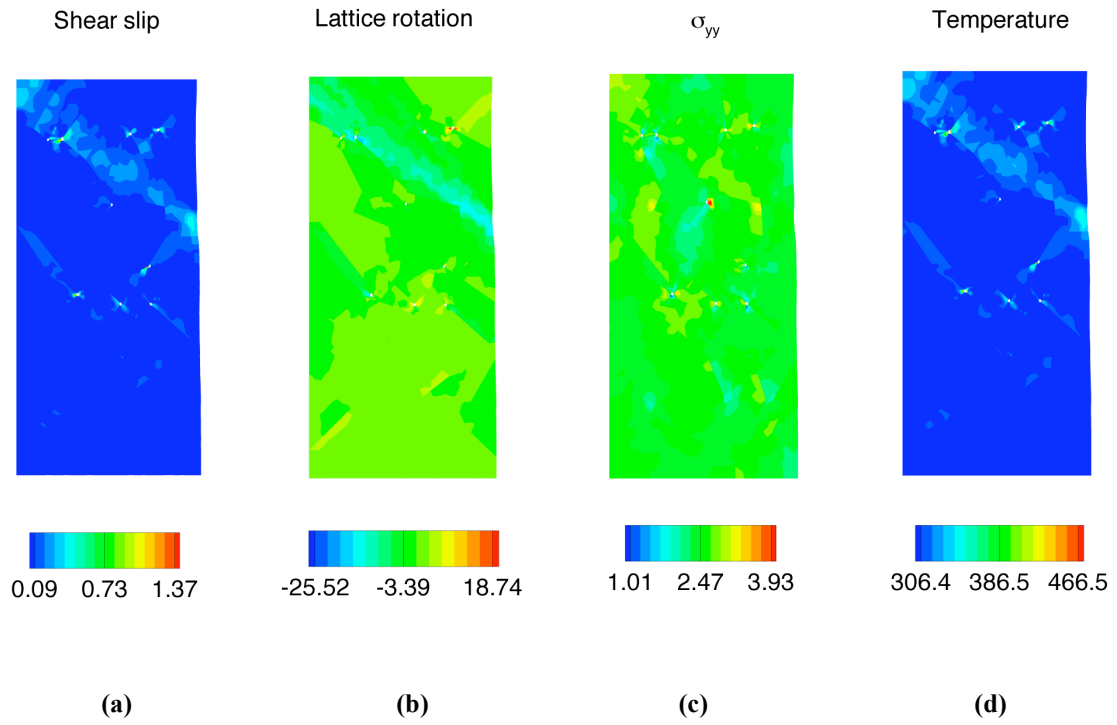


Figure 7.10 Dynamic loading (12,000/sec strain rate) – void/inclusion interactions, at a nominal strain of 7.5% (a) Shear slip contours, (b) lattice rotation in degrees, (c) normalized normal stress, (d) temperature in degrees Kelvin.

CHAPTER 8

FRACTURE EVOLUTION IN LATH MARTENSITIC MICROSTRUCTURES

The three-dimensional multiple-slip dislocation-density-based crystalline formulation, specialized finite-element formulations, and L_∞ Voronoi tessellations adapted to martensitic orientations, presented in previous chapters, were used to investigate dislocation-density activities and crack tip blunting in high strength martensitic steels. The formulation is used to investigate dislocation-density activities and crack tip blunting in high strength martensitic steels, and interaction with voids/inclusions ahead of the crack tip region. Furthermore, the effects of variant distributions and arrangements are investigated for different crack and void interaction arrangements and distributions.

8.1 Transgranular and Intergranular Failure Models

The multiple-slip dislocation-density based crystal plasticity formulation, the specialized finite element algorithm, and the L_∞ Voronoi scheme were used to investigate the fracture behavior of martensitic steel. The parent austenite grain is assumed to be oriented

based on the loading plane of $(001)_\gamma$, and the loading direction of $[010]_\gamma$. The K-S relation is adapted as the martensite OR, and $\{111\}_\gamma$ is assumed as the habit plane. The martensite morphology is generated by the L_∞ Voronoi tessellation scheme to generate block and packet microstructures relative to the parent austenite grain. A representative aggregate size was determined by modeling the response with different aggregate sizes. In this study, 40 martensitic blocks were used for modeling martensitic steels with a pre-existing crack to determine how intergranular or transgranular crack propagation can occur. The first arrangement (Model 1), Figure 8.1a, is for a variant arrangement that corresponds to a random low angle GBs (as noted earlier, GBs are equivalent to block boundaries) orientation. The second case (Model 2), Figure 8.1b, is for a variants arrangement for a random high angle GBs arrangement. The high and low angles relations are obtained relative to specific variant sequences. These sequences determine the compatibility of the slip systems between variants, which depend on the martensitic transformation, a summary of these relations is listed for variants 1-6 (V1-V6) was presented in table 7.1.

The macroscopic crack (Figure 8.1c) has a normalized length of a/w of 0.1, where a is the crack length and w is the specimen width. The axial quasi-static tension (0.0001/s) is applied along the loading direction, as shown in Figure 8.1c.

Based on a convergence analysis, 2501 four noded quadrilateral elements were used with a plane strain analysis for a specimen size of 3.2 mm by 6.2 mm. Both models have the same loading directions, mesh, and material properties. The only difference between the models is in the variant arrangements. The material properties that are used here are representative of low nickel alloy steel, and were validated with experimental results, as detailed in Chapter 6, on 10% Ni steel alloy under quasi-static compression loading.

To elucidate the local microstructural mechanisms, the contours for the mobile dislocation-densities (Figure 8.2), and the immobile dislocation-densities (Figure 8.5) corresponding to the low angle blocks boundaries (Model 1) most active three slip-systems, at a nominal strain of 7.5% are shown. The maximum normalized (the mobile densities are normalized by the saturated mobile dislocation-density) mobile dislocation-densities are 0.68 for slip-system $(112) / [11\bar{1}]$, and 0.12 for slip-system $(\bar{1}12) / [1\bar{1}1]$. The maximum normalized (the immobile densities are normalized by the saturated immobile dislocation-

density) immobile dislocation-densities for the two slip-systems are 0.55 for slip-system $(112) / [11\bar{1}]$, and 0.05 for slip-system $(\bar{1}12) / [1\bar{1}1]$. The evolution of dislocation-densities ahead of the crack tip and along low-angle GBs result in an increase in dislocation-densities values ahead of crack tip and a localization of shear slip as shown in Figure 8.4a, causing the crack tip to blunt. These increases in dislocation-density are due to an alignment of the load towards the $[010]_y$ direction. $[011]_y$ is a maximum resolved shear stress direction for this load, since it is at 45° from the loading direction. $[011]_y$ is also parallel to the long direction of laths and blocks, and parallel to the slip direction $[111]_\alpha$ based on the K-S OR. This special configuration aligns the slip-systems with the maximum resolved shear stress direction with the long direction of the blocks, and when combined with the low angle boundaries between blocks, acts as shear pipes for the localization of dislocation-densities and shear strains. The increase of dislocation transmission from the crack tip and through GBs can result in crack blunting and transgranular failure, which is consistent with ductile-brittle behavior in f.c.c. and b.c.c. metals, see, for example, [1-4].

To further underscore the OR between loading direction, slip-systems, and the lath long directions, the stereographic projection of the slip-systems of variant #3 relative to the

loading direction, the locus of maximum resolved shear stress (a circle that is 45° from the loading direction), and the long direction of the variant are plotted in Figure 8.5. As can be seen, the slip direction $[\bar{1}\bar{1}1]_{\alpha'}$ aligns with $[0\bar{1}1]_{\gamma}$, which is the long direction of the laths inside the block and the maximum resolved shear direction for the uniaxial loading direction of $[010]_{\gamma}$. Furthermore, slip-plane (112) is almost coincident with the maximum resolved shear locus. This would activate slip-system (112)/ $[\bar{1}\bar{1}\bar{1}]$ in this variant as is confirmed by the results shown in Figure 8.2a.

Similarly for variant #14, the slip direction $[\bar{1}\bar{1}\bar{1}]_{\alpha'}$ has the low angle GB relation (10.5°) with the direction $[0\bar{1}1]_{\gamma}$. Slip-plane (112) is nearly adjacent to the maximum resolved shear stress direction. This activates slip-system (112)/ $[\bar{1}\bar{1}\bar{1}]$ as confirmed by the results of Figure 8.2a. Similar behavior can be obtained for other variants, as active slip-systems in variants 6, 13, 16 relate with low angle GB in between. Furthermore, the slip is not impeded by these low-angle boundaries, which lead to shear-strain accumulation and localization as shown in Figure 8.4a.

As shown in Figure 8.4a, the accumulated maximum plastic shear is 3.3 at a nominal strain of 7.5%. This large value is due to dislocation activities at the crack tip, geometrical

softening, and the orientation effects associated with the shear pipes, which are essentially conduits for localization in martensitic steels, for more details see previous chapter . The crack tip blunting and geometrical softening occur due to the large lattice rotation that as high as 37.2° (Figure 8.4b), reaching its maximum at the crack-tip. The maximum normalized (stress values are normalized by the static yield stress) normal stress is 2.93 (Figure 8.4c), and the maximum normalized shear stress is 2.57 (Figure 8.4d). These maximum values occur directly ahead of the crack tip.

For the high angle block boundary model (Model 2), the contours for the mobile dislocation-densities (Figure 8.6), and the immobile dislocation-densities (Figure 8.7) corresponding to most active two slip-systems, at a nominal strain of 7.5% are shown. The maximum normalized mobile dislocation-densities are 0.27 for slip-system $(112) / [11\bar{1}]$, and 0.06 for slip-system $(\bar{1}12) / [1\bar{1}1]$. The maximum normalized immobile dislocation-densities for the two slip-systems are 0.16 for slip-system $(112) / [11\bar{1}]$, and 0.02 for slip-system $(\bar{1}12) / [1\bar{1}1]$. There is significantly lower shear slip and dislocation activities at the crack tip region, and the crack profile is significantly different, as shown in Figure 8.8a. This

difference in behavior can be due to incompatibility between the martensitic variant slip-systems due to the high angle GBs between V6-V1.

As shown in Figure 8.8a, the accumulated plastic shear is lower by a factor of two in comparison with the low-angle GB case. The accumulated maximum plastic shear is 1.67 at a nominal strain of 7.5%, the shear slip is concentrated directly ahead of the crack-tip and along GBs directly ahead of the crack-tip region. The maximum lattice rotation is 33.28° (Figure 8.8b). Higher normal stress at the crack-tip and along the GBs are shown in Figure 8.8c. The maximum normalized normal stress is 3.94 (Figure 8.8c), and the maximum normalized shear stress is 1.47 (Figure 8.8d). These maximum values occur ahead of the crack tip. The lower plasticity and dislocation-densities and higher stresses are indications of potential sharp crack growth along the GBs.

The current analysis is consistent with experimental results for fracture in martensitic carbon steel. As carbon content in martensitic steel is increased, brittle behavior with intergranular growth is observed [5-6]. As noted by Krauss [5-6], precipitation and interlath cementite are sites of brittle fracture nucleation. Another contributing factor to brittle fracture can be due to a high frequency of high angle GBs that have been observed experimentally by

Morito *et al.* [7] with increasing carbon percentage. Furthermore, precipitation at GBs could impede the dislocation transmission at GBs resulting in intergranular failure modes.

8.2 Voids-Crack Tip Interactions

In this section, we investigate interaction scenarios between cracks and voids placed at triple junctions within areas of high plastic deformation (Model 1a for low angle GBs, and Model 2a for high angle GBs) and directly ahead of the crack tip (Model 1b for low angle GBs, and Model 2b for high angle GBs), as shown in Figure 8.9. The void radius is chosen as 0.02 mm, which is comparable with microvoid in steels [8]. For this analysis, we use the previous variant arrangement, and the same mesh for the void arrangements. Voids can be thought as previously existing voids, or inclusions at triple junctions ahead of the crack tip [9-10].

The shear slip and normalized normal stress for both models are presented in Figures 8.10-8.11. The maximum shear slip at a nominal strain of 7.5% is 3.18 for Model 1a, 3.48 for Model 1b, 3.75 for Model 2a, and 3.52 for Model 2b, Figure 8.10. The maximum normalized normal stress at a nominal strain of 7.5% is 2.85 for

Model 1a, 3.02 for Model 1b, 1.28 for Model 2a, and 1.36 for Model 2b, Figure 8.11.

As seen for models with voids within areas of high plastic deformation (Model 1a, 2a), there are more microvoid interactions for random low angle GBs (Model 1a) than random high angle GBs (Model 2a). For this case (Model 1a), as shown in Figures 8.10a, and 8.11a, it is evident that there is preferential void growth along the transgranular planes as a result of dislocation evolution at the void surface, causing the shear slip and the normalized normal stress to decrease.

For models with voids directly ahead of the crack tip (Model 1b, 2b), there are more interactions for random high angle GBs (Model 1b) than random low angle GBs (Model 2b). A decrease in shear slip can be observed in (Figure 8.10d), combined with decrease in normal stresses (Figure 8.11d) that might result from void effects ahead of the crack tip.

8.3 Summary

This investigation provides detailed validated predictive capabilities that have been used to understand complex interrelated physical mechanisms that relate to martensitic microstructures at different physical scales and material failure. A multiple-slip rate-dependent crystalline constitutive formulation that is coupled to the evolution of mobile and immobile dislocation-densities, and specialized computational schemes have been developed to investigate failure behavior in martensitic steels. Variants are represented by arrangements of packets and blocks that account for different slip planes and orientations. These variant arrangements can be categorized, through different arrangements of the blocks, as either random low or high angle GBs.

This methodology was used to characterize sharp and blunt crack growth for different GB orientations. It has been shown that for a loading direction of $[010]_y$, the maximum resolved shear stress direction, slip directions and the long direction of blocks are almost coincident. When combined with low angle GBs between blocks, which acts as shear pipes that increase the dislocation-densities at the crack tip. High dislocation activity and plastic strains along transgranular planes can blunt crack growth for random low angle block

arrangements. On the other hand, low dislocation-density accumulation and plastic slip can result in sharp growth along intergranular directions for high angle block arrangements. This can be due to the incompatibility between slip-systems at high angle grain boundaries, where more grain boundaries (or block boundaries) are available to impede the dislocation transmission between blocks.

Void interactions within areas of high plastic deformation with the pre-existing crack were most pronounced for the random low angle GBs, while void interactions ahead of the crack tip were most pronounced for the random high angle GBs. The present study underscores how the local and unique microstructures related with martensitic steel are intricately related to material failure at physical different scales.

REFERENCES

- [1] Rice J. R., 1992, "Dislocation nucleation from a crack tip: An analysis based on the Peierls concept," *J. Mech. Phys. Solids*, 40(2), pp. 239-271.
- [2] Kameda T., and Zikry M. A., 1998, "Intergranular and transgranular crack growth at triple junction boundaries in ordered intermetallics," *Int. J. Plast.*, 14(8), pp. 689-702.
- [3] Kameda T., Zikry M. A., *Rajendran A. M.*, 2006, "Modeling of grain-boundary effects and intergranular and transgranular failure in polycrystalline intermetallics," *Metall. Mater. Trans. A*, 37A, pp. 2107-2115.
- [4] Qiao Y., and Argon A. S., 2003, "Cleavage cracking resistance of high angle grain boundaries in Fe-3%Si alloy," *Mech. Mater.*, 35, pp. 313-331.
- [5] Krauss G., 2001, "Deformation and Fracture in Martensitic Carbon Steels Tempered at Low Temperature," *Metall. Mater. Trans. A*, 32B, pp. 205-221.
- [6] Saeglitz M., and Krauss G., 1997, "Deformation, Fracture, and Mechanical Properties of Low-Temperature-Tempered Martensite in SAE 43xx Steels," *Metall. Mater. Trans.*, A 28A, pp. 377-387.
- [7] Morito S., Tanaka H., 2003, *et al.*, "The Morphology and Crystallography of Lath Martensite in Fe-C Alloys," *Acta Mater.*, 51, pp. 1789-1799.

- [8] Garrison W. M. and Wojcieszynski A. L., 2007, "A Discussion of the Effect of Inclusion Volume Fraction on the Toughness of Steel," *Mater. Sci. Eng A-Struct.*, 464, pp. 321-329.
- [9] Lorio L. E., and Garrison W. M., 2002, "Effects of Gettering Sulfur as CrS or MnS on Void Generation Behavior in Ultra-High Strength Steel," *Scripta Mater.*, 46(12), pp. 863-868.
- [10] Bandstra J. P., Koss D. A., *et al.*, 2006, "Modeling void coalescence during ductile fracture of a steel," *Mater. Sci. Eng A-Struct.*, 366(2), pp. 269-281.

Figures for Chapter 8

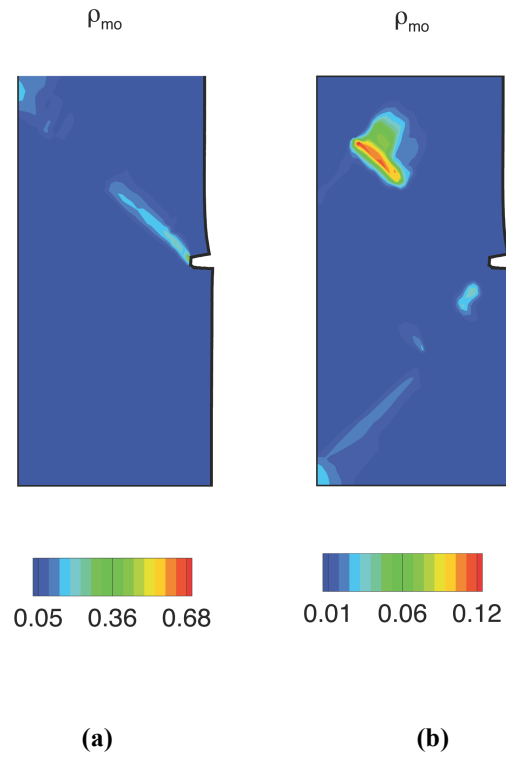


Figure 8.2 Normalized mobile dislocation-densities for most active slip-systems for low angle GBs specimen, (a) slip-system $(112) / [11\bar{1}]$, (b) slip-system $(\bar{1}12) / [1\bar{1}1]$, at a nominal strain of 7.5%. Values normalized by the mobile dislocation-density saturation value, $\rho_{m,s}^{(\alpha)} = 6.86 \times 10^{14} \text{m}^{-2}$.

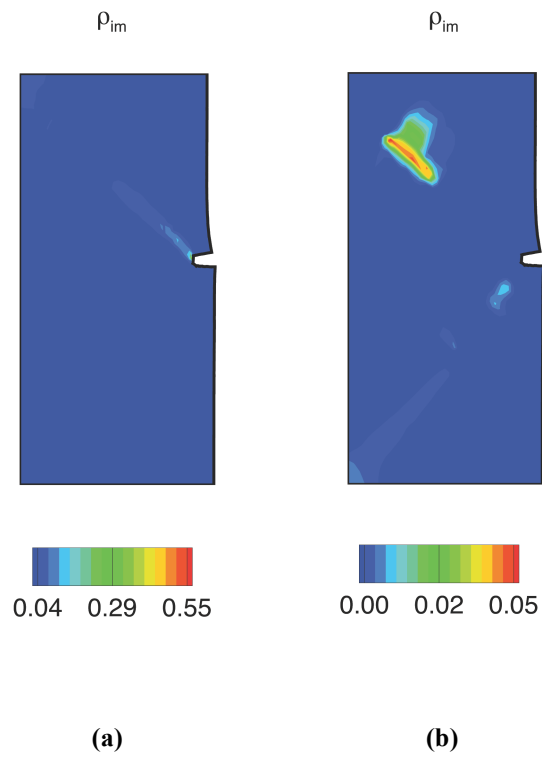


Figure 8.3 Normalized immobile dislocation-densities for most active slip-systems for low angle GBs specimen, (a) slip-system $(112) / [11\bar{1}]$, (b) slip-system $(\bar{1}12) / [1\bar{1}1]$, at a nominal strain of 15%. Values are normalized by immobile dislocation-densities saturation values, $\rho_{im,s}^{(\alpha)} = 1.16 \times 10^{16} \text{m}^{-2}$.

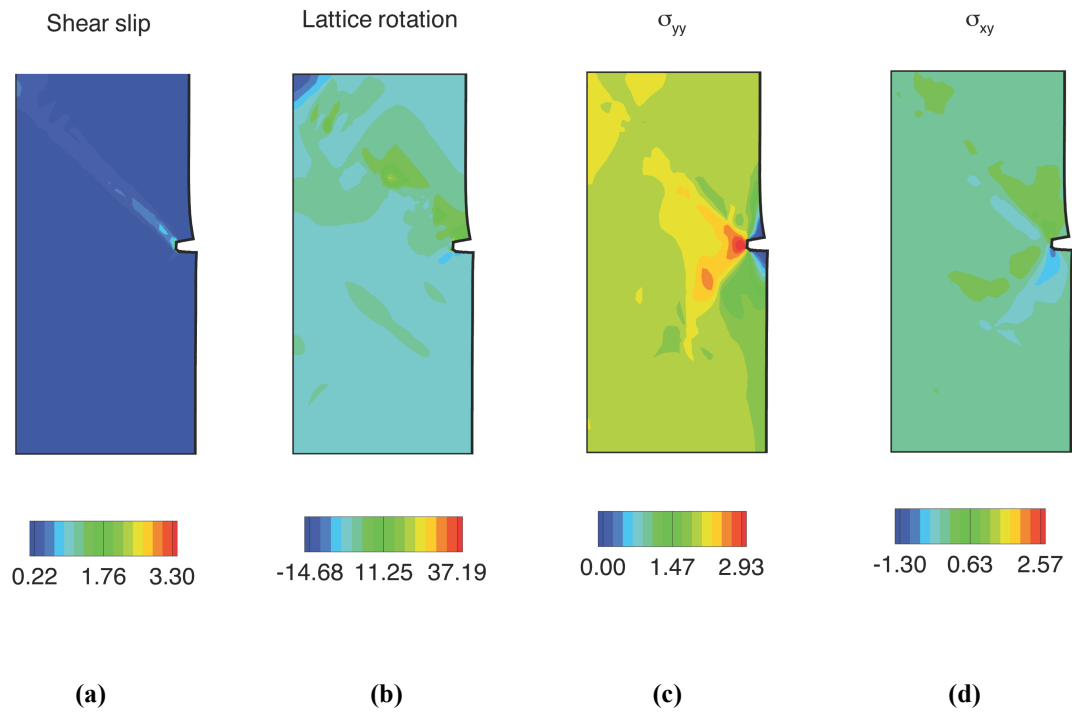


Figure 8.4 Behavior for low angle GBs, at a nominal strain of 7.5% (a) Shear slip contours γ ; (b) lattice rotation in degrees, (c) normalized normal stresses, (d) normalized shear stresses. Stresses values are normalized by the static yield stress.

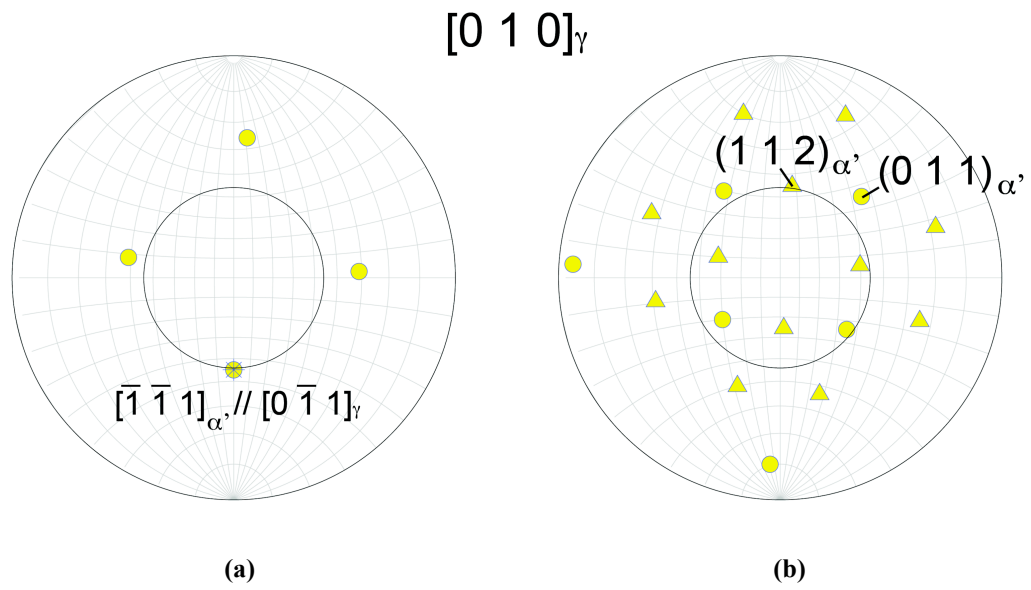


Figure 8.5 $[010]_{\gamma}$ upper hemisphere stereographic projection for variant #3 slip-systems relative to the loading direction, the locus of maximum resolved shear stress (the inner circle) and the long direction of the variants (denoted as * in figure a) (a) the slip directions, (b) the slip planes

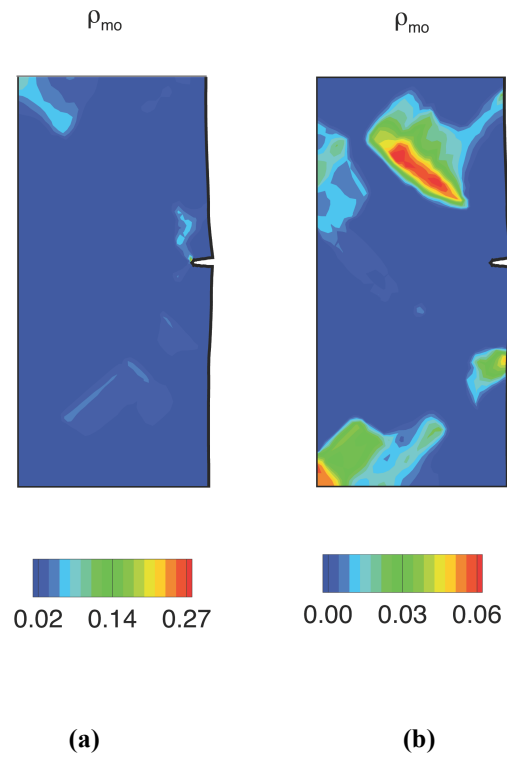


Figure 8.6 Normalized mobile dislocation-densities for the most active slip-systems for high angle GBs for (a) slip-system $(112)/[11\bar{1}]$, (b) slip-system $(\bar{1}12)/[1\bar{1}1]$, at a nominal strain of 15%

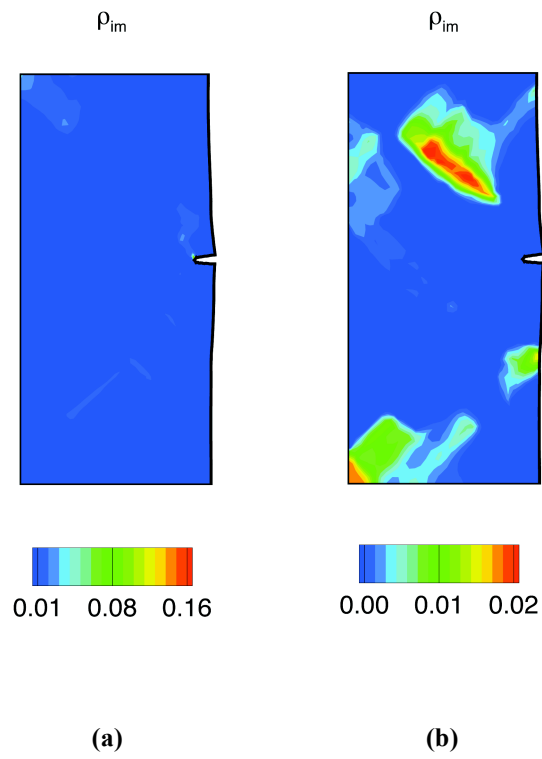


Figure 8.7 Normalized immobile dislocation-densities for most active slip-systems for high angle GBs for (a) slip-system $(112) / [11\bar{1}]$, (b) slip-system $(\bar{1}12) / [1\bar{1}1]$, at a nominal strain of 15%.

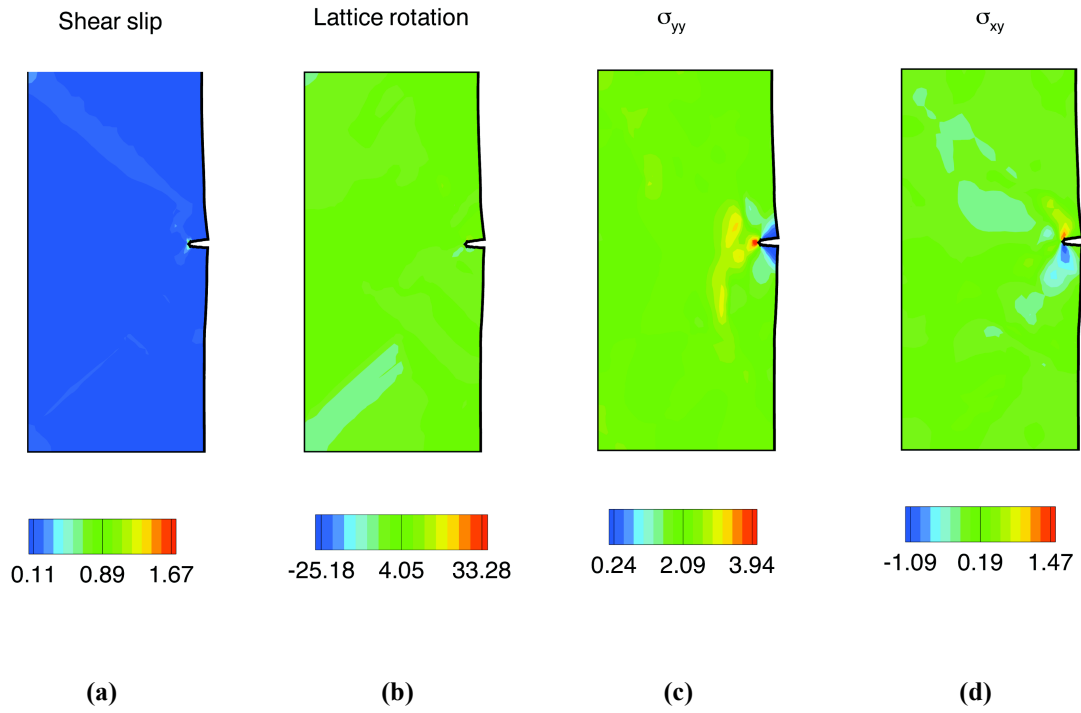


Figure 8.8 Results obtained for the high angle GBs specimen, at a nominal strain of 7.5% (a) Shear slip contours γ , (b) lattice rotation in degrees, (c) normalized normal stresses, (d) normalized shear stresses.

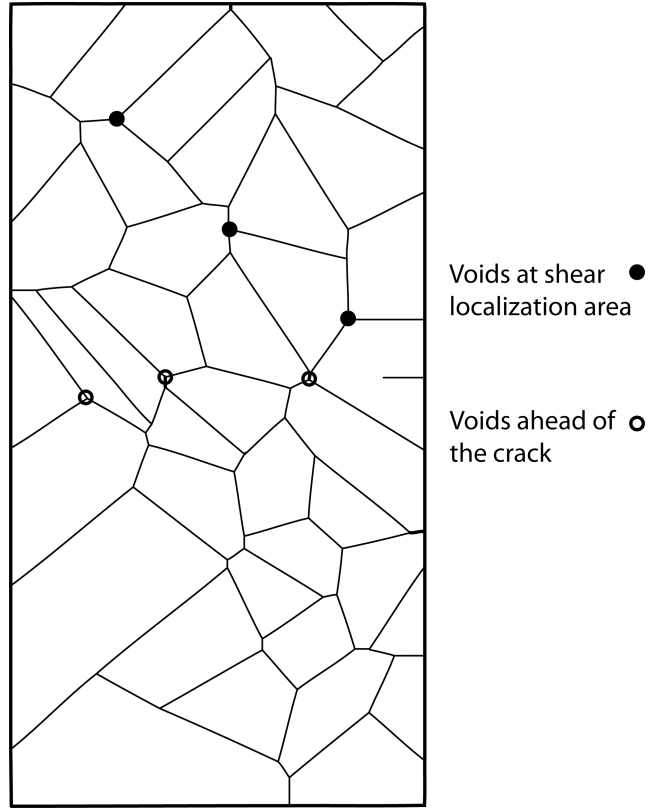


Figure 8.9 Microstructural model and void distribution

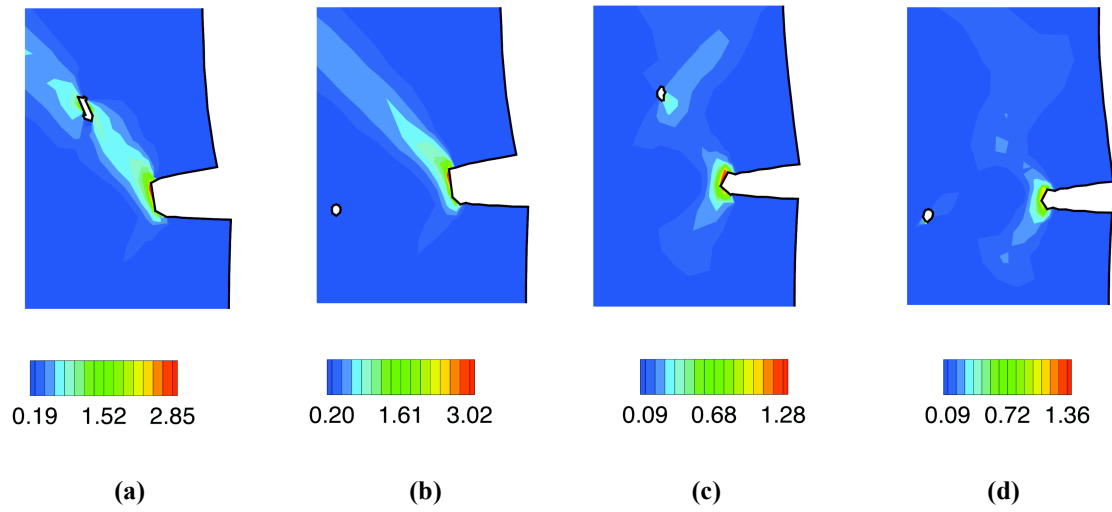


Figure 8.10 Shear slip around the crack tip indicating crack tip-micro voids interactions for low angle GBs (a, b) and high angle GBs (d, c)

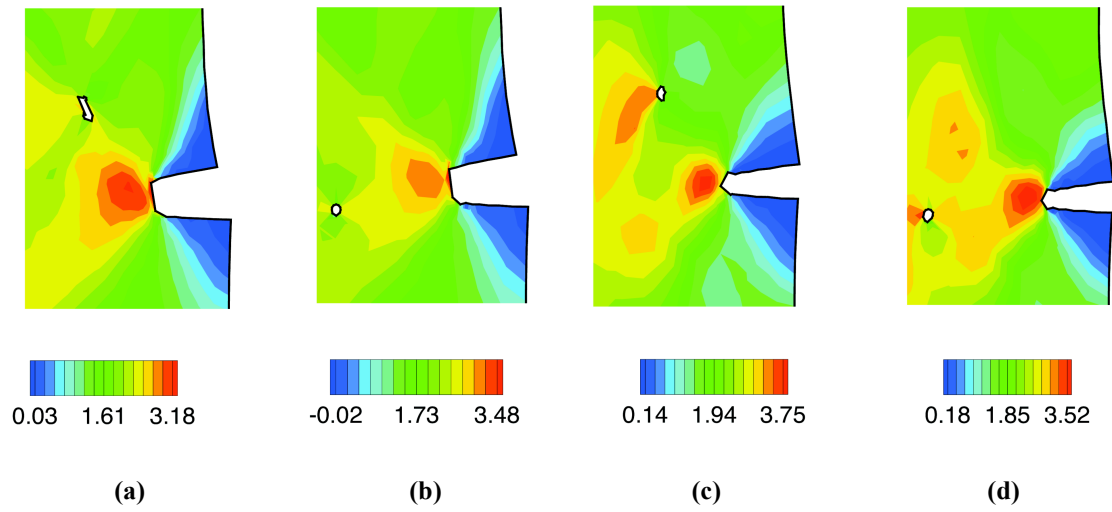


Figure 8.11 Normal stresses around the crack tip indicating crack tip-micro void interactions for low angle GBs (a, b) and high angle GBs (c, d)

CHAPTER 9

SHEAR-STRAIN LOCALIZATION AND INCLUSION EFFECTS UNDER HIGH COMPRESSIVE DYNAMIC LOADS

A three-dimensional multiple-slip dislocation-density-based crystalline formulation, specialized finite-element formulations, and L_∞ Voronoi tessellations adapted to martensitic orientations, were used to investigate shear-strain localization, and dislocation-density evolution in martensitic microstructures under dynamic compressive loads. In this chapter, the computational framework and the constitutive formulation used to investigate the effects of strain rate and inclusions on the evolution of shear-strain localization were investigated. Three loading pressure values have been investigated 0.5 GPa, 1.0 GPa and 1.5 GPa. To investigate the effect of inclusions, we modeled a heterogeneous crystalline structure with b.c.c. crystalline structures for the martensitic phase and NaCl like crystal structure for the MnS inclusions placed at the triple junctions.

9.1 Dynamic Shear-Strain Localization Under Compressive Pressure Loads

The multiple-slip dislocation-density based crystal plasticity formulation, the specialized finite element algorithm, and the L_∞ Voronoi scheme were used to investigate the large strain inelastic behavior of martensitic steel under dynamic loadings. The martensite orientation is represented as outlined in Chapter 3. The parent austenite grain is assumed to be oriented based on the loading plane of $(001)_\gamma$, and the loading direction of $[010]_\gamma$. The K-S relation is adapted as the martensite OR, and $\{111\}_\gamma$ is assumed as the habit plane. The martensite morphology is generated by the L_∞ Voronoi tessellation to generate block and packet microstructures relative to the parent austenite grain. A representative aggregate size was determined by modeling the response of aggregates with different aggregate sizes. In this study, 40 martensitic grains are used with 14 packets, with an average of 3 blocks per packet as shown in Figure 9.1. It is also assumed that the parent austenite grain has an initial cube orientation.

The material properties (Table 9.1) that are used here are representative of low nickel alloy steel, and were validated along with the computational framework and the constitutive formulation with experimental results, as detailed in Chapter 6, on 10% Ni steel alloy under

quasi-static compression loading. The global nominal stress-strain curve of a comparison between results from different strain rate is shown in Figure 9.2. Comparisons were made for quasi-static result and dynamic results on strain rates of 1 200/s, and 12 000/s by applying uniaxial velocity in the topside of the model. As seen, nominal stresses increase with increasing strain rates. At higher strain rates (12 000/sec) undulation can be observed, which come as a result of shear-strain accumulations.

In the current study, based on a convergence analysis, 3541 four noded quadrilateral elements were used with a plane strain analysis for a specimen size of 3.2 mm by 6.2 mm (Figure 9.1). A dynamic pressure loading is applied as illustrated in Figure 9.1; three loading pressure values have been investigated 0.5 GPa (Model 1), 1.0 GPa (Model 2) and 1.5 GPa (Model 3). The load is applied until 12.5 μ s for the three models.

The nominal strain and the strain-rate corresponding to the applied loads were calculated from the average nodal displacement and velocity on the top boundary as shown in Figure 9.3. The nominal strain at 12.5 μ s for model 1 is 0.91%, 7.8% for model 2, and 25.6% for model 3. The maximum nominal strain rate for Model 1 is 7,135/sec, 14,571/sec for Model 2, and 27,728/sec for Model 3.

Results for the normalized normal stresses (stress values are normalized by the static yield stress) in Model 1, at 2.5 μs , 5.0 μs , 7.5 μs , and 12.5 μs are given in Figure 9.4. The incident wave can be observed in Figure 9.4a with a maximum value of -1.4. The reflected wave from the bottom fixed boundary with higher nominal stresses can be observed in Figure 9.4b, with a maximum value of -2.15. The unloading reflected wave from the top free boundary can be seen in Figures 9.4c-9.4d, with a normalized stress value of approximately 1.5 for the reflected wave. The effects of the release wave from the free boundary and the symmetry BCs are obvious in the non-uniform distribution of the nominal stresses. For Model 1, there was no significant plastic deformation, and as the normalized stress values indicate, the stresses are only marginally higher than the static yield stress.

For Model 2 (1.0 GPa), the reflected stress wave from the bottom boundary results in plastic deformation. As shown in Figure 9.5a, the accumulated maximum plastic shear is 1.02 at 12.5 μs . The maximum lattice rotation at 12.5 μs is -17.35° (Figure 9.5b), reaching its maximum at the martensitic blocks in the bottom of the model. The maximum normalized nominal stress at 12.5 μs is -3.66 (Figure 9.5c) that occurs at the blocks' boundaries and around triple junctions. The maximum temperature at 12.5 μs is 450 $^\circ\text{K}$ (Figure 9.5d).

It should also be noted that high transverse stresses occur and result in tensile hydrostatic pressure in the model, as a result of shear slip and wave unloading at the top boundary. Figure 9.6 shows the normalized hydrostatic pressure, at times of 5.0 μs , 7.5 μs , 10 μs , and 12.5 μs . The negative hydrostatic pressure is shown in Figures 9.6b-9.6d). The maximum tensile normalized hydrostatic pressure stress is -1.4 at 10 μs (Figure 9.6c). These maximum values occur at the triple junctions that might lead to void nucleation and growth.

Results for shear slip in Model 3 (2.0 GPa) at times of 2.5 μs , 5.0 μs , 7.5 μs , and 12.5 μs are shown in Figure 9.7. As shown in Figures 9.7c-9.7d, the accumulated maximum plastic shear slip is 1.35 at 7.5 μs , and is 2.25 at 12.5 μs . This large value of plastic shear is due to geometrical and thermal softening; the geometrical softening occurs due to the large lattice rotation that is high as 29.3° (Figure 9.8a) at 7.5 μs and 38.0 at 12.5 μs (Figure 9.8b), reaching its maximum inside the blocks. Thermal softening results from high temperature as a result of high plastic deformation and it is as high as 459 °K (Figure 9.8c) at 7.5 μs and 596 °K at 12.5 μs (Figure 9.8d).

To further elucidate the local microstructural mechanisms, the contours for the mobile dislocation-densities (Figures 9.9a-9.9b), and the immobile dislocation-densities (Figures

9.9c-9.9d) corresponding to the two most active slip-systems, at 7.5 μs are shown. The maximum mobile dislocation-densities are $2.17 \times 10^{14} \text{ m}^{-2}$ for $(112) / [11\bar{1}]$, and $2.0 \times 10^{14} \text{ m}^{-2}$ for $(\bar{1}12) / [1\bar{1}1]$. The maximum immobile dislocation-densities for the three slip-systems are $2.11 \times 10^{15} \text{ m}^{-2}$ for $(112) / [11\bar{1}]$, and $1.9 \times 10^{15} \text{ m}^{-2}$ for $(\bar{1}12) / [1\bar{1}1]$. The evolution of dislocation-densities along selected blocks and along low-angle grain boundaries (as noted earlier grain boundaries are equivalent to block boundaries) result in an increase in dislocation-densities values and a localization of shear slip as shown in Figure 9.7. These increases in dislocation-density are due to an alignment of the load towards $[010]_{\gamma}$. $[011]_{\gamma}$ is a maximum resolved shear stress direction for this load, since it is 45° from the loading direction. $[011]_{\gamma}$ is also parallel to the long direction of laths and blocks, and parallel to the slip direction $[111]_{\alpha'}$ based on the K-S OR.

To further underscore the orientation relation between loading direction, slip-systems, and the lath long directions, the stereographic projection of the slip-systems of variant #11 relative to the loading direction, the locus of maximum resolved shear stress (a circle that is 45° from the loading direction), and the long direction of the variant are plotted as in Figure 9.10. As can be seen, the slip direction $[11\bar{1}]_{\alpha'}$ aligns with $[0\bar{1}\bar{1}]_{\gamma}$, which is the long direction

of the laths inside the block and the maximum resolved shear direction for the uniaxial loading direction of $[010]_y$. Furthermore, slip-plane $(112)_\alpha$ is almost coincident with the maximum resolved shear locus. This would activate slip-system $(112)/[11\bar{1}]$ in this variant as was confirmed by the results shown in Figures 9.9a, and 9.9c).

Similarly for variant #8, the slip direction $[\bar{1}\bar{1}\bar{1}]_\alpha$ has the low angle GB relation (10.5°) with the direction $[0\bar{1}\bar{1}]_y$. Slip-plane $(\bar{1}\bar{1}2)$ is nearly adjacent to the maximum resolved shear stress direction. This activates slip-system $(\bar{1}\bar{1}2)/[1\bar{1}\bar{1}]$ as confirmed by the results shown in Figures 9.8b, and 9.8d. This special configuration aligns the slip-systems with the maximum resolved shear stress direction with the long direction of the blocks, and when combined with the low angle boundaries between blocks, acts as shear pipes for the localization of dislocation-densities and shear strains; more details for shear pipes effect is presented in Chapter 6.

9.2 Secondary-Phase Inclusions Effects

As noted earlier, inclusions play a major role in the fracture and failure behavior of high-strength steels, see, for example, [1-4]. To investigate these effects,

we modeled a heterogeneous crystalline structure with NaCl like crystal structure for the MnS inclusions and b.c.c. crystalline structures for the martensitic phase. We assumed that 0.056% of the volume was MnS inclusions with nine inclusions placed at triple junctions, as shown in Figure 9.11. The inclusion radius was chosen as 20 μm , which is comparable with observed inclusion size in steels [4]. For this analysis, we used the previous variant arrangement, boundary conditions, and loading pressure values.

Figure 9.12 shows the normalized normal stresses, for the 0.5 GPa loading pressure model (Model 1), at 2.5 μs , and 12.5 μs . The maximum normalized normal stress is -1.26 at 0.25 μs and -1.36 at 12.5 μs . In both cases, there is a considerable decrease in the values of normal stresses in comparison with cases with no inclusions. This difference in behavior can be due to the dispersion and attenuation of waves at the inclusions. Similar effects for Model 2, with a pressure loading of 1.0 GPa, can be drawn for the incident wave as the normal stresses decrease due to the inclusions. Once plastic deformation occurs, there are increases in the normal stresses near the inclusions. The accumulation of plastic strain around the inclusions further accelerates

shear strain localization.

Results for shear slip for Model 3 (1.5 GPa), at 2.5 μs , and 7.5 μs are presented in Figure 9.13. As shown in Figure 9.13, the accumulated maximum plastic shear slip is 1.1 at 2.5 μs , 2.3 at 7.5 μs . The large increase in shear slip is a result of extensive plastic deformation in the inclusions and its vicinity, which result in higher dislocation-density activities and shear slip.

The contours for the mobile dislocation-densities (Figures 9.14a-9.14b), and the immobile dislocation-densities (Figures 9.14c-9.14d) corresponding to the two most active slip-systems, at 7.5 μs are shown. The maximum mobile dislocation-densities are $2.23 \times 10^{14} \text{ m}^{-2}$ for $(112) / [11\bar{1}]$, and $2.15 \times 10^{14} \text{ m}^{-2}$ for $(\bar{1}12) / [1\bar{1}1]$. The maximum immobile dislocation-densities for the two slip-systems are $2.25 \times 10^{15} \text{ m}^{-2}$ for $(112) / [11\bar{1}]$, and $2.12 \times 10^{15} \text{ m}^{-2}$ for $(\bar{1}12) / [1\bar{1}1]$. There are higher shear slip and dislocation-densities at the region around the inclusions, as shown in Figure 9.13. The significant increase in shear slip in the case with inclusions is due to slip-system incompatibilities between MnS inclusions and the martensitic matrix. Furthermore, high plastic deformation in the inclusions results in high plastic deformation in the

matrix, which results in increase shear strain localization

The lattice rotation, temperature, and normalized hydrostatic pressure stress are presented in Figure 9.15. The increase in shear-strain localization is due to geometrical and thermal softening; the geometrical softening occurs due to the large lattice rotation that is high as -42.2° (Figure 9.15a) at $7.5 \mu\text{s}$, reaching its maximum at blocks boundaries. The maximum temperature is $847 \text{ }^\circ\text{K}$ (Figure 9.15b) at $7.5 \mu\text{s}$. Furthermore, there are high normalized values of hydrostatic pressure stress that are as high as 4.89 in compression and 0.89 in tension at $7.5 \mu\text{s}$, (Figure 9.15c).

9.3 Summary

This investigation provides detailed validated predictive capabilities that have been used to understand complex interrelated physical mechanisms that relate to martensitic microstructures at different physical scales under dynamic loading. A multiple-slip rate-dependent crystalline constitutive formulation that is coupled to the evolution of mobile and immobile dislocation-densities, and specialized computational schemes have been developed

to investigate the effects of strain-rate, secondary-phases, and elastic and plastic wave propagation in high-strength martensitic steels.

It has been shown that for a loading direction of $[010]_y$, the maximum resolved shear stress direction, the slip directions and the long direction of blocks are almost coincident. When combined with low angle GBs between blocks and slip-system compatibility, these results in shear pipes, which promote extensive shear-strain localization.

It is shown that tensile hydrostatic pressure due to the unloading of the plastic waves at the free boundary and the accumulation of plastic shear-strain in the martensitic blocks can occur around certain triple junctions. The effects of inclusions on dislocation activities and behavior of martensitic steels was also investigated by incorporating NaCl like structures within b.c.c structures (martensitic blocks). The results clearly show the effect of inclusions and crystalline heterogeneities in wave scattering, and promoting shear-strain localization with increasing pressure loads.

This general methodology underscores the importance of accurately representing martensitic microstructure on different microstructural scales. This predictive framework can be used to model other steel phases and alloys, such as bainite and dual phase steels and to

potentially control behavior at the microstructural scale for a spectrum of high dynamic pressure loads.

REFERENCES

- [1] Garrison W. M., and Moody N. R., 1987, "Ductile Fracture," *J. Phys. Chem. Solids*, 48(11), pp. 1035-1074.
- [2] Lorio L. E., and Garrison W. M., 2002, "Effects of Gettering Sulfur as CrS or MnS on Void Generation Behavior in Ultra-High Strength Steel," *Scripta Mater.*, 46(12), pp. 863-868.
- [3] Garrison W. M. and Wojcieszynski A. L., 2007, "A Discussion of the Effect of Inclusion Volume Fraction on the Toughness of Steel," *Mater. Sci. Eng A-Struct.*, 464, pp. 321-329.
- [4] Minnaar K., and Zhou M., 1998, "An Analysis of the Dynamic Shear Failure Resistance of Structural Metal," *J. Mech. Phys. Solids*, 46-10, pp. 2155-2170.

**Table and Figures for
Chapter 9**

Table 9.1 Properties of martensitic and MnS inclusions.

Properties	Martensite phase	MnS inclusions
Young's modulus, E	22.8GPa	45.6GPa
Static yield stress, τ_y	517MPa	300MPa
Poisson's ratio, ν	0.3	0.3
Rate sensitivity parameters, m	0.01	0.01
Reference strain rate, $\dot{\gamma}_{ref}$	$0.001s^{-1}$	$0.001s^{-1}$
Critical strain rate, $\dot{\gamma}_{critical}$	10^4s^{-1}	10^4s^{-1}
Burger vector, b	$3.0 \times 10^{-10}m$	$3.0 \times 10^{-10}m$
Reference stress interaction coefficient, a_i ($i=1, n$)	0.5	0.5
Initial immobile dislocation-density, $\rho_{im}^{(\alpha)}$	Chapter 5	$10^{10}m^{-2}$
Initial mobile dislocation-density, $\rho_m^{(\alpha)}$	Chapter 5	10^7m^{-2}

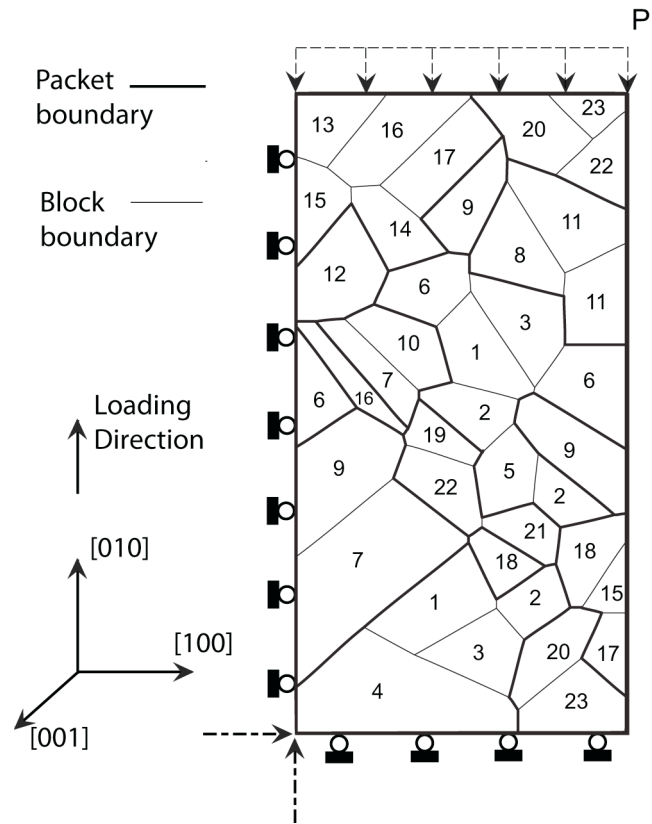


Figure 9.1 Microstructural model used in the current study, the distribution of variants in blocks and packets (variants numbered as indicated in Table 3.4), loading, geometry, and boundary conditions.

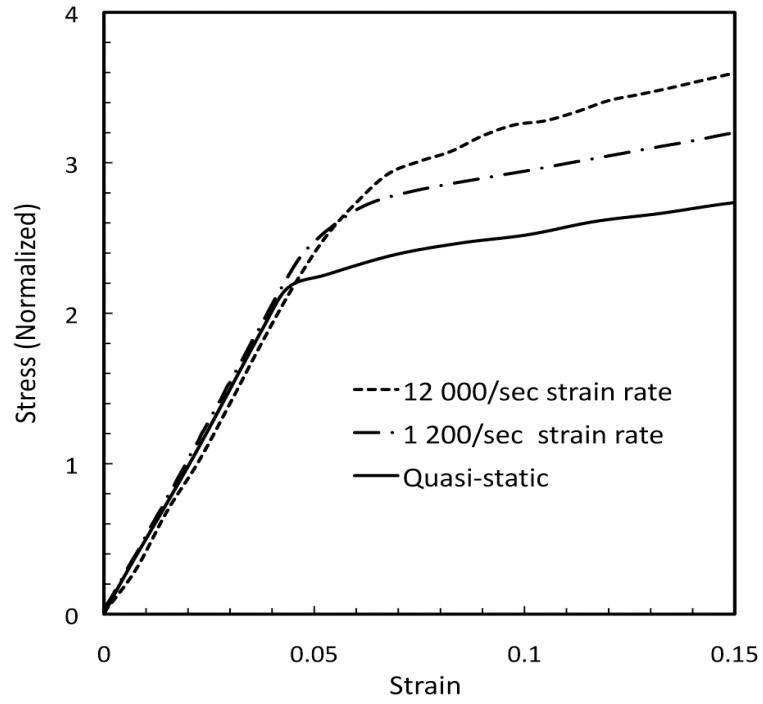


Figure 9.2 The global stress-strain curve for low nickel martensitic steel for different strain-rates (stresses are normalized by the static yield stress).

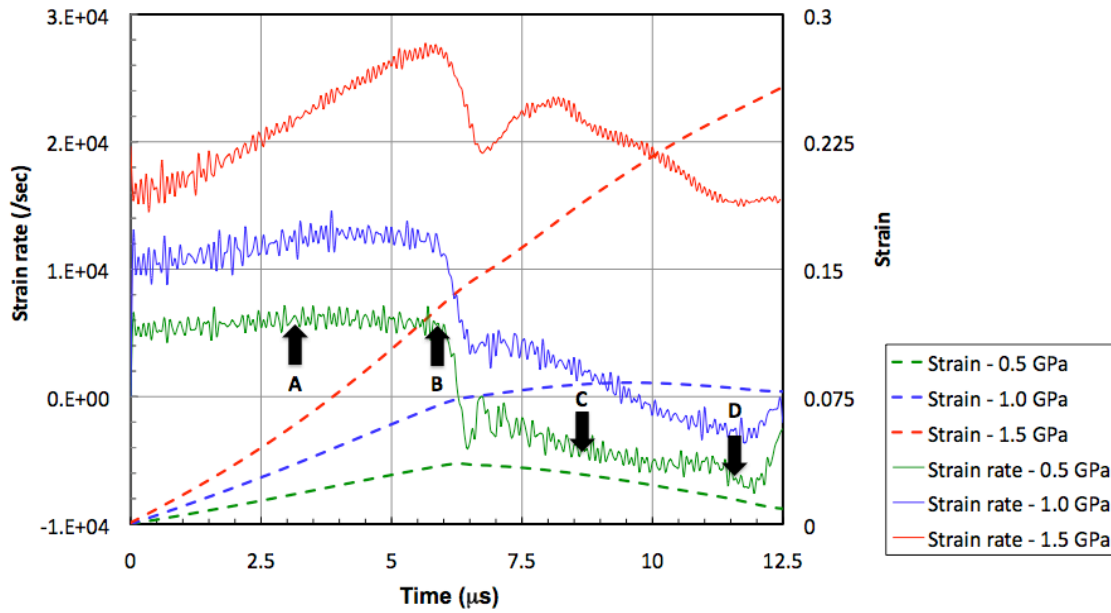


Figure 9.3 Nominal strain-rate and strain for different loading pressures. The arrows indicate wave reflection from one of the horizontal boundaries; (A) incident wave reflects from the bottom boundary; (B) wave reflects from the top boundary; (C) wave reflects from the bottom boundary again; (D) wave reflects from the top boundary.

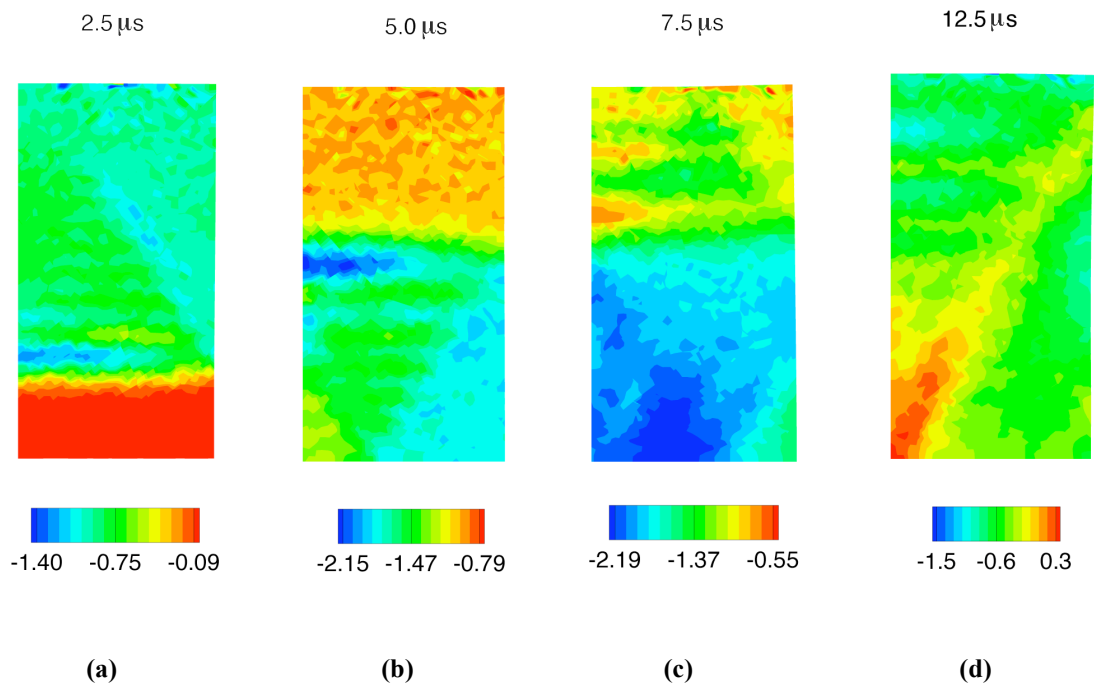


Figure 9.4 Normalized normal stresses for a dynamic pressure loading of 0.5 GPa at different times.

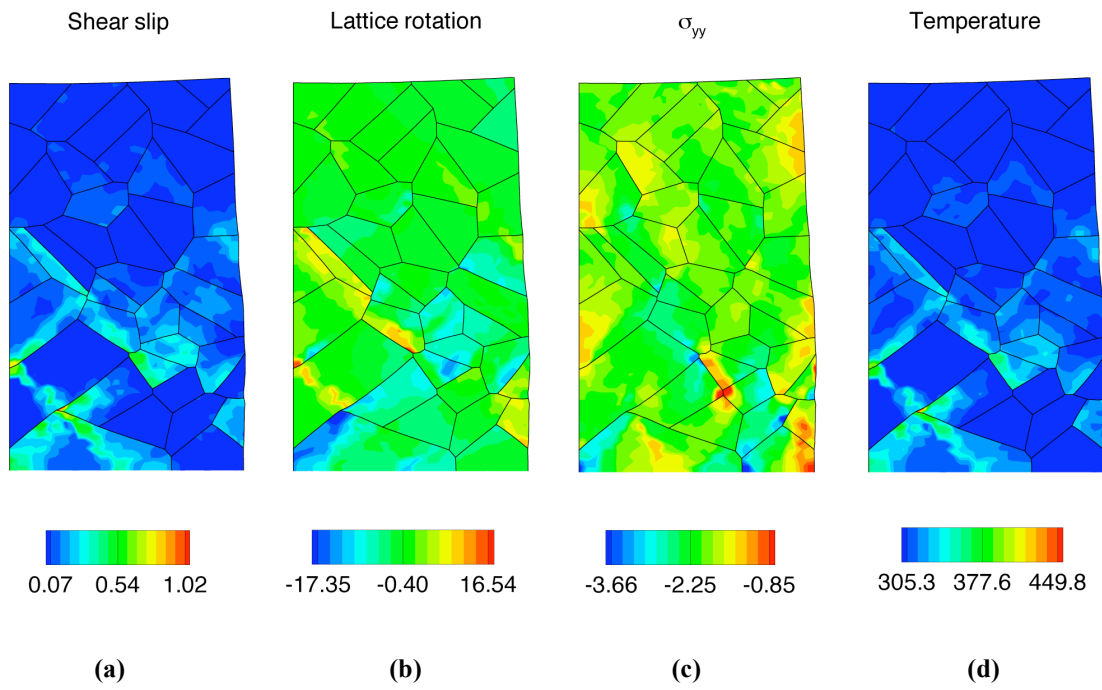


Figure 9.5 Dynamic loading (1.0 GPa), at 12.5 μs (a) Shear slip contours, (b) lattice rotation in degrees, (c) normalized normal stress, (d) temperature in degrees Kelvin.

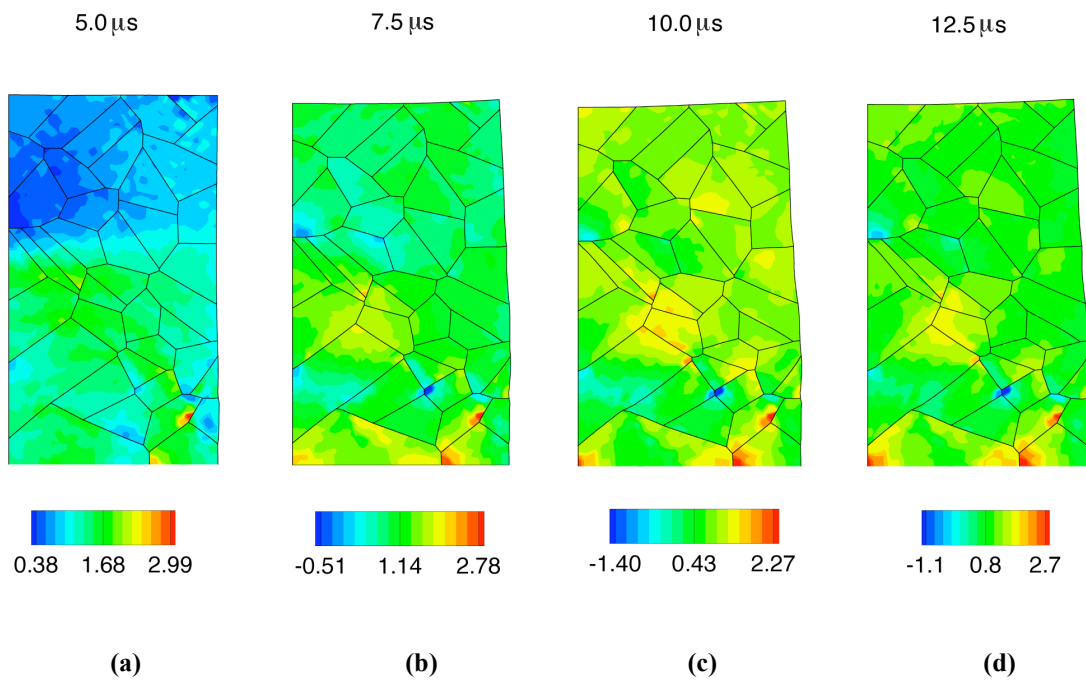


Figure 9.6 Normalized hydrostatic pressure stresses for a dynamic loading of 1.0 GPa at different times.

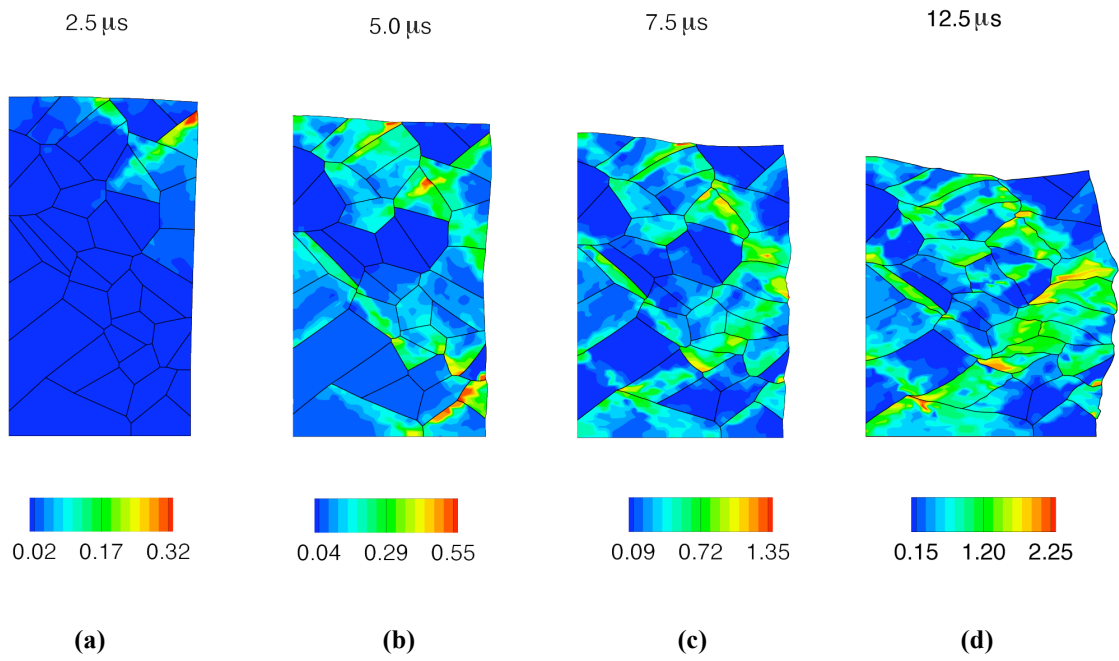


Figure 9.7 Shear slip for a dynamic loading 1.5 GPa at different times.

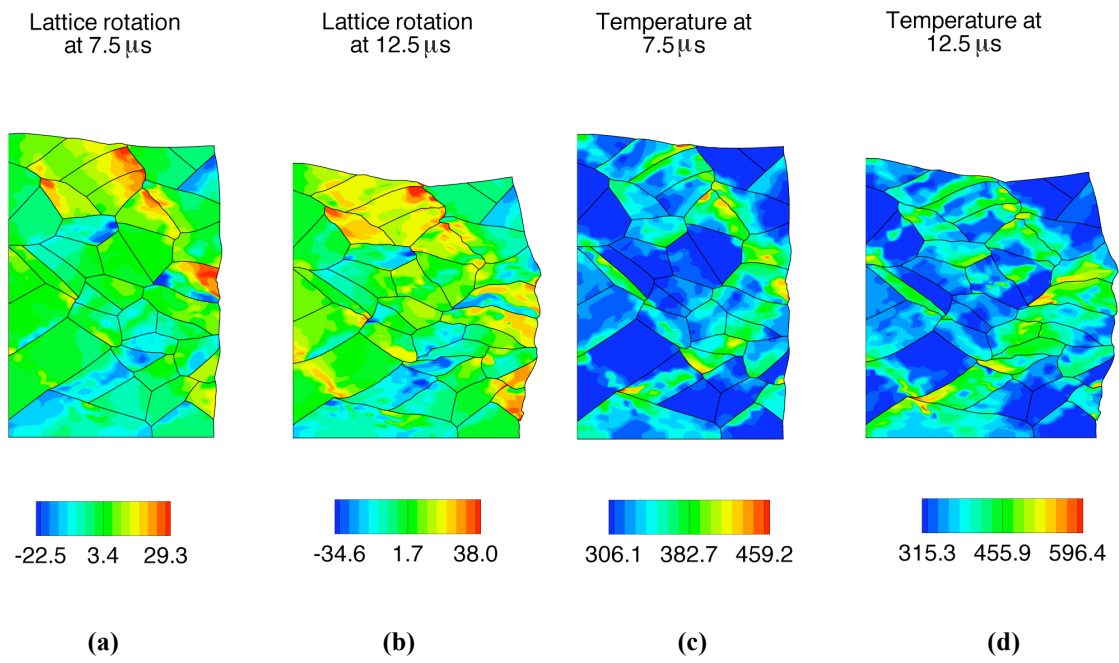


Figure 9.8 Lattice rotation and temperature for a dynamic loading of 1.5 GPa at 7.5 and 12.5 μs (a-b) lattice rotation in degrees, (c-d) temperature in degrees Kelvin.

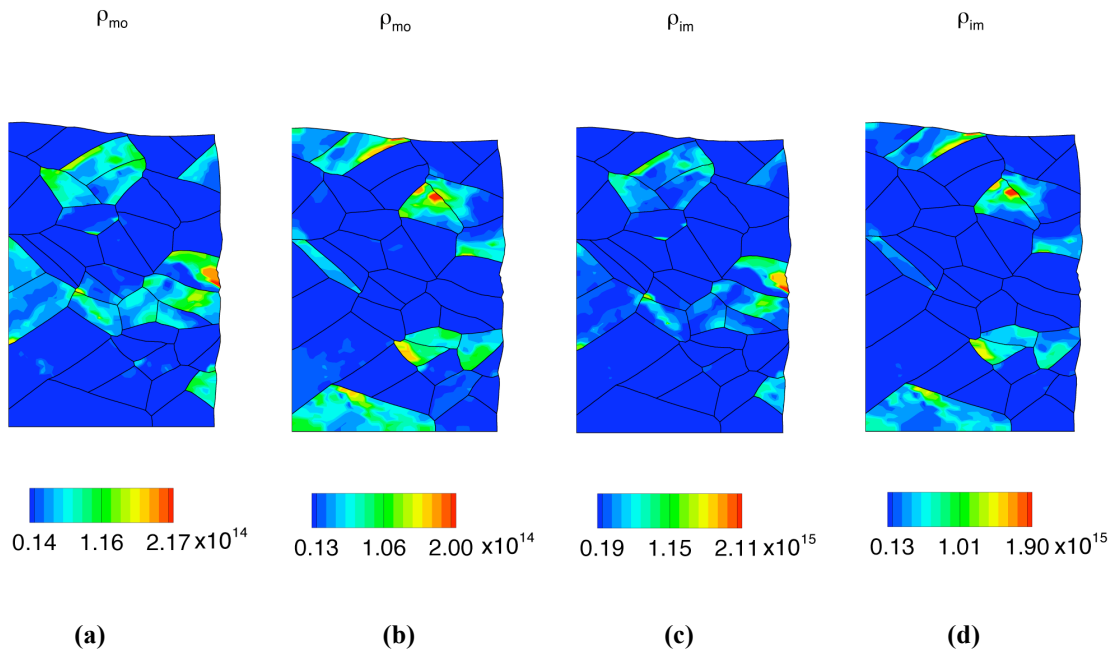


Figure 9.9 Mobile and immobile dislocation-densities at 7.5 μ s for most active slip-systems for (a) slip-system (112)/[11 $\bar{1}$], (b) slip-system ($\bar{1}12$)/[1 $\bar{1}\bar{1}$], (c, d) immobile dislocation-densities, (c) slip-system (112)/[11 $\bar{1}$], (d) slip-system ($\bar{1}12$)/[1 $\bar{1}\bar{1}$] at a pressure loading of 1.5 GPa.

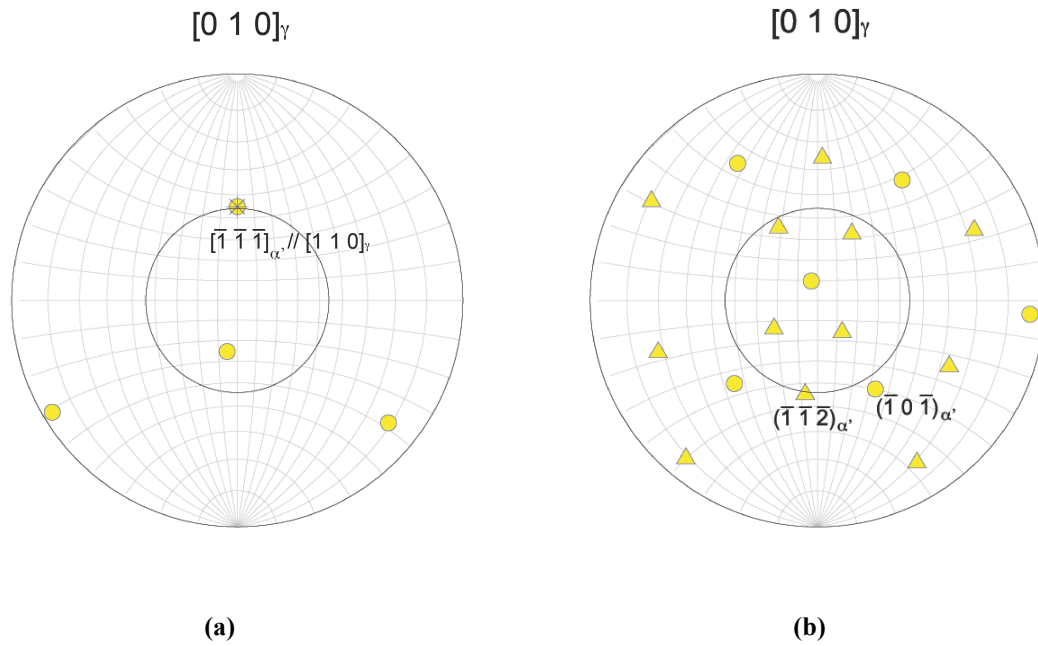


Figure 9.10 $[010]_\gamma$ stereographic projection for variant #11 slip-systems relative to the loading direction, the locus of maximum resolved shear stress (the inner circle) and the long direction of the variants (presented as * in figure a) (a) the slip directions, (b) the slip planes.

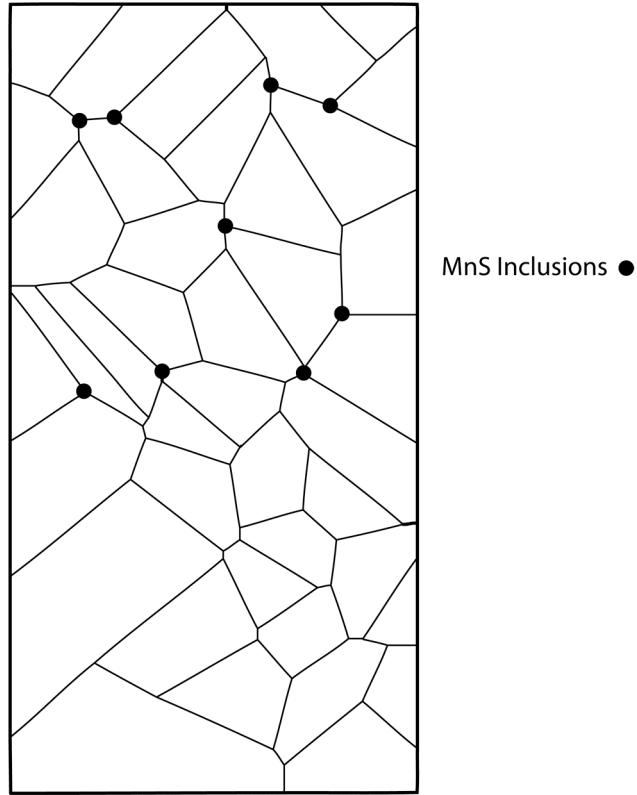


Figure 9.11 Microstructural model and inclusion distribution

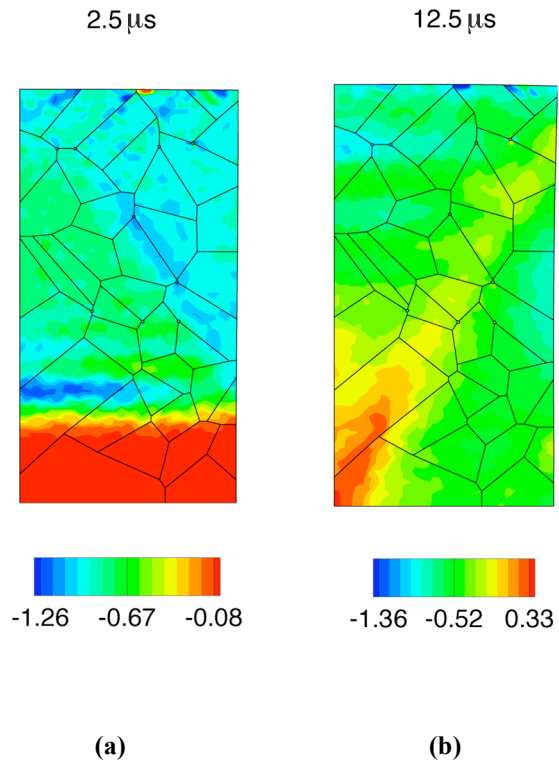


Figure 9.12 Normalized normal stresses for a dynamic loading of 0.5 GPa - inclusion interactions at different times.

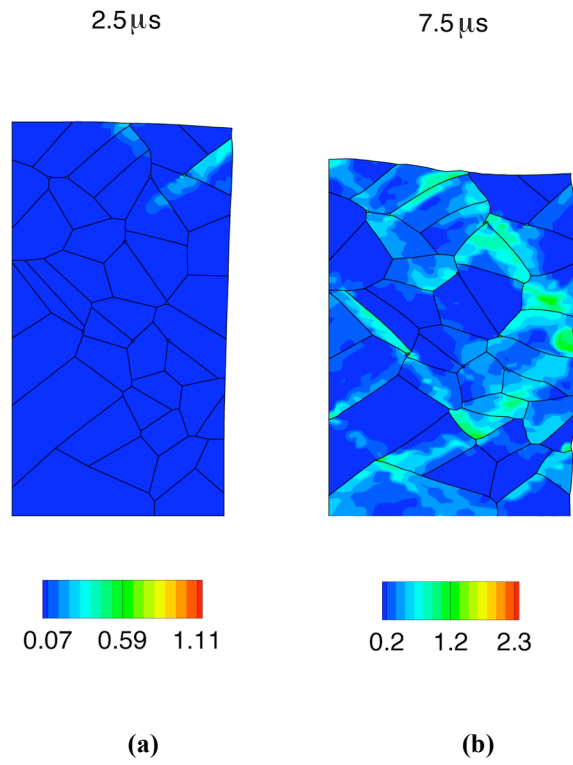


Figure 9.13 Shear strain for dynamic loading at a dynamic loading of 1.5 GPa – inclusions interactions at different times.

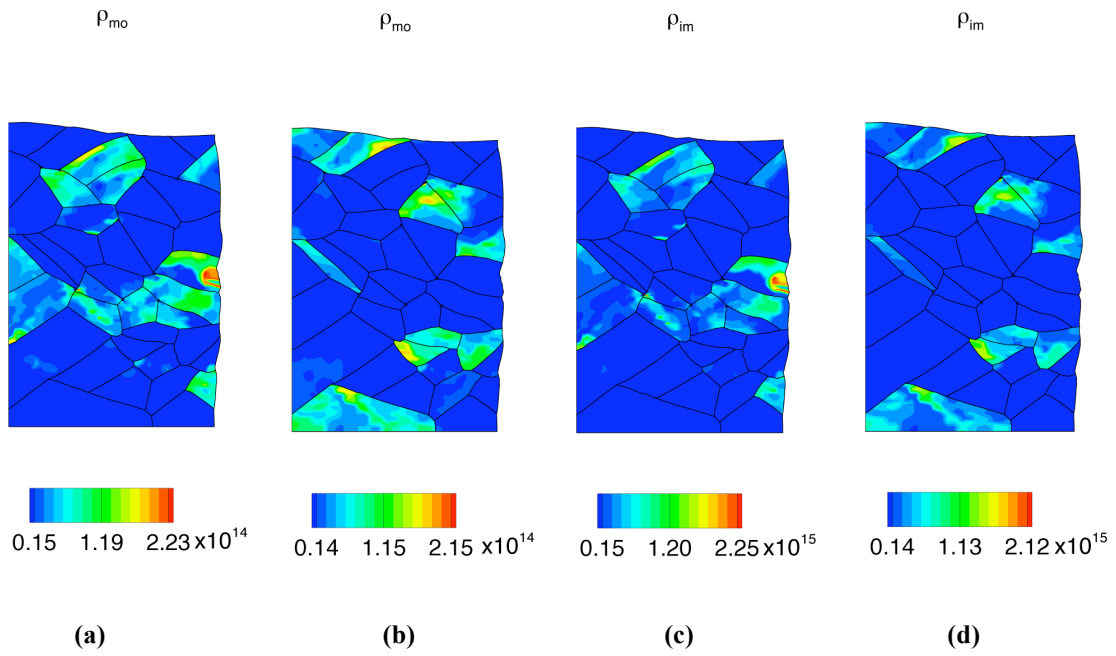


Figure 9.14 Mobile and immobile dislocation-densities at 7.5 μ s for the most active slip-systems for (a) slip-system (112)/ [11 $\bar{1}$], (b) slip-system ($\bar{1}$ 12)/ [1 $\bar{1}$ 1], (c, d) immobile dislocation-densities, (c) slip-system (112)/ [11 $\bar{1}$], (d) slip-system ($\bar{1}$ 12)/ [1 $\bar{1}$ 1] at pressure loading of 1.5 GPa.

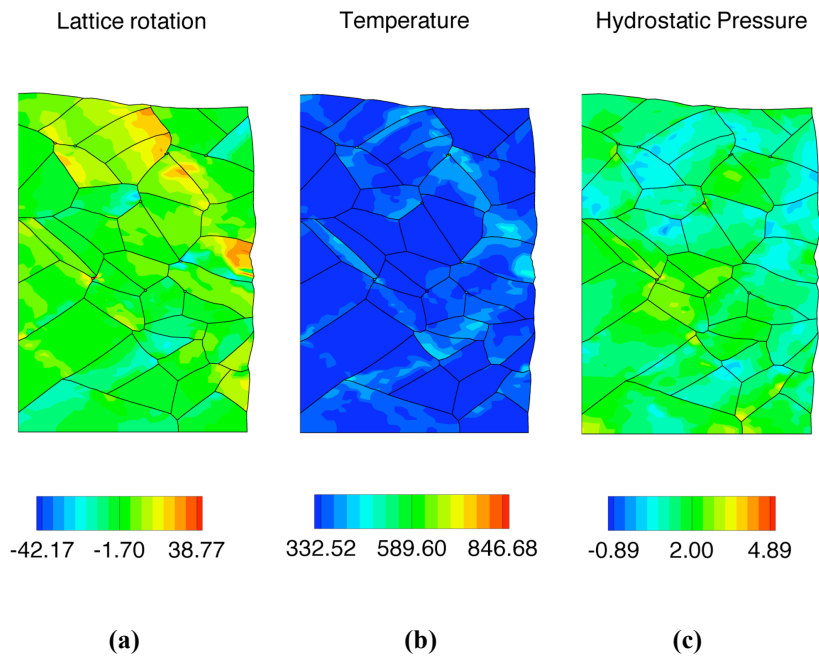


Figure 9.15 Dynamic loading at a pressure of 1.5 GPa – inclusion interactions at 7.5 μ s (a) lattice rotation in degrees, (b) temperature in degrees Kelvin, (c) hydrostatic pressure.